Regional Assessment of Glacier Motion in Kluane National Park, Yukon Territory

Alexandra Waechter

Thesis submitted to the
Faculty of Graduate and Postdoctoral Studies
in partial fulfillment of the requirements
for the M.Sc. Degree in Physical Geography

Department of Geography
Faculty of Arts
University of Ottawa

Supervisor:

Dr. Luke Copland

Thesis Committee:

Dr. Laurence Gray

Dr. Denis Lacelle

ABSTRACT

This project presents regional velocity measurements for the eastern portion of the St. Elias Mountains, including the entire glaciated area of Kluane National Park, derived from speckle tracking of Radarsat-2 imagery acquired in winter 2011 and 2012. This technique uses a cross-correlation approach to determine the displacement of the ‘speckle’ pattern of radar phase returns between two repeat-pass images. Further reconstruction of past velocities is performed on a selection of key glaciers using feature tracking of Landsat-5 imagery, allowing for the investigation of variability in glacier motion on interannual and decadal time scales.

The results of the analysis showed that there is a strong velocity gradient across the region reflecting high accumulation rates on the Pacific-facing slope of the mountain range. These glaciers may have velocities an order of magnitude greater than glaciers of a similar size on the landward slope. Interannual variability was high, both in relation to surge events, of which a number were identified, and variation of other unknown controls on glacier motion. A long-term trend of velocity decrease was observed on the Kaskawulsh Glacier when comparing the results of this analysis to work carried out in the 1960s, the pattern of which is broadly congruent to measurements of surface elevation change over a similar period.

ACKNOWLEDGMENTS

Funding and resources for this project have been provided by:

National Sciences and Engineering Research Council of Canada Graduate Scholarship
Ontario Graduate Scholarship
Northern Scientific Training Program
Polar Continental Shelf Project
Canada Foundation for Innovation
Ontario Research Fund
CRYO-EX and GLACIO-EX
University of Ottawa
Parks Canada (especially Jean Poitevin for providing the Radarsat-2 imagery that formed the basis of this project, and the wardens of Kluane National Park and Reserve)
Kluane Lake Research Station

I would also like to thank Dr. Laurence Gray for his ongoing willingness to share his program and expertise and for his patience in answering questions and addressing problems when they arose. Likewise, I owe a debt of gratitude to Wesley Van Wychen without whose attention this project would have been much more slowly accomplished, and to all the lab members of the Laboratory for Cryospheric Research for their support throughout the project.

I gratefully acknowledge the help of Dr. Andreas Kääb in providing access to his feature tracking software, and of Emilie Herdes and Camilo Rada who processed and provided dGPS data for comparison. Large thanks are due to Sian Williams and the other staff at KLRS for welcoming us back every year, and for maintaining such an important link to research in the Yukon over the past 52 years.

I would like to thank my supervisor, Dr. Luke Copland, for his support, patience and guidance throughout the process, and for affording me so many opportunities that I would not have been able to imagine two years ago.

I gratefully thank my family and friends, especially my parents Diane and Tom Waechter for their constant support throughout this project, and friends Stephanie Smith and Greg Lopinski for encouraging me to pursue graduate studies. Their interest in this project has been both inspiration and motivation. Finally, thanks are due to Jonathan Wheatland for his unflagging encouragement and good sense, advice on figures, and for taking care of the rest of my life when my mind was focused on completing the preparation of this paper.

TABLE OF CONTENTS

LIST OF TABLES

LIST OF FIGURES

Chapter 1: Introduction

1.1 Global context

Warming of the continents, particularly the disproportionate warming observed at higher latitudes, has increased the vulnerability of permafrost, snow, sea ice, glaciers and ice caps to melting (IPCC, 2007; SWIPA, 2011). Of importance, then, is a comprehensive baseline assessment of the status of features such as glaciers, given their potential for large impacts on global sea level, water resources and high-mountain hazards. Developments in air- and space-borne data-collection techniques have opened up new opportunities for expanding and addressing gaps in current datasets, including more extensive and improved estimates of long-term changes to glacier mass balance, such as measurements of area changes (e.g. Barrand and Sharp, 2010), surface elevation changes (e.g. Berthier et al., 2010; Larsen et al., 2007; Arendt et al, 2002), and mass changes (e.g., via the Gravity Recovery and Climate Experiment (GRACE) program; Jacob et al., 2012; Luthcke et al., 2008). Area and surface elevation changes constitute the majority of the existing satellite monitoring, however these measurements do not properly account for changes in ice dynamics. Kääb (2005b) suggested that given advances in feature tracking and synthetic aperture radar (SAR) interferometry and offset-tracking techniques, glacier velocity could be a feasible and valuable addition to global glacier monitoring datasets such as those published by the World Glacier Monitoring Service (http://www.geo.uzh.ch/microsite/wgms/) or the Global Land Ice Measurements from Space project (http://www.glims.org/). Acceleration of outlet glaciers in response to increased melt has been identified as a significant mass loss mechanism, particularly for the Greenland and Antarctic Ice Sheets (Pritchard et al., 2009). Elsewhere, glacier velocities represent an important component of understanding ice discharge, useful for determining factors such as calving rates of tidewater glaciers or estimating glacier mass balance.

1.2 Project objective

The objective of this project has been to produce a regional assessment of glacier motion for the southwest Yukon Territory, with a particular focus on Kluane National Park. Surface velocity fields have been derived across the entire glaciated region from winter 2011 and 2012, producing velocity maps suitable as a baseline for future studies, for quantifying current ice fluxes, and for monitoring and understanding glacier surges. Further analysis has been undertaken to evaluate the state of activity of known surge-type glaciers over the study period, and to assess whether there have been changes in surface velocity over ~30 years for several key glaciers in this region.

1.3 Study area

The region of interest is the glaciated area of Kluane National Park in the southwest Yukon Territory, extending slightly southward into Alaska and British Columbia to capture the termini of the Tweedsmuir and Hubbard Glaciers (Figure 1.1). This region forms part of the St. Elias-Wrangell Icefields, one of the largest continuous extra-polar ice masses in the world with a mid- to late-20th century area of 45 905 km^2 (Berthier et al., 2010). The mountain range runs parallel to the coast, straddling the borders between Alaska, the Yukon, and British Columbia, and contains Canada's highest peak, Mt. Logan, at an elevation of 5959 m above sea level (a.s.l.). From the icefield summit glaciers flow west into Alaska, south towards the Gulf of Alaska or east and north into the northwest/southeast-oriented Shakwak Trench bounding this glaciated region from the rest of the Yukon Territory. Important outlet glaciers from the icefield are the Kaskawulsh Glacier (~ 72 km long), flowing east to terminate near the south end of Kluane Lake, Seward Glacier (~ 121 km to the foot of the Malaspina Glacier piedmont that it feeds), flowing west out of the study area, and the Hubbard Glacier (~ 122 km long), flowing south to terminate in Yakutat Bay.

1.3.1 Regional climate

Patterns of precipitation and temperature variation throughout the region are influenced by atmospheric circulation and elevation, which create a strong gradient in conditions from the maritime Pacific coast to the semiarid continental interior, over a fairly short horizontal distance, only ~185 km from Yakutat to Haines Junction. Winter atmospheric circulation is dominated by the Aleutian Low in the North Pacific that draws warm moist air from the tropics towards the southeast Alaskan coast. The result is high precipitation in the fall months when the low pressure system begins to form, and persistent cloud cover over the coastal region (Fleming et al., 2000). At Yakutat, the annual precipitation is over 3000 mm a^{-1}. Over the continent, high pressure systems tend to dominate, and this, combined with the mountain barrier, means that the continental leeward side receives much less moisture (~300 mm a^{-1}). With less cloud, radiative losses throughout the winter are high, leading to much lower temperatures. The strongest precipitation gradient across the mountain profile occurs during fall, though it decreases almost to zero in July when coastal precipitation is at its minimum and interior precipitation attains its seasonal maximum (Fleming et al., 2000).

Precipitation and temperature have been measured at a number of low elevation permanent meteorological stations for several decades (for example, Yakutat (AK), Haines Junction (YT) and Burwash Landing (YT) since 1948, 1944 and 1966, respectively). However, conditions at these sites may bear little resemblence to those at higher elevations. The precipitation record has been augmented spatially by a series of snowpits dug across a 'transmountain profile' during the 1960s that revealed a decrease in accumulation towards the interior, from ~ 1500 mm a^{-1} w.e. at the Upper Seward Glacier to < 400 mm a^{-1} w.e. near the equilibrium line of the Kaskawulsh Glacier, with an additional peak at the Divide between the Hubbard and Kaskawulsh Glaciers (Marcus and Ragle, 1970). Ice cores retrieved in the vicinity of Mount Logan have further expanded the accumulation record, and revealed that at high elevation accumulation shows variations that correlate with shifts in large-scale atmospheric circulation related at interannual timescales to the El Niño-Southern Oscillation (ENSO) and Pacific Decadal Oscillation (PDO) as well as shifts at longer timescales (Rupper et al., 2004; Fisher et al., 2004). However, at lower elevations and towards the interior, climate seems to be less impacted by these changes in the Pacific moisture tracks (Fleming and Whitfield, 2010). With limited data at a suitable timescale from the interior of the icefield, it is difficult to identify the patterns and modes of climatic variation across this gradient, or to directly relate it to glacier changes.

1.3.2 Glacier characteristics

The region is notable for the variety of glacier forms and regimes that it contains. Glaciers range in size from <1 km^2 to >3000 km^2, with the largest being the Seward-Malaspina, Bering, and Hubbard glacier systems. The high elevation (typically >2000 m) accumulation plateau at the top of the icefield intercepts Pacific moisture as air masses are advected eastward over the mountains, and Pacific-facing glaciers experience high rates of accumulation that can exceed 1500 mm w.e. a^{-1} (Marcus and Ragle, 1970). Most of these glaciers terminate at or close to sea level where ablation is high. Such glaciers tend to have high rates of ice flux to balance large accumulation and ablation, and a temperate ice regime. In contrast, the glaciers on the continental side of the mountains experience colder, drier conditions, and many of the smaller ones are likely polythermal, such as the Trapridge and Rusty Glaciers (Crossley and Clarke, 1972; Classen and Clarke, 1972; Clarke and Goodman, 1975; Clarke et al., 1984; Field, 1975). Glaciers overlie a complex of accreted terranes resulting in a varied, complex and heavily-faulted geology (Headley et al., 2012), and while direct observations of bed conditions are limited, it is inferred that both soft and hard beds occur in the region. Finally, the region has a large concentration of surging glaciers, including the Lowell and well-studied Trapridge Glaciers in the Yukon (Post, 1969; Clarke, 1991; Clague and Rampton, 1982; Frappé and Clarke, 2007) and Variegated Glacier in Alaska (Kamb et al., 1985; Harrison et al., 1986; Kamb and Echelmeyer, 1987; Raymond and Harrison, 1988; Eisen et al., 2001; Eisen et al., 2005 etc.).

1.3.3 Previous Research

The St. Elias Mountains were first described in detail by the International Boundary Commission in the late 19th and early 20th century, when there was early interest in the glaciology of the Alaskan mountain ranges (Tarr and Martin, 1914). However, this was focused on the more easily-accessible glaciers to the south and west. The continental-facing glaciers of the St. Elias Mountains from the White River valley southwards to the region west of the Alsek River remained only perfunctorily explored. These glaciers were opened up for detailed study following a series of expeditions in the 1930s and 1940s led by Walter A. Wood and Bradford Washburn, largely with the object of mapping and photographing the peaks and ice masses of the area (Marcus and Ragle, 1970). Partly out of this work developed Project Snow Cornice (1948-51) and the Icefield Ranges Research Project (IRRP: 1961-1972), both under the aegis of the Arctic Institute of North America. Both projects were conceived as multi-disciplinary investigations into the glacial environment. Project Snow Cornice was focused on the accumulation basin of the Seward Glacier and produced measurements of weather data, snow accumulation, firn temperature, density and meltwater storage and transport, as well as geology and nunatak biodiversity (Wood, 1948). Its success led to the more ambitious IRRP, conceived around the notion of developing practical field teaching for students, and applying a holistic approach to the study of a glacierized area, with emphasis on the interrelations of different environmental systems (Wood, 1963). It produced research in glaciology, climatology, meteorology, geomorphology, hydrology, and ecology. Results were published in four volumes by the American Geographical Society (Ommanney, 1995). Glaciological studies within the study area were particularly focused on the Kaskawulsh-Hubbard ice divide in the vicinity of Mount Logan, the Kaskawulsh Glacier, and later the Steele valley glaciers. Measurements included ice thickness (Clarke, 1969; Dewart, 1970), surface velocity (Clarke, 1969; Brecher, 1969; Anderton, 1970; Thomson, 1972, Stanley, 1969), snow structure and chemistry (Wagner, 1969; Macpherson and Krouse, 1969; Alford and Keeler, 1970; Alford, 1970), glacier hydrology (Dewart, 1969; Ewing, 1972; Dozier, 1974; Detwyler, 1974), and firn and ice temperatures (Marcus and Ragle, 1970; Crossley and Clarke, 1972; Classen and Clarke, 1972).

The bulk of previous glaciological work in this region has been focused on aspects relating to glacier surges. Early studies largely focused on the identification of surging glaciers and the characteristics of their surge cycles (e.g., duration, periodicity, maximum displacements) (e.g. Post, 1966; Post, 1969; Stanley, 1969; Ommanney, 1980). Later studies incorporated stake array measurements and borehole instrumentation to determine glacier velocity at high resolution and to acquire information on subglacial properties. Much of this research in the Yukon has been centred on the surging glaciers of the Steele Valley in the northwest sector of the study area, most particularly on Trapridge Glacier, with most studies carried out under the impetus of G.K.C. Clarke (e.g. Clarke and Collins, 1984; Clarke et al., 1984; Fischer and Clarke, 2001; Kavanaugh and Clarke, 2006; Frappé and Clarke, 2007). These measurements represent a valuable long-term record of the relationships between subglacial hydrology and surface velocities, but are perhaps limited in their applicability to other large valley glaciers within the study area given that Trapridge Glacier is a relatively small, cold polythermal surge-type glacier (Frappé and Clarke, 2007). Elsewhere, the release of ERTS-1 (later renamed Landsat-1) imagery in the early 1970s, coincident with surges of the Tweedsmuir and Lowell Glaciers, provided an opportunity to explore the use of satellite images for manual tracking of surface features to derive surging and quiescent glacier velocities (Post et al., 1976; Clarke and Holdsworth, 2002). Subsequent regional reviews have also tended to focus on the surge activity of the various glaciers in the St. Elias

Mountains (Field, 1975; Clarke and Holdsworth, 2002). A summary of all previous measurements of ice thickness, surface velocity and thickness change on glaciers within the study area is given in Figure 1.3 and Table 1.1.

Studies within the last decade have primarily been concerned with quantifying recent changes in thickness, extent, volume and mass of the Gulf of Alaska glaciers (often referred to collectively as ‘Alaskan’ glaciers, even though they incorporate the St. Elias Range in the Yukon). The region is considered particularly vulnerable to current warming because of the effects of rising firn line altitudes on the health of alpine glaciers, and many authors have documented widespread losses in extent, thickness and volume throughout the St. Elias Range and the larger Gulf of Alaska region (Molnia, 2007; Arendt et al., 2002; Arendt et al., 2008; Larsen et al., 2007; Berthier et al., 2010; Barrand and Sharp, 2010; Foy et al., 2011). Berthier et al. (2010) estimate that the Gulf of Alaska glaciers have contributed 24% to the global sea level rise from glaciers and ice caps from 1962-2006. Recent GRACE (Gravity Recovery and Climate Experiment) estimates indicate that the rate of mass loss of Alaskan glaciers exceeds that of all other glaciated regions with the exception of Greenland and Antarctica, at -46 ± 7 Gt a^{-1} from 2003-2010 (Jacob et al., 2012).

It is estimated that the St. Elias-Wrangell icefields on their own lost 21.66 ± 4.4 Gt a^{-1} w.e. from 1962 to 2006 (Berthier et al., 2010). Yukon glaciers experienced a 22% decrease in glacier surface area from 1957 to 2007, corresponding to an estimated total mass loss of 406 ± 177 Gt (8.12 ± 3.54 Gt a^{-1}) when scaled to ice volume (Barrand and Sharp, 2010). On the Kaskawulsh Glacier, Foy et al. (2011) measured changes in glacier extent and surface elevation from aerial and satellite imagery as well as laser altimetry, and estimated total mass loss between 1977 and 2007 to be from 3.27 to 5.94 Gt, with substantial thinning of the terminal area. A small proportion of glaciers within the Alaskan population are thickening or advancing, although these tend to be tidewater or formerly tidewater glaciers in the stable part of the calving glacier cycle. The most notable of these is Hubbard Glacier (Molnia, 2007; Trabant et al., 2003).

With the exception of the studies on Trapridge Glacier, data on the dynamics of glaciers within the Wrangell-St. Elias region have been limited, particularly in the Yukon. From IRRP studies, the ice thickness near the Kaskawulsh-Hubbard Divide was 539 m and the minimum centreline velocity measured was 8 m a^{-1}, increasing to 150 m a^{-1} on the

Kaskawulsh and 132 m a^{-1} on the upper portion of the Hubbard Glacier (Clarke, 1969). The average surface velocity of the upper North Arm of the Kaskawulsh Glacier was measured at ~150 m a^{-1} and ranged from 92 m a^{-1} to 178 m a^{-1} depending on distance along a longitudinal profile (Brecher, 1969). Further downglacier at the confluence of the North and Central Arms, the North Arm centreline velocity was 215 m a^{-1} and the Central Arm centreline velocity was 152 m a^{-1} (Anderton, 1970).

More recently, the surface flow structure of the Upper Seward Glacier has been derived from the use of interferometry (Ford et al., 2003). October surface velocities were low,<100 m a^{-1}, but the basin showed separation into a zone of slow flow (~50 m a^{-1}), and a faster flowing stream along the southern edge of the basin, from West to East, feeding the Lower Seward Glacier. The Lower Seward Glacier feeds the largest lobe of the piedmont Malaspina Glacier, and is a known surge-type glacier. Muskett et al. (2008) indicate that quiescent flow rates are ~0.5-1 m d^{-1}, the lower range of which would be loosely consistent with the results of Ford et al. (2003). Velocities during the active phase may reach 10-20 m d^{-1}. The glacier has been observed through two surge cycles, the last being in 1999-2002, and has an approximate surge periodicity of 30 years.

Hubbard Glacier has been the focus of a significant body of work as a result of unusually rapid advances in 1986 and again in 2002, leading to the temporary damming of Russell Fjord. It is currently in the advance stage of the calving glacier cycle, and it is estimated that it has been advancing since before the end of the 19th century, for a total of 2.5 km since 1895 (Krimmel and Trabant, 1992; Trabant et al., 2003). The velocity structure of the terminal area and changes in the terminus position have been mapped with considerable detail using both ground-based and photogrammetric methods by a research group based at the University of Alaska Fairbanks and the United States Geological Survey (Brown et al., 1982; Krimmel and Sikonia, 1986; Mayo, 1989; Trabant et al., 1991; Krimmel and Trabant, 1992; Trabant et al., 2003; Motyka and Truffer, 2007). The results of Trabant et al. (2003) show winter velocities at a fixed point ~3 km upglacier from the 1997 terminus position to be 6.0 m d^{-1}, a reduction of 1.7 m d^{-1} from the 1978 winter velocity of 7.7 m d^{-1}. The seasonal variation is about 2 m d^{-1}. The centreline velocity at the calving face is greater, at 11.5 m d^{-1} in 1997, and has also shown a deceleration since 1948. Errors are estimated at ±0.6 m d^{-1}. From 1959-2000, they estimate that the glacier increased in volume by 14.1 km^3

with greatest thickening in the lower accumulation area (Trabant et al., 2003). Valerie Glacier, a large tributary entering from the West near the Hubbard terminus has also been the subject of some investigation, as documented speed-ups of this glacier may have had an impact on the closure of Russell Fjord (Mayo, 1989).

There are several glaciers on the continental side of the St. Elias mountains that have active calving faces into lakes or rivers, most notably the Lowell and Donjek Glaciers. The Tweedsmuir and Kaskawulsh Glaciers also calve along parts of their termini. The calving flux of the Lowell Glacier has been estimated at 0.14 km^3 a^{-1} (Burgess et al., 2013).

Thus, while much research has been done in the region over the past 50 years, studies have tended to be fairly localized, and there are large areas remaining that have never been studied. In particular, velocity measurements are scarce, and where they do exist, there have often never been repeat observations to evaluate how velocities may have changed through time. There are many surge-type glaciers that are only known to surge from geomorphological evidence, and their quiescent and surge velocity structure remains unknown. In a region with such a high concentration of surge-type glaciers, dynamics play a large role in regional mass balance, and a fuller understanding of these dynamics and how they change over time is necessary in order to better interpret regional patterns of mass loss estimates. This study will provide a full regional assessment of glacier velocity across the St. Elias Icefield, including the detailed drainage structure of tributary and trunk glaciers. Repeat assessments in 2011 and 2012, derivation of past velocities at selected glaciers, and comparison with previously published measurements, will provide one of the first estimates of variability in glacier motion, and its long term evolution in this region.

1.4 Thesis structure

This is a traditional thesis arranged in chapters. A review of the current state of knowledge regarding the physical basis of glacier motion and its variations is presented in Chapter 2, touching upon the different flow regimes that have been observed in the study area and in the Yukon Territory and Alaska in general. Within this chapter is a discussion of both stable and non-stable flow regimes, and the mechanisms by which glacier velocity may vary on different timescales. Chapter 3 presents the methods by which velocity maps were obtained and their errors evaluated. The results of the analysis are presented in Chapter 4. Regional patterns are discussed first, followed by a basin-by-basin breakdown of the area, in which key glaciers are addressed individually in the context of their flow pattern and magnitude, interannual variations in the velocities measured and, if applicable, surge activity. At the Hubbard and Kaskawulsh Glaciers, velocities are quantitatively compared to key past studies of glacier motion. Chapter 5 presents a discussion of the results presented in Chapter 4, with an emphasis on evaluating surge status and long-term changes to the velocity structure of glaciers in the region. Key findings and suggestions for future research follow in Chapter 6. Tables and figures are presented at the ends of their respective chapters, and references to sources cited in the text are provided in a separate chapter at the end.

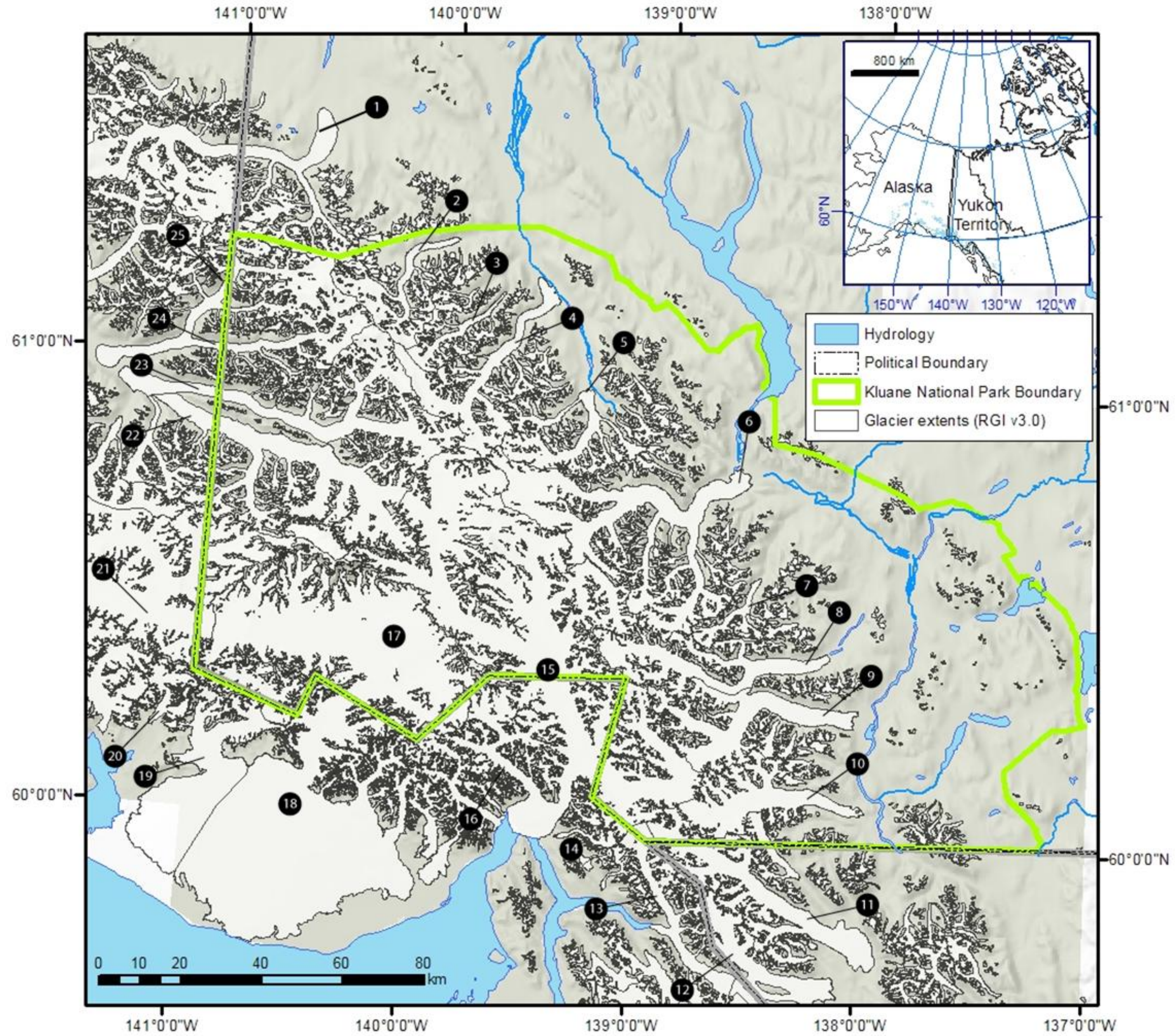

1. *Klutlan Glacier*
2. *Steele Glacier*
3. *Spring Glacier*
4. *Donjek Glacier*
5. *Kluane Glacier*
6. *Kaskawulsh Glacier*
7. *Disappointment Glacier*
8. *Dusty Glacier*
9. *Lowell Glacier*
10. *Fisher Glacier*
11. *Tweedsmuir Glacier*
12. *Vern Ritchie Glacier*
13. *Art Lewis Glacier*
14. *Variegated Glacier*
15. *Hubbard Glacier*
16. *Valerie Glacier*
17. *Seward Glacier*
18. *Malaspina Glacier*
19. *Agassiz Glacier*
20. *Tyndall Glacier*
21. *Bering Glacier*
22. *Logan Glacier*
23. *Walsh Glacier*
24. *Chitina Glacier*
25. *Anderson Glacier*

Figure 1.1: Map of the main glaciers in the study area. Glacier extents are from version 3.0 of the Randolph Glacier Inventory, GLIMS. Hydrologic base layers, Kluane National Park boundary, 500 m hillshade and MODIS 500 m image from Yukon Geomatics.

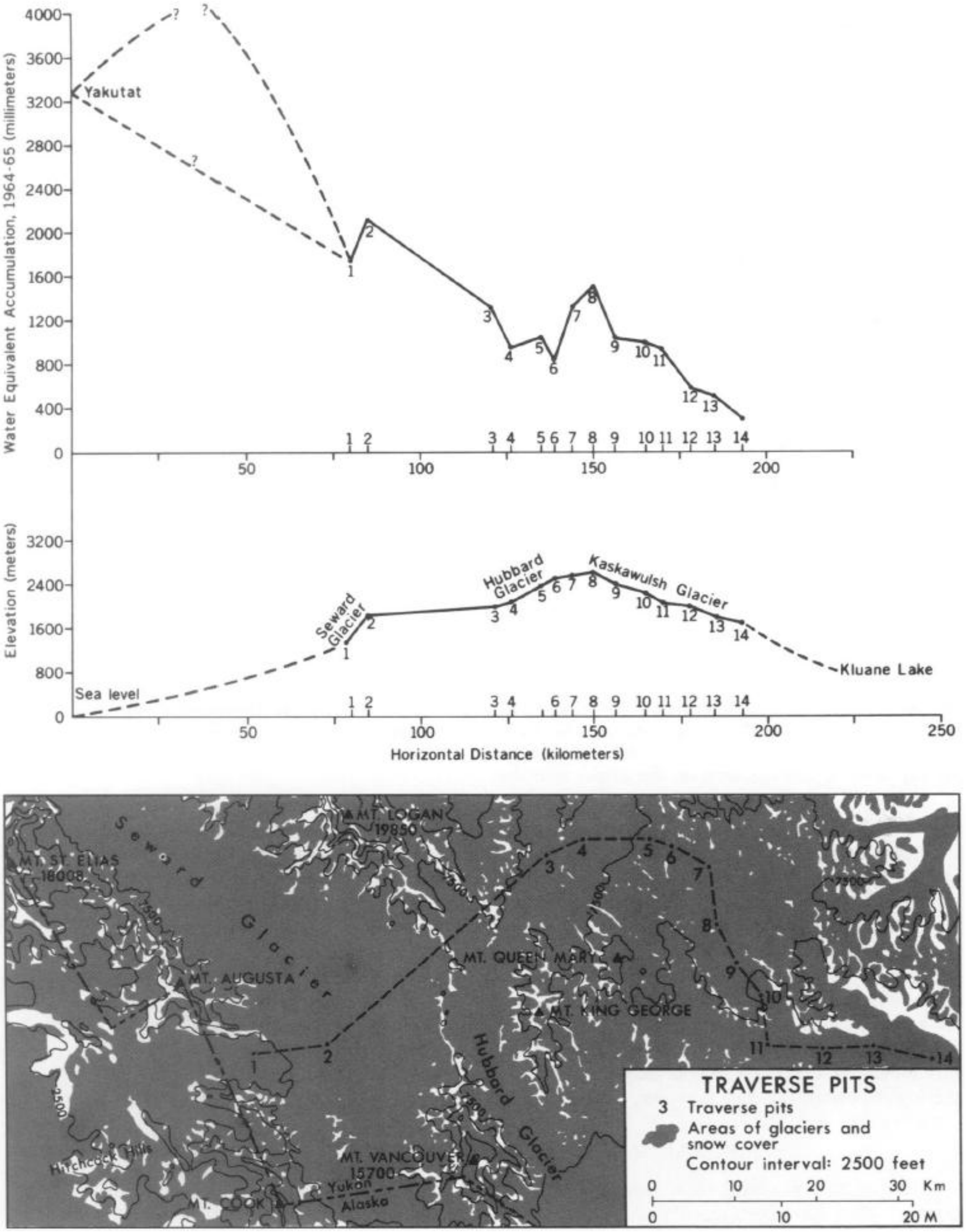

Figure 1.2: 1964-65 water accumulation along the transmountain profile from Yakutat to the Kaskawulsh Glacier. 1965 snowpit sites are numbered. Figure reproduced from Marcus and Ragle (1970).

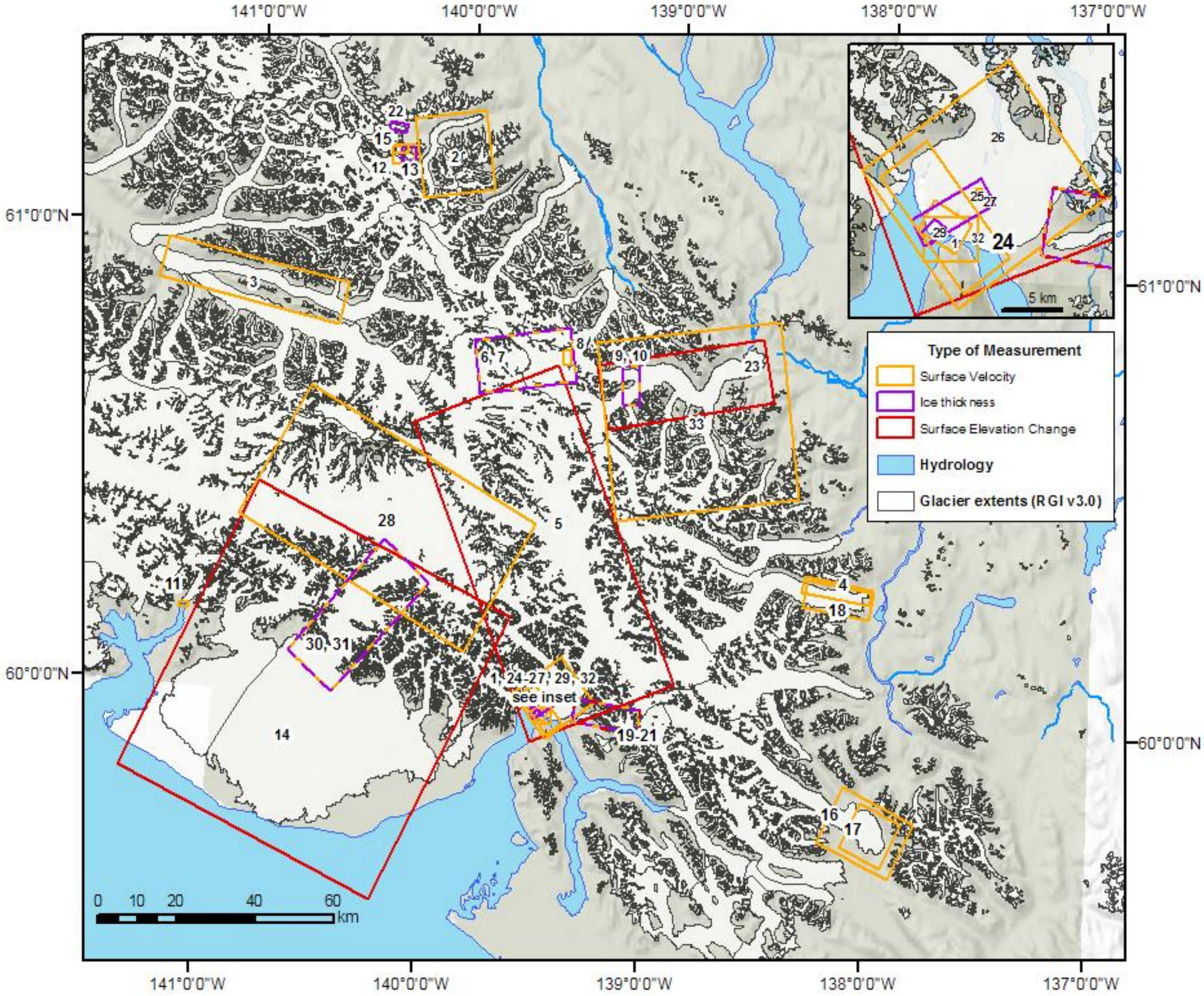

Figure 1.3: Summary of the locations of previous measurements of surface velocity, ice thickness and surface elevation change within the study area. Number labels correspond to the entries in Table 1.1

ID	Year	Measurement method	Reference
Surface velocity			
2	multiple intervals, 1951-1967	air photo feature displacements	Stanley, 1969
3	multiple intervals, 1951-1960		Post, 1966
11	annual 1964-1965		Brown et al., 1982
4	1954-1973	air photo and Landsat-1 feature displacements	Krimmel and Meier, 1975
16	1972-1973	Landsat-1 feature displacements	Krimmel and Meier, 1975
17	1973-1978		Clarke and Holdsworth, 2002
18	multiple intervals, 1973-1983	Landsat 1-4 feature displacements	Clarke and Holdsworth, 2002
1	multiple intervals, 1950-2001	photogrammetry	Trabant et al., 2003
24	summer 1977		Brown et al., 1982
25	multiple intervals, 1978-1997		Trabant et al., 2003
26	summer 1978		Krimmel and Sikonia, 1986
32	summer 2002		Motyka and Truffer, 2007
6	annual 1962-1963	stake survey	Clarke, 1969
8	summer 1964		Brecher, 1969
10	summer 1964		Anderton, 1970
12	1967-1970		Collins, 1972
21	seasonal, each year 1973-1981		Raymond and Harrison, 1988
15	multiple intervals, 1972-2005	stake survey, photogrammetry	Frappe and Clarke, 2007
28	fall 1995	interferometry	Ford et al., 2003
30	autumn 2000	speckle tracking	Headley et al., 2012
33	2009, 2010	speckle tracking, dGPS	Darling, 2011
Thickness			
7	1963	seismics	Clarke, 1969
9	1964		Dewart, 1970
13	1969	radio echo sounding	Clarke and Goodman, 1975
19	1973		Raymond and Harrison, 1988
27	1986		Trabant et al., 1991
22	1976	drilling	Clarke and Collins, 1983
29	1999	bathymetric profile	Trabant et al., 2003
31	autumn 2000	modelled from velocity field	Headley et al., 2012
Surface elevation change			
14	1972-2002	DEM differencing	Muskett et al., 2008
20	each year 1973-1981	stake survey	Raymond and Harrison, 1988
5	1959-2001	altimetry-DEM differencing	Trabant et al., 2003
23	1977-2007		Foy et al., 2011
St. Elias regional studies			
Surface elevation change			
	1957-2009	area-volume scaling	Barrand and Sharp, 2010
	1950s-1990s[1]	altimetry-DEM differencing	Arendt et al., 2002
	1962-2006	DEM differencing	Berthier et al., 2010
Velocity			
	winter 2007-2009	SAR offset tracking	Burgess et al., 2013

[1] extrapolated from altimetry lines on the Kaskawulsh, Hubbard and Seward/Malaspina glaciers

Table 1.1 Summary of previous measurements of surface velocity, ice thickness and surface elevation change within the study area. The ID number corresponds to the number labels in Figure 1.3

Chapter 2: Glacier motion: A Review

2.1 Glacier Velocity and Mass Balance

The primary driver for glacier flow is the mass imbalance between accumulation in the upper reaches of a glacier and ablation in the lower reaches. Increasing thickness above the equilibrium line and thinning below creates a surface gradient which drives flow downslope. The driving stress is commonly considered a product of the mass of the ice column at a given point and the downglacier component of acceleration due to gravity, with surface slope driving the motion rather than the bed slope. For a glacier in steady state (i.e., a glacier where flow is in equilibrium with mass balance such that the glacier maintains a constant geometry), the driving stress is balanced by resistive forces from basal and lateral friction. For such a glacier, the ice flux through any given cross section gate is equal to the cumulative mass balance upglacier. Theoretically the mass flux therefore increases to a peak at the equilibrium line and then decreases towards the glacier terminus. A similar velocity profile is expected to the flux gradient, with the balance velocity describing the velocity required to balance mass inputs and outputs.

Valley geometry will modify this overall pattern of glacier velocity along a centreline. For example, narrow valley constrictions apply lateral compression, which, due to the incompressibility of ice, leads to local thickening and accentuation of the surface gradient relative to downslope. This increases the driving stress and thus increases velocity through the constriction. Irregularities at the bed also translate into velocity variations at the surface, if they are sufficiently large relative to glacier thickness. A rise in the bed topography increases the resistive stress upglacier of that point, which impedes flow and leads to localized thickening. This resultant increase in surface slope relative to the thin ice over the apex of the bump then provides the force necessary to drive the glacier over the bed obstruction. Thus, the thinnest ice coincides with the steepest slope, and greatest velocity (Paterson, 1994). Similarly, localized increases in resistive stress are also found at bends in glacier valleys, and may be associated with velocity variations, often expressed on the glacier surface in the form of crevassing. Due to longitudinal stress coupling, such local variations are ‘felt’ at the surface over distances of several ice thicknesses. More readily-deformable warm ice has a shorter coupling length while cold ice has a large coupling length (Kamb and Echelmeyer, 1986). Over larger distances these longitudinal stress variations probably cancel out such that the largest component of longitudinal stress is accumulation and ablation.

Long-term changes in mass balance would therefore be expected to provoke long-term changes in ice flux, via evolution of glacier velocity, thickness or both. An increase in accumulation would thicken the upper parts of a glacier, increasing the surface slope and thereby increasing the glacier velocity. The consequent longitudinal acceleration (extension) would be expected to be accompanied by vertical thinning, which works to maintain the initial geometry. The terminus may advance to the point where the additional ice flux is removed by increased ablation at lower altitudes. Conversely, mass loss would be expected to decrease velocities, due to the thinning of the glacier column, resulting in decreased driving stress (Heid and Kääb, 2012b). However, observations of glacier velocities in current mass loss environments suggest that the response may be more complex (Moon et al., 2012). Increased thinning in the ablation area in a case where accumulation remains constant increases the overall surface gradient, which may increase flow to the terminus until a new equilibrium state is reached with decreased ice thickness. Then, with less ice mass in the thinned glacier column, the driving stress is less, and the new steady state velocity will be lower, assuming that the degree of perturbation is constant.

The time required for a glacier to reach a new equilibrium state in response to a change in its net mass balance is called the response time, and can be roughly estimated from the mean ice thickness and the ablation rate at the terminus. For maritime temperate glaciers with thicknesses of 150-300 m and terminus ablation rates of 5-10 m a^{-1}, the response time is expected to be on the order of 15-60 years (Paterson, 1994). Examination of long-term trends in glacier velocity should therefore be conducted on similar or greater timescales. However, the reaction time, describing the time elapsed between a mass balance perturbation and when it affects the position of the terminus, may be almost immediate. Such perturbations may propagate downglacier at velocities approximately an order of magnitude greater than the ice velocity, in the form of kinematic waves. At the kinematic wave front, the flux varies at a rate equal to the local mass balance. In the ablation zone, where flow is compressive, the effects of added mass are manifested as a bulge in the surface elevation since there is a greater increase in flux flowing into an upglacier gate than flowing out of a downglacier gate (Paterson, 1994). The localized changes in surface gradient act to dampen the amplitude of the bulge, while lengthening its footprint, in a process called diffusion. The leading edge reaches the terminus more quickly, thus diffusion decreases reaction time, but there is a greater lag before the trailing edge reaches the terminus, so the response time is lengthened (Paterson, 1994). Observations of kinematic waves are difficult to distinguish, but measurements of the downglacier propagation of surge bulges at rates of almost 100 m d^{-1} seem to provide the best evidence (e. g. Krimmel and Meier, 1975). At Variegated Glacier, for example, 'mini-surges' prior to the major 1982-83 surge propagated as waves of high velocity downglacier at a rate of almost 0.3 km hr^{-1} (Kamb and Engelhardt, 1987).

The majority of studies of glacier velocity changes over multi-annual time periods have been focused on the outlet glaciers of Greenland and Antarctica, particularly the tidewater glaciers where acceleration has been pronounced. However, the dynamic response for these glaciers seems to be driven more by reductions in resistive stresses at the terminus and at the bed than by changes in the driving stress from melt-induced evolution of the glacier profile (e.g. Rignot and Kanagaratnam, 2006; Howat et al., 2008; Podrasky et al., 2012). The dynamics of these glaciers are discussed more completely in Section *2.3.2: Calving glacier dynamics*. Moon et al. (2012) measured velocities of almost all Greenland outlet glaciers in 2000 and annually from 2005-2010, including the land-terminating and slower-flowing marine-terminating glaciers. They noted significant variability between glaciers on both annual and decadal scales, with large accelerations of some glaciers and velocity decreases on many others. The majority of land-terminating glaciers, located mostly on the southwest coast, decreased in velocity from 2000-2010. The majority of the large marine-terminating glaciers in the southeast showed marked acceleration from 2000-2005 followed by reductions in the rate of acceleration from 2005-2010, with about 35% of glaciers experiencing decreases in motion to below 2005 levels. Heid and Kääb (2012b) performed a survey of multi-decadal velocity changes of land-terminating glaciers in five regions worldwide, and noted that most glaciers showed deceleration between the periods 1970-1990 and 2000-2010, and that the dominant signal in all five regions was one of deceleration. They were, however, unable to find a correlation with the magnitude of mass balance change, and did not examine the detailed velocity response to mass balance changes.

2.2 Basal Conditions and Glacier Motion

2.2.1 Thermal Regime

The velocity measured at the surface can be considered as the sum of two terms, one component from internal deformation of the ice, and one from basal motion, which can include sliding at the ice-bed interface, or, if the glacier bed is composed of unconsolidated till, deformation of an active till horizon (Figure 2.1, Siegert, 2008). The latter two processes are typically only possible if there is liquid water at the bed, which lubricates the surface for sliding, and weakens the shear strength of deformable sediments. These two processes can permit much greater rates of motion than internal deformation alone. As such, glacier thermal regime, the temperature structure within a glacier, has large implications for the type and magnitude of glacier motion. Glacier thermal regime is broadly climate-dependent, although other factors such as ice thickness and dynamics also play a role. There are three primary categories of glacier thermal regime (Benn and Evans, 2010):

Temperate: in this category ice is everywhere at the pressure melting point, except for a near-surface layer that oscillates between warm and cold ice seasonally. Temperate glaciers generally occur in areas with relatively warm climates that experience high rates of both accumulation and ablation, particularly in maritime temperate mountain ranges. This includes the ranges along the Pacific coast of North America in which the study area is located. High winter snowfall insulates the ice below, which, along with latent heat release within the snow or firn pack from the refreezing of summer meltwater, maintains internal temperatures at or near 0°C in the accumulation zone. In the ablation zone, summer melt removes the surface layer of winter-chilled ice. These glaciers may experience high rates of flow, both in response to water lubrication and the rate of transfer required to balance high accumulation and ablation rates. They may also experience large seasonal variations in velocity, related to meltwater production (Fountain and Walder, 1998).

Cold: in these glaciers, ice is everywhere below the pressure melting point and the glacier is frozen to the bed, meaning that movement is by internal deformation only. This type of glacier is typically small and occurs only in cold, arid climates such as Antarctica, certain parts of the High Arctic, and at very high altitudes. Flow rates are generally very low, <15 m a^{-1} (Van Wychen et al., 2012).

Polythermal: these glaciers comprise zones of both warm and cold ice, although there is considerable variety in the configuration of warm and cold ice zones based on the processes of surface or basal warming or cooling that occur for any given glacier (Blatter and Hutter, 1991). Subsurface heating may occur from strain or friction heating at the base of the glacier in response to motion. Surface heating may arise from the release of latent heat during the refreezing of meltwater within the snow or firn pack. Surface cooling occurs by conduction or convection of heat out of the glacier during winter. Polythermal glaciers may be further classified as 'warm polythermal' or 'cold polythermal' depending on which type of ice is dominant. Within the study area, there are several glaciers that have been identified as polythermal from borehole measurements or inferred as such through indirect means, notably Trapridge Glacier (Clarke et al., 1984).

2.2.2 Types of motion

(a) Internal deformation

Internal deformation refers to the deformation of individual ice crystals and the movement of the crystals past each other in response to an applied stress (Benn and Evans, 2010). Laboratory and field measurements of strain rate for glacier-typical stresses have shown that ice deformation can be described by a function of the form:

$$\varepsilon_{xy} = A\tau_{xy}^{n}$$

where ε_{xy} is the strain rate, τ_{xy} is the shear stress and A and n are flow parameters. This relationship is commonly called Glen's flow law after Glen (1958). A is dependent on ice temperature, crystal structure and impurity content, and n is usually taken to equal 3, although this value could be less for cold ice (Paterson, 1994). There is a large dependence on temperature, as ice is brittle at low temperatures but deforms readily when at its pressure melting point because intergranular water facilitates creep (Benn and Evans, 2010). However, Glen's flow law implies several key assumptions. It describes simple shear, as might be experienced close to the bed of a glacier, but for most of the ice body, strain operates in two or three dimensions, and the component of deformation in a given direction may be some fraction of the value assuming simple shear (Paterson, 1994). In addition, the theoretical assumption of Glen's flow law that glacier ice is essentially isotropic and homogenous is probably inaccurate (Paterson, 1994). Impurities such as dissolved compounds and silt bands tend to increase the creep rate, while sand-sized material or coarser tends to stiffen ice and lower the creep rate (Paterson, 1994) As it deforms, basal ice progressively develops a preferred crystal orientation, which eventually enhances further deformation near the base of the ice column. Field observations have suggested that this basal ice may be more deformable than the uniform isotropic ice assumed by Glen's flow law (Hubbard and Sharp, 1989), although there have been few field studies to assess this in detail.

(b) Basal sliding

Studies suggest that sliding over an impermeable bedrock bed is primarily enabled by a thin water film at the ice-bed interface that supports normal stresses, but insignificant shear stresses. Drag therefore mainly occurs because of undulations in the bed topography, which create compressive stresses on the upslope side, as in Figure 2.2 (Paterson, 1994). A stress gradient is formed around a bedrock obstruction, with an upslope compressive force that must be balanced by a downslope area of reduced stress (Willis, 1995). Motion over such obstacles occurs by regelation (most effective over small obstacles), enhanced creep (most effective over large bumps), and the formation of subglacial cavities, once basal water pressure exceeds a threshold pressure called the separation pressure.

Regelation moves ice over obstacles as a thin film of pressurized water, melted from the high-pressure upslope side, driven over the bump by the pressure gradient, and refrozen in the lee of the obstacle. The latent heat of fusion released from this refreezing is conducted through the bedrock bump to the upslope face, providing heat for further melting (Weertman, 1957). It is most effective where bedrock obstructions are small, so that heat can be efficiently conducted from the downslope to the upslope face. Although the existence of this process is not disputed, its impact on sliding velocity is likely very small, only about 1 cm a^{-1} for realistic values of shear stress and bed roughness of 1 m (Fowler, 2010). Enhanced creep occurs because of the greater stresses in the vicinity of a bed obstruction that promote larger strain and facilitate deformation around the obstacle. Because the velocity is dependent both on the magnitude of the stresses acting on the ice and the distance over which those stresses act, enhanced creep is most efficient for larger obstacles.

The initial sliding laws developed by Weertman (1957) and mathematically refined by Nye (1970) and Kamb (1970) were based on the premise that for a generalized bed, sliding is at a minimum when the sliding velocity component due to regelation is equal to the component due to enhanced creep. In other words, sliding is controlled by bedrock obstructions of some intermediate size, a ‘controlling obstacle’ (Paterson, 1994). This model was thus very sensitive to a bed roughness parameter. However, because this model was based only on basal shear stress and bed roughness and thus described sliding by regelation and enhanced creep only, neglecting cavitation, the model assumed that for a given glacier bed, sliding velocity remains constant if the basal shear stress does not change. It therefore cannot explain observed short-term variations in velocity (Paterson, 1994). Lliboutry (1968) identified early on that the opening of basal cavities was a probable consequence of glacier sliding, and furthermore, that cavitation was necessary to explain the magnitude of sliding observed as well as its variations. The stresses produced by Weertman’s (1957) model using a roughness value consistent with observed glacier velocities exceeded the shear strength of ice and would result in ice fracturing, which was obviously unrealistic (Fowler, 2010). Lliboutry thus proposed that a sliding law should include this third process, cavitation, dependent on effective pressure (= ice overburden pressure – basal water pressure).

Effective pressure can be extremely variable on short time scales, and thus is capable of explaining variations in sliding velocity. Low effective pressure (high basal water pressure) facilitates the formation of basal cavities. These cavities allow for greater velocities because the shear stress must be supported by a smaller area of the bed (Willis, 1995). The opening of cavities commences once basal water pressure reaches a critical value, called the separation pressure. Cavitation is facilitated by the hydraulic jack mechanism: water inside cavities exerts a downglacier force on the upslope-oriented ice face of the cavity, increasing the sliding velocity, and promoting cavity growth (Iken et al., 1983). Cavities are kept open by sliding, and are closed by downward creep closure. They thus carry a water flux most effectively at high basal water pressure, which maintains glacier sliding, and lowers effective pressure so that creep closure is slower (Willis, 1995).

Sliding theory is still under development, and there exists no satisfactory theoretical sliding law relating basal shear stress, water pressure and sliding velocity. Instead, empirically-derived ad hoc relationships, usually of the form $u_b = k{\tau_b}^m N^{-n}$, where u_b is the sliding velocity, τ_b is the basal shear stress, N is effective pressure, and k, m, and n are adjustable parameters > 0, are relied upon (Budd et al., 1979; Bindschadler, 1983; Paterson, 1994). The dependence on roughness is captured in the constant *k*, which is dependent on ice properties and inversely proportional to bed roughness (Paterson, 1994). However, they are not ideal. Schoof (2005), following Iken (1981), shows that these relationships allow unrealistically high shear stresses to be generated at the bed, when in fact cavitation imposes an upper bound on the upslope compressive stress by limiting the minimum downslope stress to the separation pressure. This limit is controlled by the steepness of bed obstacles, and since drag on a sliding glacier is provided solely by the upglacier normal stress produced by bed obstacles, this bound effectively limits the basal drag that a given glacier bed is able to produce. The implication is that basal drag cannot increase continuously with driving stress, and where driving stress exceeds the drag produced by the bed, longitudinal and lateral stresses become significant in maintaining force balance. It thus cannot be assumed for a given point on the glacier bed that driving stress is equal to the basal shear stress (Schoof, 2005).

It is worth noting a couple points pertaining to the bed assumptions made in most sliding models. They generally assume a clean ice-bed interface, and so neglect both debris-rich ice near the bed and till pockets on a bedrock bed. The friction existing between debris-rich ice and the bed may dissipate up to 30% of energy in abrasion (Paterson, 1994). Sliding velocities calculated from theory may therefore be too high. Secondly, bed roughness is not necessarily a fixed parameter, but is itself influenced by the shear stresses at the bed. Lliboutry (1968) observed that basal shear stress tends to be constant in the range of 100 kPa, suggesting that the bed evolves to a typical roughness. If the bed is too rough, then shear stress will be very high, and lead to plucking and redistribution of the bed mass into hollows, smoothing the bed. A smooth bed will develop its own roughness as low shear stress must be balanced by high longitudinal extension, which induces stresses high enough to rupture the ice and/or the bed, creating obstructions in both hard and soft beds (Fowler, 2010).

(c) Subglacial deformation

The above discussion has addressed sliding on impermeable bedrock beds, upon which sliding theory was largely developed. However, given the glacial capacity for erosion, it is more likely that glaciers partially or completely overlie soft sediments (Alley, 2000). In this case, basal motion can also result from the deformation of a sediment layer under the glacier. Unfortunately, subglacial till is much more difficult to parameterize. Till rheology is dependent on a relatively large number of parameters, most of which, such as porewater pressure and basal shear stress, are difficult to directly measure.

At high effective pressures, ice can infiltrate the pore spaces of sediment, effectively reducing the potential for sliding at the ice-till interface to zero (Boulton and Hindmarsh, 1987). However, till becomes softer than ice when saturated with water, and can shear efficiently, accounting for large percentages of the velocity at the surface (e.g. Boulton and Jones, 1979). Subglacial deformation occurs when the basal shear stress exceeds the yield strength of the till, which is dependent on the cohesion of the till as well as the effective pressure (= hydrostatic pressure – porewater pressure). High porewater pressure and high porosity both weaken till. Additionally, till is a dilatant material, meaning that it expands as it deforms, as the particles are rearranged in such a way that porosity is increased (Paterson, 1994). Therefore, initial deformation can be amplified in a positive feedback. Once deformation is sufficiently reduced, a dilated till tends to deflate and recompress (Paterson, 1994). Favorable conditions for till deformation require large amounts of water that sufficiently reduce the effective pressure for the yield strength to drop. Therefore, subglacial deformation is more likely to be important if there is an appreciable water supply from the surface and poor drainage (both in the subglacial drainage system and due to the permeability of the basal sediment). Deformation thus depends on shear stress, effective pressure, porosity, volume fraction of fines, and strain history. These characteristics likely change with time. In fact, where measurements exist, subglacial deformation appears to be variable in both space and time, leading to significant difficulty in deriving a suitable till flow law relating shear stress and deformation (Alley, 2000). It is also possible that lateral and longitudinal stress coupling become important in linking areas of high deformation to ‘sticky spots’ that support most of the stress. These may be patches of ice frozen to the bed, or areas of coarse till that have a high yield strength (Alley, 2000). Finally, deformation moves material downglacier, so for subglacial deformation to persist, the supply of fresh material through erosion must be maintained.

It is often assumed that deformation occurs along relatively narrow shear bands near the ice-till interface where water inputs are presumably highest. However, there is also some evidence for pervasive or deep deformation. If we take the simple assumption that deformation is highest where porewater pressure is highest, then variations in water pressure at the ice-till interface that propagate down into the till could create conditions where the depth of greatest water pressure is not only not at the till surface, but also changes with time (Alley, 2000). At Black Rapids Glacier in Alaska, for example, till deformation appears to occur at a depth of several metres, beneath a stiff consolidated till horizon (Truffer et al., 2000). At Breiðamerkurjökull in Iceland, the subglacial environment was instrumented to allow synchronous observations of strain rates at various depths in the subglacial sediment, water pressure and 3-dimensional ice displacements (Boulton and Hindmarsh, 1987). The results indicated a stratified structure where most motion occurred in a 40-60 cm thick dilated, deforming layer overlying a second horizon of more consolidated rigid sediment. Trapridge Glacier in the Yukon Territory is another of the few subglacial environments that has been instrumented (Blake et al., 1992, Fischer and Clarke, 2001). Their results showed a deforming layer of approximately 30 cm thickness, with significant variability between measurement years, and across the glacier bed.

Till flow laws have been empirically derived, and either treat till as a plastic-Coulomb material where the strain rate is independent of stress above a critical yield strength, or a linear-viscous material where the strain rate increases nearly linearly with stress. Both theories have some degree of observational support (Alley, 2000).

2.2.3 Subglacial drainage and its impact on velocity

Water pressure at the bed is strongly affected by the mode of subglacial drainage, and short-term (seasonal and intra-annual) velocity variations have been linked to the evolution of the subglacial drainage system by a large and growing body of field observations and modelled evidence. A summary of the primary forms of drainage for hard and soft bedded glaciers is given below.

Meltwater is typically routed from the surface to the glacier bed through englacial channels and moulins or crevasses. In the accumulation zone, transit times to the bed are generally greater than in the ablation zone due to water storage in the firn or snow pack. However, increases in basal water content in response to increases in surface melt occur relatively rapidly, on the order of minutes to days, especially if pathways from the surface to the glacier base have been previously established (Fountain and Walder, 1998; Tedesco et al., 2013). Basal drainage systems are commonly conceptualized as either ‘distributed’ or ‘discrete/channelized’ (or ‘slow’ and ‘fast’, respectively, preferred by Fountain and Walder, 1998).

Discrete channelized systems are efficient at draining water from the basal system, and are composed of an arborescent network of subglacial channels incised either upwards into the overlying ice (Röthlisberger ‘R’ channels) or downwards into the underlying substrate (Nye ‘N’ channels in bedrock, and ‘Tunnel Valleys’ in sediment), with R-channels thought to be more common (Fountain and Walder, 1998). These channels exist in general equilibrium with closure by inward creep of the ice and enlargement by melt and outward water pressure. Röthlisberger (1972) quantitatively modeled the hydraulics of subglacial channel flow. One of the properties of his model is that the greater the discharge from the channels, the lower the pressure, meaning that larger channels tend to capture the water flux of smaller channels, leading to the development of a subglacial drainage network which focuses water flow into a small number of outflow streams at the terminus. Channelized systems thus cover a small area of the glacier bed relative to the volume of subglacial water, and small changes to the total channel volume can represent large changes to water discharge. On soft beds, channels may also form upwards into the ice, and will be low pressure systems if they tend to enlarge upwards as opposed to laterally along the bed (Willis, 1995)

In distributed systems, larger areas of the bed are hydraulically connected. Drainage is less efficient, with longer transit times due to temporary storage and a more tortuous route to the terminus. Distributed systems may take a variety of forms including a water film at the ice/bed interface, processes of water flow through a deformable sediment bed, or a linked cavity system as described by Kamb (1987) (Fountain and Walder, 1998; Benn and Evans, 2010). This linked cavity system is thought to be composed of cavities, ~1 m in vertical height and with horizontal dimensions of ~10 m that form in the lee-side of bedrock bumps or anchored boulders from the motion of ice over these features. These cavities are connected by narrow channels, termed orifices, which are thought to contain water at high pressure and serve to control (“throttle”) water flow through the system. Much of the flow is diverted laterally as opposed to down-glacier, as cavities have a tendency to form in step- or wave-like depressions in the bed, and are often oriented transverse to the direction of ice flow, as shown in Figure 2.3a (Kamb, 1987). Distributed drainage systems are higher-pressure systems than channelized drainage systems, because of the constriction of water flow by these narrow channels. In contrast to the inverse relationship between water pressure and discharge in channelized systems, basal water pressure in cavities increases with water flux, because high water discharges must be accommodated though enlarging the cavities, which requires high pressures (Kamb, 1987).

The spatial extent of both types of subglacial drainage system may vary with water inputs and the amount of water storage, and both types of system can exist beneath a single glacier (Nienow et al., 1998; Schoof, 2010). Seasonal shifts between the type of drainage system are fairly well documented, and reflect changes in the availability of meltwater (e.g. Iken and Truffer, 1997; Nienow et al., 1998). As temperatures cool in fall, there is less water flowing through the discrete-system channels, and this decrease in water flux enables closure by ice creep to become dominant. This is thought to cause the channel system to collapse, leaving a distributed drainage system throughout the winter. The onset of melt in the following spring and summer introduces large amounts of water from the surface to the bed, which destabilizes the distributed system, leading to the progressive formation of a channelized system at the expense of the distributed system (Benn and Evans, 2010). Nienow et al. (1998), through the use of dye-tracing experiments on the Haut Glacier d'Arolla in Switzerland, determined that the spring shift from a distributed to a channelized system starts in the ablation zone where water production is more sensitive to temperature changes (due to the lower albedo of bare ice compared to snow), and where there is rapid transit of surface meltwater to the bed due to the lack of temporary water storage in a snow or firn pack. Thus, efficient channel development migrates upglacier with the snowline as the melt season progresses.

The switch from a winter distributed system to a summer channelized system was observed in detail at Bench Glacier in the Chugach Range in Alaska in 2002 by Anderson et al. (2004). There were two spring acceleration events separated by approximately 2 weeks of steady high flow. After the second acceleration event, the glacier decelerated to a value less than the steady episode, and maintained this low velocity for the remainder of the melt season. The vertical uplift record of bed separation recorded a similar pattern, with a period of uplift during the first acceleration event followed by maintenance of high bed separation for the period before the second acceleration event. The second acceleration event was marked by further surface uplift before a slow decline to zero. The termination of the second acceleration event was accompanied by a tripling of the stream discharge. The authors were able to model their observations with excellent agreement, up to the termination of second acceleration event, when they had to impose a drop in water pressure to achieve the observed decrease in velocity. They interpreted this as the opening of an efficient channel.

Anderson et al.'s (2004) interpretation of the series of events is based on the balance between the opening of subglacial cavities by glacier sliding and their closure by creep. An increase in meltwater increases the basal water pressure, which increases basal sliding. This increase in horizontal movement enlarges both the cavities and the narrow orifices connecting them. In order for the period of stable high velocities to be maintained, water pressure (and therefore water input) must be low enough that creep closure of the orifices is sufficient to maintain the stability of the cavity system. Large water inputs would lead to unstable sliding that would enlarge the orifices to the extent that they would develop into channels to efficiently evacuate the water flux, as occurred during the second period of acceleration that was triggered by a couple of high melt days. The authors observed the spring dynamic behaviour of this glacier in a previous year, when one acceleration event was sufficient to spawn the development of an efficient channelized drainage system, and they judge that the extended 2-week period of stable high velocities is a relatively rare occurrence, requiring that melt input and sliding velocity remain within a narrow range. This conclusion implies that stable high-velocity sliding may not be a feasible response to meltwater inputs, unless under relatively specific conditions.

The model used above by Anderson et al. (2004) was unable to predict the decrease in water pressure associated with the switch to a channelized subglacial drainage system; it had to be manually imposed. However, Schoof (2010) developed a numeric model that is able to capture this channelizing instability, and explain most of the velocity and water pressure variations associated with it based on the concept that the viability of both channels and cavities can be taken as a balance between the opening rate (by wall melt and glacier sliding, respectively) and the closure rate (by creep). Plotting opening and closing rates indicates two stable nodes. The cavity state occurs at low water flux (Q) and is associated with effective pressure (N) decreasing Q. The other stable state, where N increases with Q, is the channel state (figure 2.5). At a critical Q, discharge concentrates into a few channels, driven by wall melting. Below this value, all conduits can be stable at the same size.

There are several interesting features of Schoof's (2010) analysis: first, that the critical discharge to return to a cavity system is much lower than the critical discharge required to develop the channel system. This means that channels, once formed, can remain open for some time even if the water flux through them decreases. This means that efficient drainage can be maintained throughout a melt season, despite small fluctuations in the meltwater input. This is consistent with observations on valley glaciers and the large ice sheets of velocity minima in late summer (Darling, 2012) and/or steady or decreasing annual velocities in spite of increased mean melt (Van de Wal et al., 2008; Sundal et al., 2010). More important than mean melt to short-term glacier velocity, according to Schoof (2010), is short-term variations in melt inputs, because the channelized system may still be overwhelmed by large rapid (<1 day) inputs of melt water, given that the channel size adjustment to changes in water flux occurs on a scale of several days. Mid-season summer high velocities are therefore more likely to be associated with discrete acceleration events, caused by abrupt draining of supraglacial lakes, rain events or strong diurnal melt cycles. This result is supported by observations on the Greenland Ice Sheet that abruptly-draining supraglacial lakes have a much more appreciable effect on glacier velocity than slow lake drainages (Tedesco et al., 2013). It seems that effects on velocity require water inputs at a rate that exceeds the capacity of the subglacial drainage system to adapt. Both the configuration of the drainage system and the rate of water input are important in determining the velocity response. Furthermore, such acceleration events may be followed by 'extra-slowdown events', where the creep closure of channels occurs more slowly than the decrease in water input so that for a short period of time following an acceleration event, the conduits exist at anomalously low water pressure (high effective pressure) and surface velocity falls to below what it was initially before the acceleration event (Podrasky et al., 2012). These slow-down events may compensate for short periods of accelerated flow in the annual flux balance, so that mean annual velocity does not show a long-term response to increased melt.

2.3 Non-stable Glacier Regimes

2.3.1 Surge dynamics

(a) Surge characteristics

Glaciers typically experience steady downslope displacement. However, a small proportion of the world's glaciers experience cyclic variations in motion and are termed surge-type. These glaciers are characterized by alternation between periods of slow flow, termed quiescence, and shorter periods of much faster flow (from 10-1000 times the quiescent flow rate), sometimes accompanied by significant terminus advance (Meier and Post, 1969; Murray et al., 2003). Such advances are not indicative of mass gain, but rather of mass redistribution, from the upper reservoir area that experiences gradual thickening during quiescence, to the receiving area down-glacier (e.g. Raymond and Harrison, 1988). Surges are generally accompanied by a surface lowering in the reservoir area of tens to hundreds of metres (Meier and Post, 1969; Frappé and Clarke, 2007).

The stresses associated with rapid acceleration, flow and deceleration typically result in heavy and chaotic surface crevassing, which usually enables ready identification of glaciers in the active surge phase. Surging may also be accompanied by large terminus displacements, sheared-off margins and tributaries, and bulging or overriding of medial or terminal moraines (Meier and Post, 1969). Certain features, notably looped and folded moraines in the ablation zone, are produced during a surge but persist during quiescence, permitting the identification of surge-type glaciers from aerial or satellite imagery. During quiescence, large portions of the receiving area may become stagnant; leading to downwasting with associated thermokarst features such as a deeply potholed or heavily debris-covered surface, and incised supraglacial channels (Stanley, 1969).

Fewer than 1% of the world's glaciers are surge-type, and this population shows strong regional clustering, with particular concentrations in northwestern North America, Svalbard, the Canadian High Arctic and the Pamir and Karakoram ranges (Murray et al., 2003; Copland et al., 2003; Kotlyakov et al., 2008; Copland et al., 2011). Post (1969) identified 204 surging glaciers out of several tens of thousands in western North America from the Brooks Range in northern Alaska to California. All surging glaciers were located in the Alaska Range, Chigmit, eastern Wrangell and St. Elias Mountains. Within these ranges, there is also a tendency for surge-type glaciers to cluster within basins (Frappé and Clarke, 2007). A notable example within the study region is the Steele Valley system, where not only has the Steele Glacier been observed to surge, but also the smaller Hazard, Backe, Rusty and Trapridge Glaciers, all within close proximity (Collins, 1972; Stanley, 1969). There is also evidence for a relationship between trunk and tributary glacier surging, whereby surging of a trunk glacier may initiate surging of its tributaries by mass drawdown. The inverse situation, where a tributary surge triggers a surge of the trunk glacier it feeds, appears to be rarer (Clarke, 1991). However, Kotlyakov et al. (2008), in a study of compound surge-type glacier systems, observed several cases of tributary advances causing partial damming of trunk glaciers, leading to mass build-up over several years in the trunk glacier directly upstream of the confluence and subsequent surging of the trunk in response to the additional mass loading.

Surge-type glaciers in Alaska and Svalbard have significantly different characteristics in terms of the duration of their active and quiescent phases and the overall structure of the surge evolution through time. Meier and Post (1969) described the typical characteristics of Alaskan-type surging glaciers. The average length of the active phase is 1-3 years, although surges of only a few months are also common (Eisen et al., 2005, Bevington and Copland, submitted 2013). Maximum velocities during the active phase can reach 5 m hr^{-1}, for short periods of time, and tend to be highly variable. Deceleration at the conclusion of the active phase is rapid. The duration of the quiescent phase can be from ~15 years to >100 years, and is commonly ~20-30 years. The most extensively-studied and widely-cited example of a typical Alaskan-type surging glacier is Variegated Glacier, a temperate valley glacier in the St. Elias Range in Alaska. Kamb et al. (1985), studying the 1982-83 surge of this glacier, measured peak velocities of 65 m d^{-1}, a 100-fold increase over quiescent velocities. The surge started in the upper portion of the glacier and propagated down-glacier. Termination of the surge was rapid; occurring over several hours only, and was accompanied by outburst flooding.

In contrast, Svalbard-type surge glaciers exhibit a periodicity ranging from 50-500 years. The active phase comprises a 3-10 year period of increasing flow rates followed by a long period (up to ~20 years) of gradual deceleration before re-entering quiescence. Maximum flow rates are generally an order of magnitude less than those of the Alaskan-type surges (Murray et al., 2003). Surges of Svalbard-type surge glaciers have been known to propagate either up- or down-glacier, while the Alaskan-type is characterized by down-glacier propagation of the surge front. The evolution of the two types of surges through time is presented in Figure 2.5, which clearly indicates the difference in surge magnitude and duration and the differences in the speed of surge onset and termination.

These points of contrast led Murray et al. (2003) to conclude that different mechanisms must be operating behind the surges of these two glacier populations, with possible links to the differing climates of Svalbard and the Gulf of Alaska and their impacts on glacier thermal regime. This conclusion is complicated by the assertion that Trapridge Glacier, as well as a small unnamed glacier nearby, in the Yukon Territory has once, and possibly more than once throughout the history of its observed surges, experienced a “slow surge” more like the Svalbard-type than the Alaskan-type more common in the Yukon St. Elias region (Frappé and Clarke, 2007; Flowers et al., 2011). In particular, Steele Glacier, a larger valley glacier within the same drainage basin as Trapridge Glacier, is a surge-type glacier whose surges match the characteristics of the Alaskan-type (Stanley, 1969). It seems that both surging mechanisms can exist in close proximity (as noted also in East Greenland by Jiskoot and Juhlin, 2009). The relative size of Trapridge Glacier to other ‘typical’ Alaskan surge-type glaciers, including the neighbouring Steele, may be important. Because it is small and thin, part of the glacier is frozen to the bed, giving it a polythermal structure that is not inconsistent with the Svalbard population of surge-type glaciers.

(b) Surge mechanisms

Discussion of the mechanisms of glacier surging generally falls into two categories: (a) the process of initiation of the active phase of a surge cycle (the ‘switch’ mechanism) and the mechanisms permitting short-term rapid flow, and (b) the factors determining whether a given glacier experiences ‘normal’ flow, or flow by surge cycles. Concerning the former, subglacial water has long been considered a key element in enabling a glacier to decouple from its bed and permitting rapid flow (e.g. Stanley, 1969). Observations of ‘plug flow’ – the movement of ice *en bloc*, with minimal change in the position of surface features relative to each other, and strong shearing at the margins, as well as comparison of surface velocities with calculated velocities assuming ice creep only, indicate that motion during the active phase is primarily a result of basal processes. This can take the form of either sliding or subglacial deformation, depending on the nature of the ice/bed interface and subglacial water pressures (Murray et al., 2003; Harrison and Post, 2003). There is evidence to suggest that surge initiation is related to some critical mass accumulation in the reservoir area, and is thus linked to snowfall (Kamb, 1987). Eisen et al. (2001) present compelling support for this. Their study estimated mass balance at a point in the accumulation zone during the quiescent periods preceding the last three surges of Variegated Glacier in Alaska (1965, 1983, 1995). Their results indicate that the interval between surges represents the time required for cumulative accumulation to reach a critical value, ~43.5 m ice equivalent for Variegated Glacier. Estimates of this value for the three periods agree closely, with 1 standard deviation representing 1.2 m ice equivalent (Eisen et al., 2001). The 1995 surge was shorter than the previous observed surges, and appeared to be prematurely terminated before the reservoir area was depleted, after two days of record-level melt introduced large volumes of water into the system. It was predicted that the next surge would occur after a shorter-than-average time interval as a result, which was borne out when the glacier next surged in 2003-04, with a cumulative mass accumulation from 1995-2003 of only ~24 m ice equivalent (Harrison et al., 2007)

There are two main models describing the mechanisms that initiate glacier surging. Kamb (1987) developed the 'linked-cavity' subglacial drainage system model of surge initiation and development following observations of the 1982-83 surge of the temperate Variegated Glacier. The essential element to explain the difference in ice velocity between the quiescent and active phases is a switch in the subglacial drainage system from a low-pressure channelized system to a high-pressure linked cavity system as described in Section 2.2.3. Borehole measurements prior to, during, and after the surge showed a strong correlation between basal water pressure and the observed surface velocities (Kamb et al., 1985). Higher pressures cause an increase in basal sliding, by reducing friction at the bed and favouring the formation of subglacial cavities. Theoretically, at subglacial water pressures higher than the ice overburden pressure, there would be complete decoupling of the glacier from its bed and surface velocities would increase accordingly. The linked cavity system as conceived by Kamb (1987), unlike a discrete channelized system, is stable at high basal water pressures and under conditions of rapid basal sliding, permitting rapid ice motion.

Kamb et al. (1985) argue that surge initiation requires high basal water pressures, produced by the collapse of the channelized subglacial drainage system. They suggest that the build-up of ice thickness in the reservoir area during quiescence would explain the initial collapse of the tunnel system, trapping water and leading to an increase in basal sliding. As the surge front progresses downglacier, it simultaneously collapses the discrete tunnel system and develops the linked cavity system, creating the conditions of high basal water pressure that maintain and enhance the rapid rate of basal sliding.

Kamb (1987) quantitatively showed that the stability of the linked cavity system is dependent on the behaviour of the orifices rather than the cavities. For high basal water pressures to exist, orifices must be narrow, throttling the water flow through the system. If they begin to enlarge unstably, such as by frictional melt caused by the flow of pressurized water through them, it may lead to the development of a more efficient channelized system. This would simultaneously reduce subglacial water pressure and evacuate basal water in outburst flooding. He suggests that this situation is likely what occurs during surge termination. However, his model demonstrates that the characteristics of bed roughness and slope have a significant effect on the stability of orifices, and likely impact a glacier's tendency to surge; that is, whether a given glacier experiences motion by surge cycles or normal steady downslope flow.

Fowler et al. (2001) offer a model for thermally-controlled glacier surging, derived from observations in Svalbard and the polythermal Trapridge Glacier. Unlike Variegated Glacier, borehole observations at these locations indicate 'soft' sediment beds actively deforming under subglacial stresses (Clarke et al., 1984; Fischer and Clarke, 2001; Murray et al., 2003). In addition, observations suggest minimal amounts of surface meltwater reaching the bed of polythermal Svalbard glaciers (Murray et al., 2003). The description of 'thermally-controlled' rests on the supposition, based on field observations of Bakaninbreen Glacier in Svalbard and Trapridge Glacier, that such glaciers are cold-based and frozen to their beds during quiescence, but warm-based during the active phase. The switch to warm-based ice occurs in response to thickening of the ice during quiescence. Such mass build-up better insulates the bed from cold atmospheric temperatures, leading to the production of basal meltwater. Increased pore water pressure weakens the underlying sediment, leading to deformation and increasing velocities. Deformation of the till layer increases frictional heating and melt, thereby increasing the basal water content and further weakening the sediment. Therefore, there exists a positive feedback between basal meltwater production, the shear strength of the sediment, and sediment deformation, the result of which is rapid basal motion. These processes may propagate along the glacier length with the surge front. Surge termination occurs when thinning of the ice due to mass redistribution is sufficient to raise the pressure melting point of the basal ice and increase the conduction of heat out of the glacier. Refreezing of the glacier to its bed halts the rapid basal motion and signals reentry into quiescence (Fowler et al., 2001; Murray et al., 2003).

2.3.2 Calving glacier dynamics

Calving glaciers behave semi-independently of climate, with variations often unrelated to the regional pattern of mass gain or loss, and disproportionate to the climate signal, although over multi-decadal to century timescales, they do seem to respond to shifts in climate. Currently, there are more tidewater glaciers experiencing retreat than advance, which is unlikely to occur if tidewater glacier dynamics were entirely independent of climate, given that the advance phase lasts much longer than the phase of rapid retreat (Post et al., 2011)

The tidewater calving glacier cycle was first elaborated by Post (1975), based on reconstruction of historic terminus changes of Columbia Glacier, Alaska. Calving glacier stability is dependent on conditions at the ice front. Over annual timescales, the calving rate seems to increase with water depth at the terminus; therefore, advance of a calving glacier into deep water is prohibited by increases in the calving rate. Advance occurs as the glacier pushes its terminal moraine further down the fjord, by the redeposition of material eroded from the upglacier slope of the moraine onto the lee side. The rate of advance is thus controlled by the availability of material and the rate of moraine rebuilding, and is usually in the range of 20-40 m a^{-1} (Meier and Post, 1987). During advances, velocities are moderate and the calving rate is relatively low (Post et al., 2011). Under these conditions, thickening and deceleration at the terminus is possible. This has been observed at Hubbard Glacier, where velocity measurements over almost 50 years indicate that the glacier is decelerating by ~0.05 m a^{-2} (Trabant et al., 2003). Advance will continue as long as there is sufficient ice flux out of the accumulation area to sustain it; typically when the accumulation area ratio (AAR) is greater than 0.65-0.7 (from Alaskan examples, Trabant et al., 2003) up to 0.8 (Post et al., 2011). Continued advance enlarges the ablation area, reducing the AAR. After this point, losses from melt and calving may begin to exceed ice replenishment, which can instigate the retreat phase. The AAR is also impacted by surface mass balance, such that the ablation area can be enlarged through upward migration of the equilibrium line. In this case, the onset of catastrophic retreat can be attributed to a climate signal, if the preexisting geometry renders the glacier vulnerable.

Retreat becomes catastrophic once the terminus recedes beyond its protective shoals into the overdeepened depression behind. In deeper water, the calving rate increases correspondingly, and the backstress provided by grounding on the submarine moraine is removed. Where motion is mainly by basal sliding, removal of this resistive force leads to acceleration at the terminus, thinning, and mass drawdown. Thinning of the ice decreases the effective pressure at the bed, in turn leading to further acceleration, thinning and calving. Longitudinal extension also serves to encourage calving by opening new crevasses (Meier and Post, 1987). This positive feedback means that both velocity and calving rate can reach very high values. During catastrophic retreat at Columbia Glacier, for example, the velocity of the lower glacier increased by a factor of 3-4, from 3-8 m d^{-1} to 10-15 m d^{-1}. The seasonal amplitude of the velocity variation also increased once catastrophic retreat was initiated (Krimmel and Vaughn, 1987).

Retreat is halted when the terminus regains a position of stability, at a shallow or narrow point in the glacier fjord, and when the ablation area has been sufficiently reduced in size so that the mass imbalance tends towards the positive. Both conditions seem necessary; observations at Columbia Glacier and in Greenland have revealed that thinning and mass drawdown can continue even while the terminus position is held at a pinning point or valley constriction (Post et al., 2011). The initial instability causing the onset of retreat has been linked to thinning beyond a critical value by submarine melt, or other processes such as dynamic thinning caused by acceleration after the loss of back stress by the break-up of land-fast sea ice or floating ice tongues (Joughin et al., 2004; Pfeffer, 2007; Amundson and Truffer, 2010; Motyka et al., 2011)

Seasonal velocity variations of calving glaciers can originate at the terminus or from melt inputs further inland. It seems that whilst the interior of the Greenland Ice Sheet responds to a seasonal increase in sliding due to inputs of meltwater (Zwally et al., 2002), closer to the ice sheet margin, the onset of acceleration is due to processes acting at the terminus. The spring disintegration of a winter floating ice tongue or compact sea ice cover reduces the backstress on the glacier leading to acceleration and thinning. This acceleration propagates upglacier into the interior as the initial thinning reduces the effective pressure and steepens the interior surface gradient. At the end of the summer, the terminus begins to slow as melt ceases and the calving front advances. Interior velocity changes lag the terminus by some period of time, so that flux into the terminal area is still high, leading to thickening and further terminus slowdown. The reduction in surface gradient propagates the slowdown upglacier (Joughin et al., 2012). This same general pattern was observed at Columbia Glacier, with velocity at the terminus greatest in late fall when the glacier length was at a minimum, and backstress from the terminal moraine was also at a minimum, and velocity at a point 50 km above the terminus showing a maximum in mid spring and minimum in early fall, seemingly responding more strongly to melt input variations (Krimmel and Vaughn, 1987). At Hubbard Glacier, the seasonal variation in velocity is approximately 2 m d^{-1} (Trabant et al., 2003). Seasonal advances and retreats of the terminus position can be on the order of several hundred metres. The seasonal fluctuation in length is about 500 m, but this does not seem to be sufficient to destabilize the front (Ritchie et al., 2008).

The first efforts to model calving rate used empirically-derived relationships dependent on water depth at the terminus (Brown et al., 1982; Pelto and Warren, 1991). However, these relationships varied regionally and while high correlations were obtained with annual data, the relationship broke down at seasonal or shorter timescales when other factors became important, such as runoff in embayments (Sikonia, 1982). Additionally, the relationship does not hold for floating termini, and the physical basis for this relationship remained unknown. More recent models typically rely on the relation between glacier thickness, effective pressure and velocity (Van der Veen, 2002; Benn et al., 2007; Pfeffer, 2007; Amundson and Truffer, 2010). Efforts have been numerous based on the need to be able to understand and predict the dynamics of the outlet glaciers of Greenland, Antarctica and other large ice masses, given that these glaciers may be responsible for carrying most of the ice flux out of the ice sheets and mountain icefields. However, many of these models do not address reasons for thinning at the terminus, and so the link between climate forcing and dynamic response is unclear.

There is one theory addressing this gap that has lately attracted attention: ice-ocean interactions. Calving glaciers, especially those with floating tongues, are potentially more susceptible to climate warming because melt can be both subaerial and submarine. Whereas surface melt ceases in winter, submarine melting at the ice-ocean interface can continue all year. Recently, the importance of ocean temperatures and ocean circulation on calving rate has been given more attention, particularly the interaction between subglacial freshwater discharged at the grounding line and ocean water (Rignot et al., 2010, Motyka et al., 2011). Sikonia (1982) noted that summertime calving tended to be localized in embayments and that it increased with subglacial water discharge. It seems likely that these embayments form where subglacial channels exit the glacier front. The influx of cold, fresh, sediment-laden water drives convection currents that bring warm saline ocean water into contact with the glacier base (Rignot et al., 2010). Motyka et al. (2011) propose that submarine melting may explain the initial thinning that triggered the recent catastrophic retreat of Jakobshavn Isbrae, Greenland.

Studies of lake-terminating glaciers are rarer, although measurements that do exist suggest that the calving rate for lake-terminating glaciers is generally about an order of magnitude less than that of tidewater-terminating glaciers. This is perhaps due to lower buoyancy forces at the terminus for fresh water compared to seawater, due to generally shallower water and/or fewer effects from water circulation, including tidal effects. At Maud Glacier in New Zealand, for example, calving rate showed no correlation with ice velocity or water discharge variations, and an appreciable component of the ice face ablation was from melt (Kirkbride and Warren, 1997). Mendenhall Glacier in Alaska is currently experiencing significant retreat, and has had a calving face since ~1930 when its proglacial lake formed. The calving rate for 1999 and 2000 was ~ 130 m a^{-1}, although calving remained secondary to surface melt in terms of overall ablation (Motyka et al., 2003).

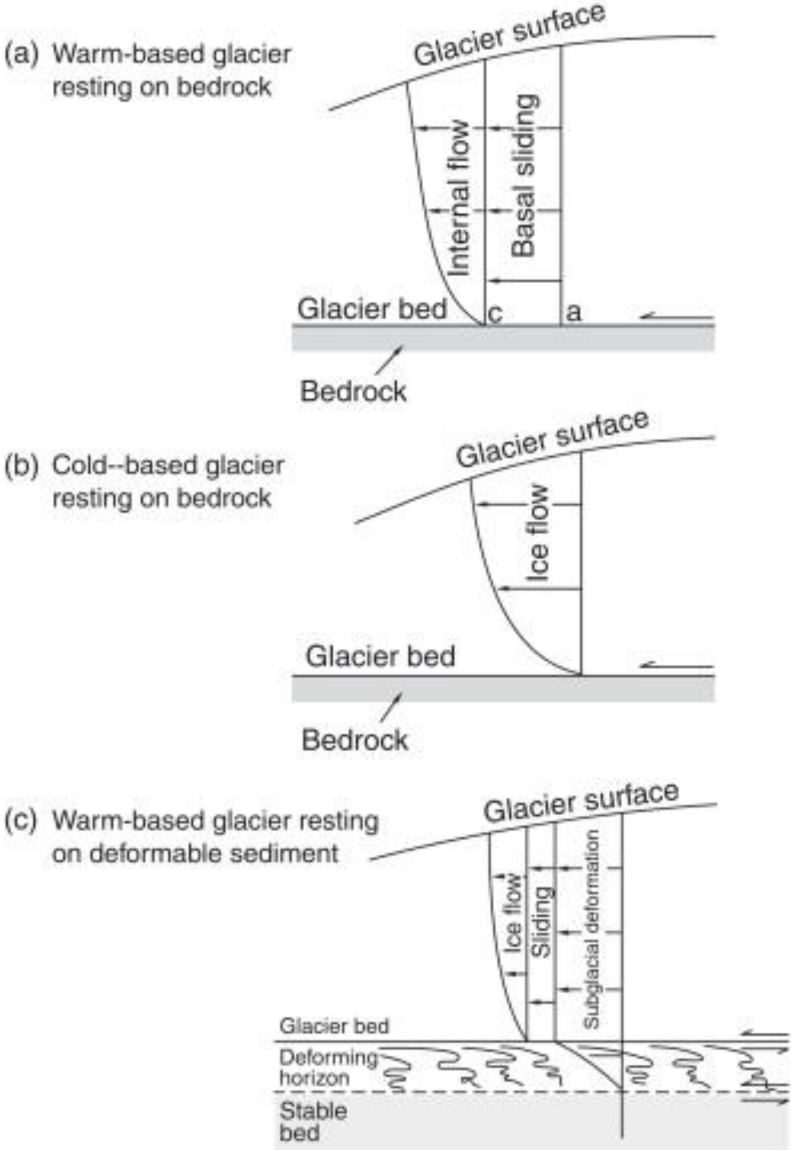

Figure 2.1: Schematic drawing of the types of glacier motion and under what conditions they occur. Internal deformation of ice (b) occurs under all conditions while the presence of water at the bed permits additional motion by basal sliding (a) and deformation of an underlying till layer if one is present (c). Reproduced from Siegert (2008).

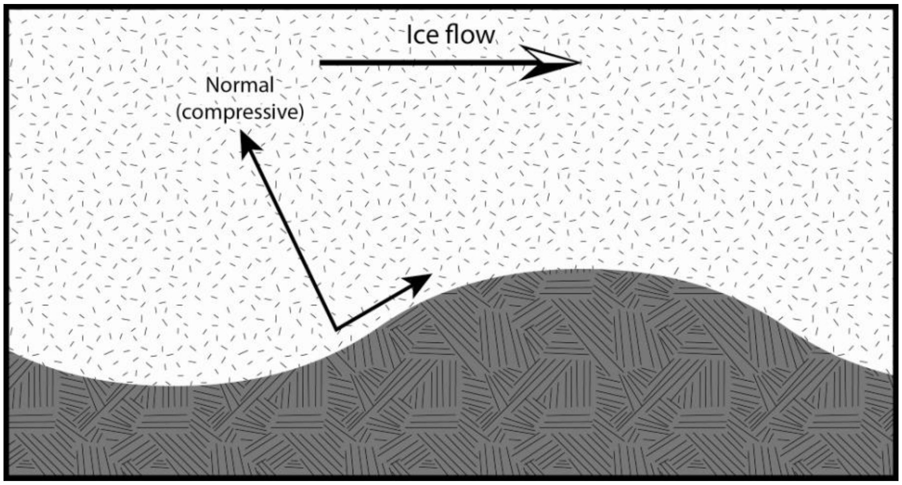

Figure 2.2: At undulations in the bed, a component of the normal force is oriented upglacier, providing an upglacier compressive force and increasing drag.

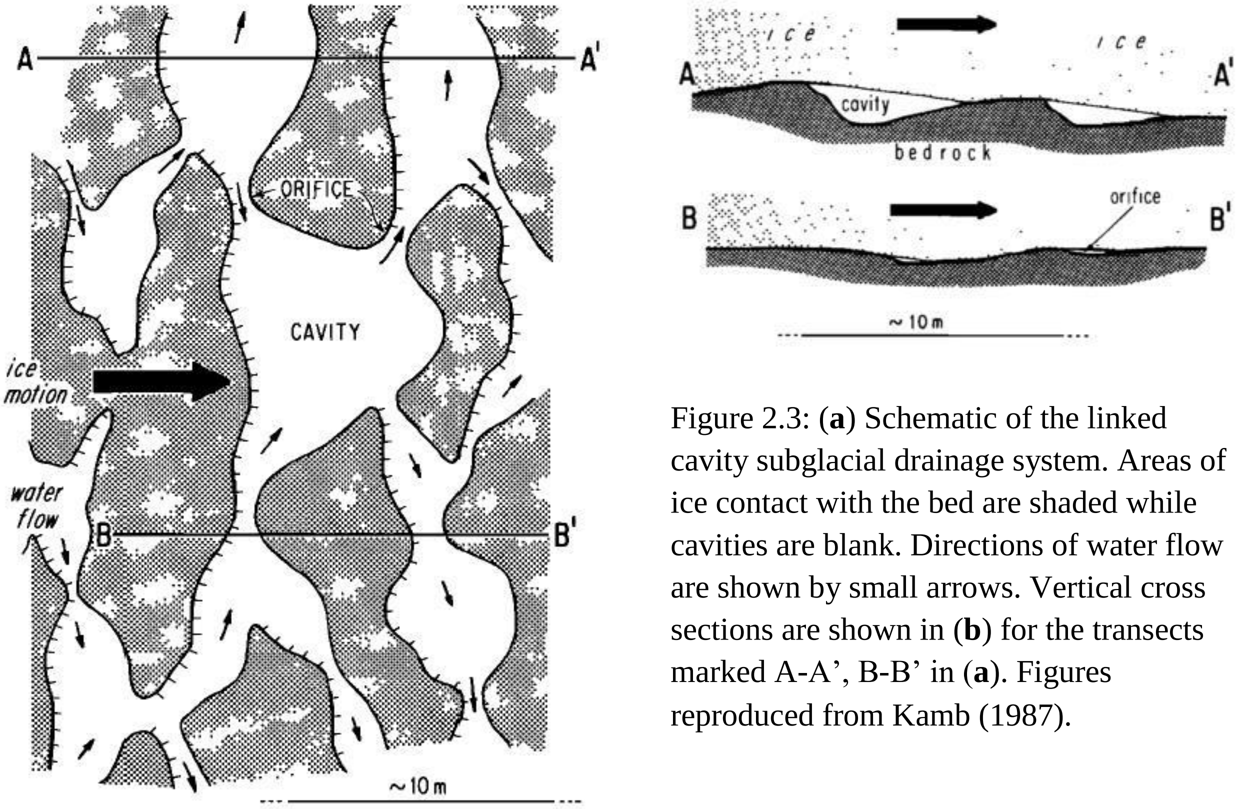

Figure 2.3: (**a**) Schematic of the linked cavity subglacial drainage system. Areas of ice contact with the bed are shaded while cavities are blank. Directions of water flow are shown by small arrows. Vertical cross sections are shown in (**b**) for the transects marked A-A’, B-B’ in (**a**). Figures reproduced from Kamb (1987).

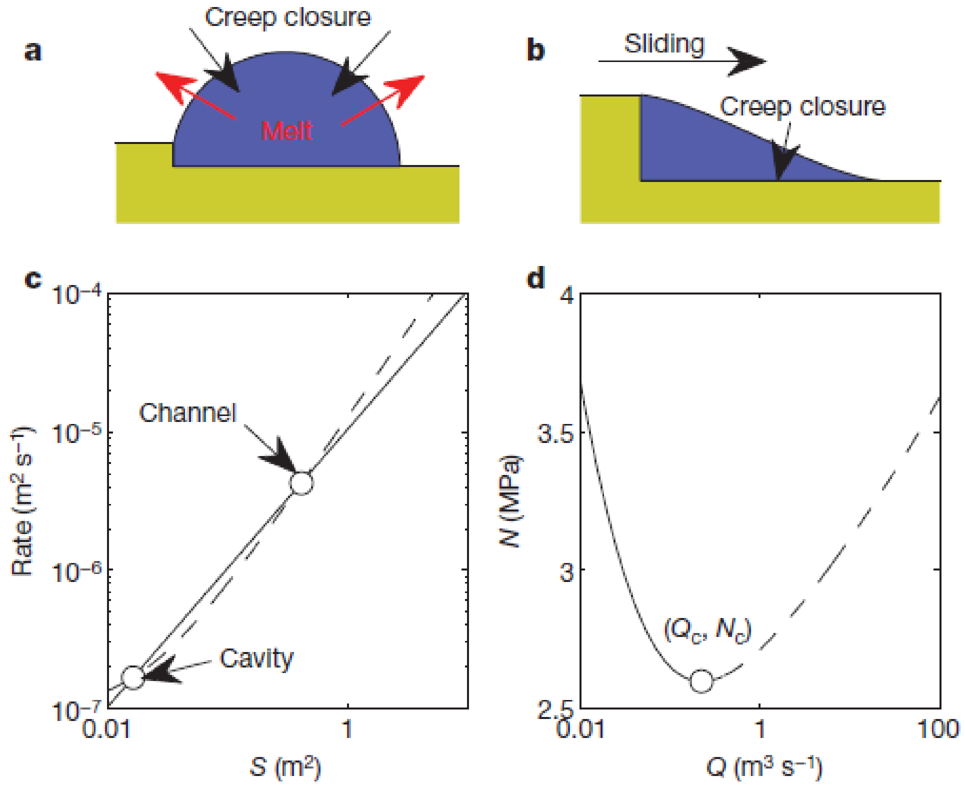

Figure 2.4: Schematic of the physics underlying the model of Schoof (2010). **a** and **b** schematize the cross-sectional area and processes defining the sizes of channels (a) and cavities (b). In **c**, the dashed line shows the conduit opening rate and the solid line shows the closure rate , plotted against S. The open circles represent states of equilibrium; channel and cavity. The cavity is stable, the channel is unstable in that if perturbed to slightly larger size, it will continue to grow (opening rate increases at a greater rate than the closure rate). **d** plots water flux by effective pressure. At large Q, the effective pressure increases with flux, at small Q, the effective pressure decreases with flux. A conduit will form a channel above a critical Q (dashed line), and remain a cavity below that threshold (solid line). (Reproduced from Schoof, 2010).

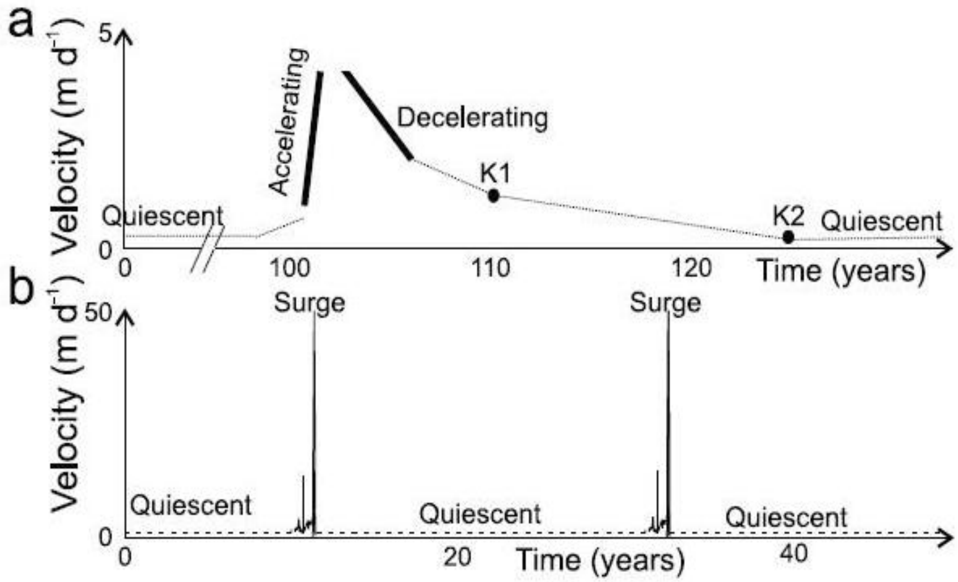

Figure 2.5: Schematic comparison of a typical Svalbard surge, based on Monacobreen and other Svalbard surging glaciers (**a**), and surges of the Alaskan-type Variegated Glacier (**b**). Svalbard surge data from Murray et al. (2003) and Melvold and Hagen (1998). Variegated surge data from Kamb et al. (1985). Figure reproduced from Murray et al. (2003).

Chapter 3: Methodology

This study primarily relies on the tracking of differences between pairs of satellite images to determine glacier motion. For a regional study, remote sensing observations offer significant advantages over more traditional field measurements, particularly in the St. Elias Mountains where access to field sites is often limited by their remoteness, high altitude, weather and logistics. As a result, existing field measurements from this region are very limited and may not be representative of regional glacier dynamics, nor provide information about the most significant contributors to regional ice fluxes or total mass loss. Remote sensing also permits measurements to be made across entire glacier surfaces, with fewer costs and at a finer resolution than would be possible with repeated surveying of gridded stake arrays.

3.1 Speckle Tracking of SAR imagery

The bulk of this project is formulated around speckle tracking of Radarsat-2 image pairs using an algorithm scripted in MATLAB by Dr. Laurence Gray (University of Ottawa; formerly Canada Centre for Remote Sensing). The technique has previously been used with good success in mapping ice flow patterns on Devon Ice Cap and Ellesmere and Axel Heiberg Islands in the Canadian High Arctic (Van Wychen et al., 2012; Short and Gray, 2005). Synthetic aperture radar (SAR) is particularly attractive for the monitoring of high latitude and altitude ice dynamics because of its ability to penetrate cloud cover and image during the night.

3.1.1 Data Acquisition

Radarsat-2 images were acquired from winter (January-April) 2011 and 2012. Acquisitions were limited to the winter season to have the greatest probability of maintaining image coherence during the 24-day interval between repeat Radarsat-2 orbits, given that summer melt changes the surface properties, altering the returned phase and making speckle tracking difficult. Within this restriction, acquisitions in each year were organized to image each location within the study area at least 3 times, to obtain at least 2 image pairs. Given the two years of data acquisition, this allowed for the possible analysis of 4-5 image pairs for most locations. Multiple pairs increase the probability of obtaining successful results over the whole region, and data from two years offers the possibility of observing interannual variations in flow velocities. Imagery was primarily obtained through Parks Canada (Jean Poitevin, Protected Areas Establishment and Conservation Directorate, Gatineau).

The 2011 imagery is in fine beam mode with a horizontal resolution of 8 m. In 2012, ultrafine wide beam mode imagery became available for order for the first time, and was acquired, given that initial processing of the 2011 data yielded promising results. It has a finer

(3 m) horizontal resolution, permitting analysis of ice motion patterns in greater detail. The extents of the Radarsat-2 fine-beam mode images range from 3000 to 3400 km^2. Coverage of the study area in 2011 was achieved with 12 image locations (47 individual scenes), covering a total area of 23 945 km^2. For ultrafine wide beam mode, the image extent ranged from 2200-3200 km^2. In 2012, 17 images (52 individual scenes) gave a coverage of 32 310 km^2 (Figures 3.1a, 3.1b). The area imaged in 2012 was slightly greater than in 2011, to capture the full extent of some glaciers that originate in Kluane National Park but terminate outside of it (e.g., Hubbard Glacier). All pairs were initially processed in MATLAB R2010b to determine the quality of results. All image locations were fully processed for one date pair in 2011 and one in 2012, with additional date pairs processed where there was improvement in the quality of results, or where there were features of interest (e.g. Hubbard Glacier). Details of the date pairs processed are found in table 3.1.

3.1.2 Speckle Tracking Process

Radarsat-2 is an active sensor, meaning that it emits its own energy and records the signal reflected back. The received signal is a result of the surface properties of the area being imaged, including reflectivity of the surface material, topography, water content and ice layers within the top layers of the snowpack. As described by Van Wychen (2010), single-look complex (SLC) SAR imagery contains information on the strength of the backscatter returned to the SAR sensor (its amplitude) and its phase (the position on the wavelength of the point at which the wave is reflected by the surface, essentially a function of the distance between the sensor and reflecting surface). These pieces of information are stored as a vector, with the amplitude expressed as the magnitude and the phase expressed as a direction in degrees.

The ground elements reflecting the transmitted wave are termed elementary scatterers or scattering centres. If the peaks and troughs of the waves reflected from the elementary scatterers within a pixel coincide, then constructive interference occurs, producing a stronger signal (a higher amplitude). Amplitude is also affected by the proportion of the transmitted wave that is reflected back to the sensor, influenced by the reflectivity of the surface. Phase returns have a much more random distribution, even in areas of bare snow where amplitudes are likely to be relatively constant. Because the snowpack is not completely opaque to the microwave energy emitted by a SAR sensor, the wave may be reflected at the surface, or may penetrate the top layers of a snowpack, until reflected by an elementary scatterer such as an ice lens. Therefore the point on the wavelength at which reflection occurs will be variable depending on the random distribution of elementary scatterers within the near-surface of the snowpack, producing the pattern of ‘radar speckle’ that is characteristic of raw SAR imagery (figure 3.2). Since this speckle pattern is a function of ground properties, it is unique to each location and will persist as a trackable return if surface conditions do not significantly change between image acquisitions due to factors such as melt, snowfall or snow redistribution by wind. Provided that coherence is maintained, the displacement of the speckle pattern between image pairs can be measured, converted to map units, and scaled to annual velocities.

The inputs to speckle tracking analysis are time-separated pairs of SLC SAR images. The two images (termed master and slave) must have the same geometry; thus, the repeat satellite orbit period is the primary factor that determines the frequency of image acquisition. For Radarsat-2, this is 24 days. Once acquired, the images are accurately co-registered and displacements are derived through a two-dimensional cross-correlation approach conceptually similar to that of feature tracking (and illustrated in figure 3.3). Image chips of predefined size are identified in the master image. Within the slave image, a search window is extended from the image chip centre, the size of which is set based on expected displacements. Correlations are calculated between the master image chip and congruent blocks of cells within the search window of the slave image. The peak in correlation coefficients corresponds to the best match between the two, from which displacement is then determined (Short and Gray, 2005; Van Wychen, 2010).

Smaller image chips give higher resolution to the final dataset, but are also associated with higher random errors, as there is a greater probability that the most highly-correlated match is not the true match. The ideal image chip size is large enough to produce a recognizable signal, but small enough that deformation and surface change within the image chip are minimized and small enough to retain as much resolution in the final results as possible (Huang and Li, 2011). Similarly, the size of the search window must be tailored to the image pair characteristics. It must be large enough to capture the magnitude of displacement of the glaciers in the image, but the larger the search window, the greater the probability of mismatches. Short and Gray (2005) determined that an image chip with sides of ~250-400 m (30-50 pixels) was most suitable for their study area in the Canadian High Arctic. In the very dynamic St. Elias Mountains, larger image chips were generally required in this study to constrain faster flows. The parameters used in the 2011 and 2012 processing are summarized in table 3.1. In general, areas with higher rates of flow required larger image chips to constrain. In areas of varied and complex flow, notably the images closest to the Pacific coast where single pairs may contain glaciers flowing at rates ranging from 10 m a^{-1} to 3600 m a^{-1}, pairs were run multiple times using different image chip and search window parameters, optimized for different glaciers in the image.

Displacements are expressed in terms of shifts in the azimuth (along-track) and range (across-track) directions, or as the one-dimensional components of the two-dimensional horizontal displacement. Range displacements can be affected by surface elevations. A digital elevation model (DEM) is therefore required to correct the slant range displacements (distance from the radar antenna to the ground target) to ground range displacements (the perpendicular distance from the ground track to the target; Figure 3.4) (Short and Gray, 2005; Van Wychen, 2010). For this project, version 2 of the ASTER Global Digital Elevation Model (GDEM) is used, with a horizontal resolution of about 30 m. It was obtained in one-degree tiles from NASA's Earth Observing System Data and Information System download portal Reverb (http://reverb.echo.nasa.gov).

The speckle tracking algorithm includes a calibration of the shifts to remove systematic biases due to any inaccuracies in the baseline or squint effects between the two SAR images (Short and Gray, 2005). An area of known zero displacement, usually an exposed bedrock outcrop, is manually defined, providing a stationary reference. Threedimensional displacements are calculated using the derived horizontal displacement and the change in elevation (extracted from the DEM) between the initial and final positions. Motion is assumed to occur parallel to the surface slope and in a straight line. Velocities are then calculated as the derived displacement divided by the time interval between image acquisitions (typically 24 days). This value is scaled to standard units of annual velocity (m a^{-1}). The process workflow is schematized in Gray et al. (2001).

The output from the speckle tracking algorithm is a velocity field containing information on the speed and direction of flow. Resolution of the grid is defined by the size of the image chip used. This dataset was imported into ArcGIS v.10 as a point layer and an inverse distance weighting (IDW) interpolation applied to produce a raster surface of flow rates. IDW provides a conservative approach to interpolation, as interpolated values cannot fall outside the range of values determined by the algorithm.

The speckle tracking algorithm has an inherent quality filter, requiring that the coefficient of correlation be ≥ 0.7; however, mismatches do occur and must be removed through a manual filtering process (Short and Gray, 2005). A mismatch occurs when a higher correlation is found with a different group of pixels than the true match. This can be due to coherence loss, where large areas may be unusable. Secondary causes include radar shadowing or other, more local, surface changes such as zones of significant thickening or shearing. Mismatched data points are removed from the dataset and from further analysis based on a number of criteria:

1. Flow vectors should show local agreement or coherence across a glacier surface; loss of surface coherence may be recognized by areas where vectors are oriented randomly, with no dominant flow direction and a similarly random distribution of flow magnitudes.
2. The flow direction or rate should not change abruptly over short distances and motion over bedrock surfaces should be at or close to zero.
3. Vectors should be oriented downslope and parallel to surface flow features such as medial moraines (with the exception of glaciers in the active phase of the surge cycle).

Image pairs composed of multiple runs with varying parameters were filtered and evaluated for errors separately and then combined in ArcMap into a composite image. A final raster surface was created from the filtered datasets, employing a fixed search radius for the IDW interpolation such that a surface is created only where data points remain in sufficient density. Cells with no data points within this radius (such as areas of coherence loss where data points have been filtered out) are excluded from the interpretation and are defined as no data cells within the raster. The 2011 velocity rasters have the following characteristics: cell size = 100 m, interpolation search radius = 500 m. The 2012 velocity rasters have a cell size of 50 m and the interpolation search radius is 250 m.

3.1.3 Advantages and limitations of the Speckle Tracking technique

In addition to speckle tracking, other remote-sensing methods commonly used to determine glacier motion include interferometry (or differential interferometric synthetic aperture radar, dInSAR), also using SAR data, and feature tracking, utilizing optical imagery (e.g. Kääb, 2005a, 2005b; Scherler et al., 2008; Luckman et al., 2002). Interferometry is the most accurate of these methods, with Strozzi et al. (2002) indicating that interferometry, under ideal conditions of coherence maintenance, can produce velocity estimates with errors 1-2 orders of magnitude less than those of offset-tracking techniques (of which speckle tracking is one), or accuracies up to the cm a^{-1} scale. However, several characteristics of interferometry make it unsuitable for a regional survey of glacier motion, most notably that it is limited to assessing displacements in the satellite look direction. Speckle tracking, in contrast, is capable of tracking displacements in two dimensions (Strozzi et al., 2002; Short and Gray, 2004). Interferometry is also heavily dependent on maintaining coherence across the glacier surface. The fast flow of some Yukon Glaciers combined with the relatively long 24-day orbital period of Radarsat-2 would lead to widespread decorrelation (Strozzi et al., 2002). In contrast, the point results produced by the speckle tracking algorithm are absolute and independent of each other, such that areas of low coherence do not negatively impact analysis in areas of high coherence (Short and Gray, 2004).

Speckle tracking also offers significant advantages over optical feature tracking in this region. One of the main limitations of feature tracking is that it is unable to measure displacements where there is a lack of observable surface features. The study area contains extensive accumulation basins of bare snow, where it would be difficult to obtain results by feature tracking (Scherler et al., 2008). However, because the phase returns in the SAR imagery are influenced by the random distribution of ice lenses or variations in liquid water content within the top layer of the snowpack, there is a trackable speckle pattern over bare snow.

Limitations of the speckle tracking procedure mostly concern resolution and accuracy. The technique can be less successful over small glaciers experiencing slow flow, although errors can be reduced through the use of high resolution SAR imagery. Short and Gray (2004) indicate that fine beam mode imagery, with a horizontal resolution of 8 m, is suitable for measuring ice velocities on glaciers with widths >~1.5 km. For smaller glaciers, the use of image chips composed of fewer pixels produces larger random errors, which may approach or exceed the motion of a small valley glacier over a 24-day period. However, the use of 3 m resolution ultra-fine beam mode Radarsat-2 imagery reduces the errors associated with smaller image chips, and produces a greater density of data points over small glaciers, thus decreasing the minimum detectable velocity. Loss of coherence still represents an obstacle to speckle tracking, although it is of generally less significance than for interferometry. Given that melt during the spring and summer months causes phase coherence to be lost, speckle tracking is most successful for winter imagery. Further errors may be introduced through ionospheric effects or azimuth streaking, although these effects are less pronounced at lower latitudes, and did not pose a problem during this analysis. There is also the possibility for the algorithm to begin tracking surface features such as crevasses if their signal overwhelms that of the radar backscatter, with an associated increase in errors (Short and Gray, 2005; Strozzi et al., 2008).

3.2 Error Analysis Methods

Errors in the speckle tracking method can arise because of co-registration errors, DEM errors, inconsistencies in the satellite orbital model, cross-correlation errors, and layover or foreshortening effects in the radar imagery (Gray et al., 2001). While gross mismatches may be removed during the filtering process, errors due to satellite geometry, signal noise or the DEM may not be. The bulk error of the speckle tracking method can be assessed by comparing derived velocity measurements with known velocity values.

Typically, this is done by evaluation of the apparent motion over zero-velocity bedrock outcrops (e.g., Van Wychen et al., 2012, Heid and Kääb, 2012b)

The error analysis as described in the coming paragraphs was in all cases performed on the velocity rasters created in ArcMap from the filtered points returned by the MATLAB script. A bulk measure of the errors associated with the regional-scale mosaicked velocity map was obtained through a summary of the apparent motion measured at bedrock outcrops and along ice divides in the 2011 and 2012 velocity mosaics. The process was also repeated for each individual image pair to provide more accurate errors for individual glaciers. The values derived from these individual image pair error evaluations are used in the next chapter when comparing velocity change over time at selected glaciers.

3.2.1. Evaluation of apparent motion over bedrock areas

The first error evaluation involves summarizing the apparent motion over bedrock areas where velocity should be zero. All areas within the aggregated image footprint outside of the Randolph Glacier Inventory (RGI) version 3.0 glacier extents were extracted. A buffer was applied to the glacier extents before extraction of the bedrock raster cells, because of greater errors along glacier margins that are not representative of the quality of results over glacier ice. Such errors arise due to interpolation over large velocity gradients, shadowing due to radar geometry in steep-sided valleys, or the presence of topographic features such as nunataks that are small relative to the size of the image chip used to derive the velocities and that therefore may not be ‘seen’ by the algorithm. The size of this buffer was determined based on the cell size and the interpolation distance used in the creation of the velocity rasters, and corresponds to two cells of the velocity raster. For the 2011 fine beam-mode imagery, this buffer was 200 m, for the 2012 ultra-fine wide beam-mode imagery, the buffer was 100 m. Thus, only bedrock areas >200 m (for 2011 fine) or >100 m (for 2012 ultra-fine) away from glacier ice were included in the analysis. This buffer removed most, although not all, edge effects. The bedrock area included in the analysis is shown for 2011 and 2012 in figures 4.1 and 4.2 in the next section. The bedrock area is shaded based on the magnitude of velocity.

It is expected that given the large influence of surface topography on the phase returns of a side-looking radar system, errors will be greater over steeper terrain (Scherler et al., 2008). Small inconsistencies in the satellite position or look direction can result in large apparent displacements over stable ground. These effects are likely not as significant over large glaciers where surface slopes are generally gentle, and therefore errors derived from steep bedrock outcrops may overestimate the error of velocity measurements on the major glaciers in the region. To investigate this, the apparent bedrock displacements were binned according to slope (derived from the ASTER DEM used in the speckle tracking). The DEM was smoothed to approximately the same resolution as the velocity raster.

3.2.2 Evaluation of apparent motion along ice divides

Apparent velocity values were also extracted along major ice divides, where motion is expected to be near zero. This is necessary to quantify errors for image pairs where bedrock outcrops (suitable for the error evaluation described above) may not be present, or may be extremely limited in extent. This occurred notably in the heavily-glaciated Pacific-facing side of the Mount Logan massif. These image pairs are also expected to have larger errors because of the lack of flat, stable ground to choose as a zero-motion reference point, necessary to calibrate the shifts as described in section 3.1.1 (Gray et al., 2001). For images where there is no area of ideal flat, stable ground, choosing different outcrops to calibrate the shifts would result in offsets of different magnitudes and directions. Experimenting with different calibration areas could minimize the offset, but rarely was it removed entirely. In the final dataset, this error would be visible in the vector directions, as a consistent offset in slow-moving areas where the percent contribution of the bias to the overall measured motion would be greatest. Extracting values along ice divides accounts for this bias.

Similar to Van Wychen et al. (2012), cell values were extracted every 10 m along all major ice divides as shown in figures 4.1 and 4.2 in the next section. Given that the RGI v3.0 outlines used to identify the divides are largely topographically-defined, with little consideration of ice dynamics, there may be some uncertainty as to whether or not the true ice divide was properly identified. At nine locations where neither the 2011 nor the 2012 velocity results agreed with the RGI v3.0 ice divide, its location was modified. The changes are summarized in table 3.2. In 7 of these cases, the modification was minor (between < 1 km^2 and 12 km^2). For the remaining two, entire upper tributaries were transferred from one glacier basin to another, in the first instance from the Hubbard Glacier to the Kaskawulsh Glacier (45.5 km^2), in the second, from the Hubbard Glacier to the Seward Glacier (59.8 km^2).

3.2.3 Comparison with dGPS measurements

The above methods provide an internal assessment of the performance of the speckle tracking method in the conditions and terrain found in the study area. Further validation of the results was derived from comparison with independent displacement measurements, notably in situ GPS measurements of stakes on the glacier surface. Differential GPS is able to provide highly accurate position data (~cm accuracy), through trilateration of signals from at least three satellites (Quincey et al., 2009; Berthier et al., 2005). Given the time between transmission and receipt of the satellite signal, as well as the known positions of the satellites, the position of the dGPS receiver can be precisely determined.

Dr. Luke Copland (University of Ottawa) manages a series of four dGPS stations on the Kaskawulsh Glacier within the study area; one at the equilibrium line, one in the upper ablation zone, one in the lower ablation zone, and one in the ablation area of a large tributary, the South Arm (Figure 3.5).The stations were installed by Samantha Darling and Dr. Luke Copland (University of Ottawa) in July 2009, and are composed of Trimble R7 GPS receivers mounted on poles drilled ~4 m into the ice for stability. They are powered by a 20 W solar panel linked to two internal 100 Ah 12 V batteries. Measurements are logged every 15 seconds, continuously in the summer and for three hours at noon during the winter months when little solar power is available. Processing of the data was performed by Emilie Herdes using the Natural Resources Canada Precise Point Positioning (PPP) technique (http://www.geod.nrcan.gc.ca/products-produits/ppp_e.php), which uses high accuracy orbital reconstruction and does not require a base station. Position accuracy using this method is <1 cm under ideal conditions, and generally increases with longer observation periods.

Extraction of the measured dGPS positions at the same time as the satellite image acquisitions provides a direct, ground-based comparison in which both the direction and magnitude of the speckle tracking results may be assessed. Straight-line displacements were then calculated in ArcMap over the 24-day interval corresponding to the satellite image acquisition period, giving an average velocity over the interval. Speckle tracking-derived velocities were then extracted at the same location from the velocity rasters and compared with the dGPS data for both orientation and magnitude.

In addition, Dr. Gwenn Flowers (Simon Fraser University) manages a network of 16 stations on a small glacier in the Kaskawulsh basin (informally, Glacier One: 60.8221°N, 139.133°W; GLIMS ID G220869E60822N). Camilo Rada of the University of British Columbia performed a similar comparison with the Glacier One dGPS points. In his comparison, dGPS velocities were linearly interpolated to the locations of those 2012 speckle tracking point results that were centrally located on the glacier surface, within the area defined by the GPS array; results are included here with his permission. Glacier One is a small, slow-flowing tributary, disconnected from the Kaskawulsh Glacier under current climate conditions, with average flow rates of ~ 25-50 m a^{-1}, an area of ~ 5 km^2 and a maximum width of ~ 1 km. It therefore represents a suitable test of the performance of the speckle tracking algorithm towards the lower limits of its capabilities.

3.3 Feature Tracking of Landsat imagery

To investigate whether glacier velocities have been undergoing any long-term evolution, feature tracking of archived Landsat-5 imagery since 1985 was undertaken. Table 3.2 indicates the image pairs used for the processing, and the general areas that were processed in each image. Landsat 1-4 imagery was unsuitable for analysis with the automated algorithm used, due to less well-constrained orbits and coarser image resolution (60 m) compared to Landsat-5 (30 m). Landsat-7 images were generally not used since the preferred time period was prior to its launch in 1999, and the 2003 failure of the scan line corrector produced imagery unsuitable for feature tracking. There was one Landsat-7 image pair processed (July 7, 2000 – August 11, 2001), selected because there were no suitable Landsat-5 pairs available for this period.

Summer images with limited cloud cover were preferentially selected, and matched with pairs that were as close as possible to one year apart. For fast flowing areas, an additional summer image was added to the annual pair, which allowed for the derivation of 16-day (1 repeat orbit) summer displacements. In all cases, an effort was made to be consistent in the time interval chosen. August or September images were preferred, where possible, due to their minimum annual snow extent. The main limitation in image selection was cloud cover, which is frequent in the St. Elias, particularly on Pacific-facing glaciers, and which significantly limited the availability of suitable pairs. Snow cover can also be a limiting factor when its extent changes considerably between images.

The feature tracking algorithm used in this analysis was a simple 2-dimensional cross-correlation algorithm developed by Dr. Andreas Kääb of the University of Oslo, Norway (Kääb and Vollmer, 2000; Heid and Kääb, 2012a). Similar to the process of the speckle tracking cross-correlation method, an image chip of predefined size (usually 11-21 pixels) is identified in the master image. A predefined search window in the slave image is then searched for the corresponding block of pixels and the target with the highest correlation is selected as the match, from which the displacement of the initial image chip is selected. The algorithm used subsamples of the initial imagery by a factor of four, which, given the Landsat 5 ground resolution of 30 m, allows for the derivation of X and Y displacements in intervals of 7.5 m.

Feature tracking was performed for several key glaciers. The Hubbard and Seward Glaciers were selected because of their large size and therefore importance for regional drainage. The Hubbard Glacier is also key to understanding long term changes as its trunk is not believed to surge, but many of its tributaries do appear to surge. There is therefore interest in better understanding how surging of upper tributaries may affect velocities at the terminus, and it is one of the few glaciers in the area that has previous ground-based stake measurements near the terminus that extend the velocity record back to 1978 (Krimmel and Sikonia, 1986).

The Kaskawulsh Glacier was investigated because it has a stable flow regime (i.e., not known to surge), meaning that any interannual changes are likely to reflect long term velocity evolution. The Logan Glacier was also selected as it appears also to follow a stable flow regime. Although a known surge-type glacier, the Lowell Glacier was selected because of the availability of previous velocity measurements from both the active and quiescent phases (collectively, 1973-1983; Holdsworth et al., 2002; Bevington and Copland, submitted 2013).The Donjek Glacier was also included in the feature tracking analysis in order to better assess its surge status, as there are no previous measurements of quiescent motion.

Landsat images were downloaded as georeferenced L1T products from the USGS Earth Explorer archive (www.earthexplorer.usgs.gov). Details of the image pairs used and the areas processed are given in Table 3.3. The algorithm was run on Band 4 imagery (nearinfrared; wavelength 0.75-0.9 µm), which generally provided the best contrast between features. Co-registration between images on the same path and row was tested for each image pair prior to running the feature tracking algorithm with single identifiable points over zero-motion areas (bedrock). If the algorithm showed no movement of the chosen stable points between the two images, then coregistration could be taken to be adequate. Given the 7.5 m minimum detectable motion of Landsat-5 images, any coregistration error less than this value will not affect the analysis. Storey and Choate (2004) estimate that the coregistration error of the Landsat-5 thermal mapping sensor is ± 6 m.

The Landsat feature tracking algorithm does not include any consideration of surface elevation, but assumes that motion occurs in 2 dimensions on a flat plane. At steep slopes this could introduce significant errors, but given that most large valley glaciers measured in this study have shallow slopes, the error due to this simplification is likely insignificant in relation to the 7.5 m minimum detectable motion or inter-seasonal variability in motion.

Filtering was undertaken on the algorithm results following the same guidelines employed in the speckle tracking filtering process. Given the coarser resolution of the Landsat-5 imagery compared to the Radarsat-2 fine and ultrafine imagery, the detail in the direction and magnitude of the derived displacements is poorer. Mismatches were generally more frequent than in the speckle tracking analysis because with relatively coarse resolution the distinctiveness of the image chip can be lost, especially where the glacier surface is composed of a series of similar-looking features (such as moraine cover or a crevasse field). Mismatches in particular were very common along flowlines, given that trackable features on a glacier surface are often created by the ice flow. Filtering was as a result stringent, such that only areas with high confidence results were retained for further analysis Confidence was greatest where the magnitude of displacement varied gradually across a continuous or near-continuous field of vectors oriented in the same direction spanning a significantly large area of the glacier surface. Patchy results were generally removed entirely.

To standardize the results, all displacements measured in this study were scaled to annual velocities by determining the motion per day over the time interval between image acquisitions and multiplying by 365 days. These velocities are not true annual velocities, but represent scaled velocities over periods varying from 16 days to 13 years, with most pairs representing average velocity over 350-400 days. Given that most glaciers flow more quickly in the summer than the winter, it is thus possible that a seasonal bias is present in the results for image pairs which were not exactly 365 days apart. This is mentioned in the results where it may be a significant factor and compared with the dGPS record to evaluate its influence.

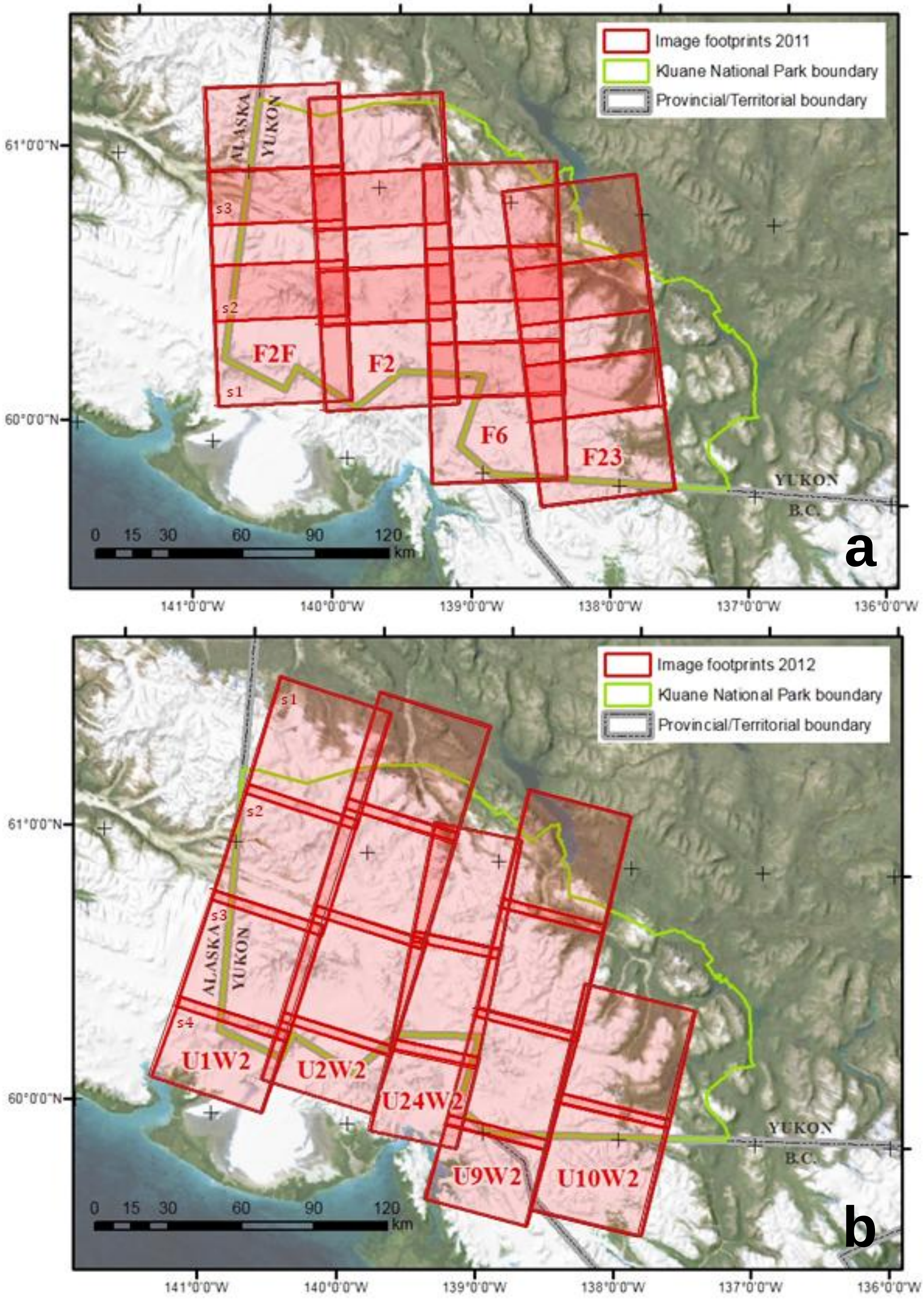

Figure 3.1: Footprints of the images acquired in (**a**) 2011, fine beam mode; and (**b**) 2012, ultrafine beam mode. Swaths are labeled by beam code, corresponding to table 2.1. With 2011 ascending data, segments are numbered south to north; descending 2012 segments are numbered north to south. Footprints are exported from the Radarsat Acquisition Planning Tool; provincial and Park boundaries are from the National Framework Canada Lands Administrative Boundaries Level 1, Geogratis; and background is a 500-m MODIS image obtained from Geomatics Yukon.

Year	Beam mode	Beam code	Near incidence angle (°)	Image Date pair	Segment	Image chip range (pixels)	Image chip azimuth (pixels)	Search window size (pixels)
2011	Fine	F6	46.9	Jan 03 - Jan 27	1 (composite*)	103, 201	125, 211	14, 23
					2	61	101	6
					3	103	125	6
				Feb 20 - Mar 16	1	61	101	8
					2	61	101	4
		F2F	40.0	Jan 10 - Feb 03	1 (composite)	103, 135	125, 163	6, 14
					2	113	145	8
					3	113	145	8
				Feb 27 - Mar 23	1 (composite)	103, 135	125, 163	6, 16
		F23F	30.8	Feb 14 - Mar 10	1	123	215	6
					2	93	163	6
					3	93	163	6
		F2	39.3	Jan 17 - Feb 10	1	111	151	14
					2	111	151	8
					3	91	131	8
2012	Ultra-Fine Wide	U1W2	28.6	Feb 17 - Mar 12	1	91	131	8
					2	91	131	8
					3	165	199	20
					4	199	249	40
		U2W2	29.5	Feb 24 - Mar 19	1	105	129	8
					2	105	129	16
					3	165	199	32
					4 (composite)	165, 201	191, 231	30, 70
				Mar 19 - Apr 12	2	105	129	16
					3	165	199	32
					4 (composite)	165, 201	191, 231	30, 70
		U9W2	35.4	Feb 21 - Mar 16	1	105	129	8
					2	165	199	20
					3	185	209	28
					4	299	319	30
		U10W2		Feb 28 - Mar 23	2	165	199	16
					3	199	219	20
		U24W2	46.0	Feb 18 - Mar 13	1	175	153	24
					2	251	235	24
					3 (composite)	251, 251, 251, 251, 301, 351	235, 235, 235, 235, 285, 331	24, 40, 70, 90, 110, 110
				Mar 13 - Apr 06	1	175	153	24
					2	251	235	24
					3 (composite)	251, 301, 351, 351	235, 285, 331, 331	24, 50, 70, 90

* composite images refer to scenes that were processed multiple times using parameters optimized for different parts of the image, as described in section 3.1.1 of the text. All parameters used are listed.

Table 3.1: Processing parameters of all fully-processed Radarsat-2 scenes. Beam codes correspond to the swath labels in Figure 2.1.

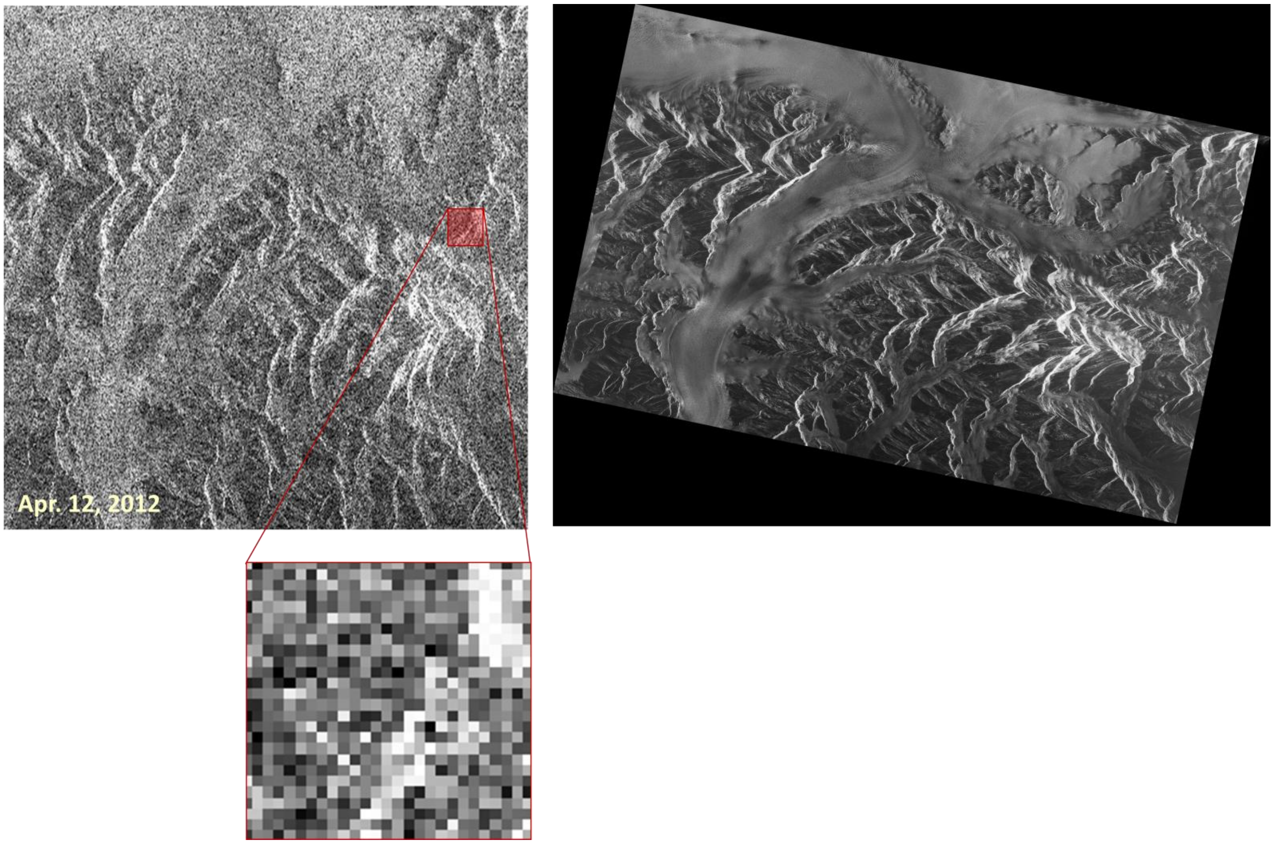

Figure 3.2: (Left) Radarsat-2 ultrafine wide-beam mode SLC image of the Lower Seward Glacier with inset showing the characteristic ‘speckle’ of SAR imagery. The pixel phase returns have a much more random appearance than the amplitude returns (on right) because they are more strongly affected by factors such as crystal and small-scale feature orientation, water content and subsurface reflectors.

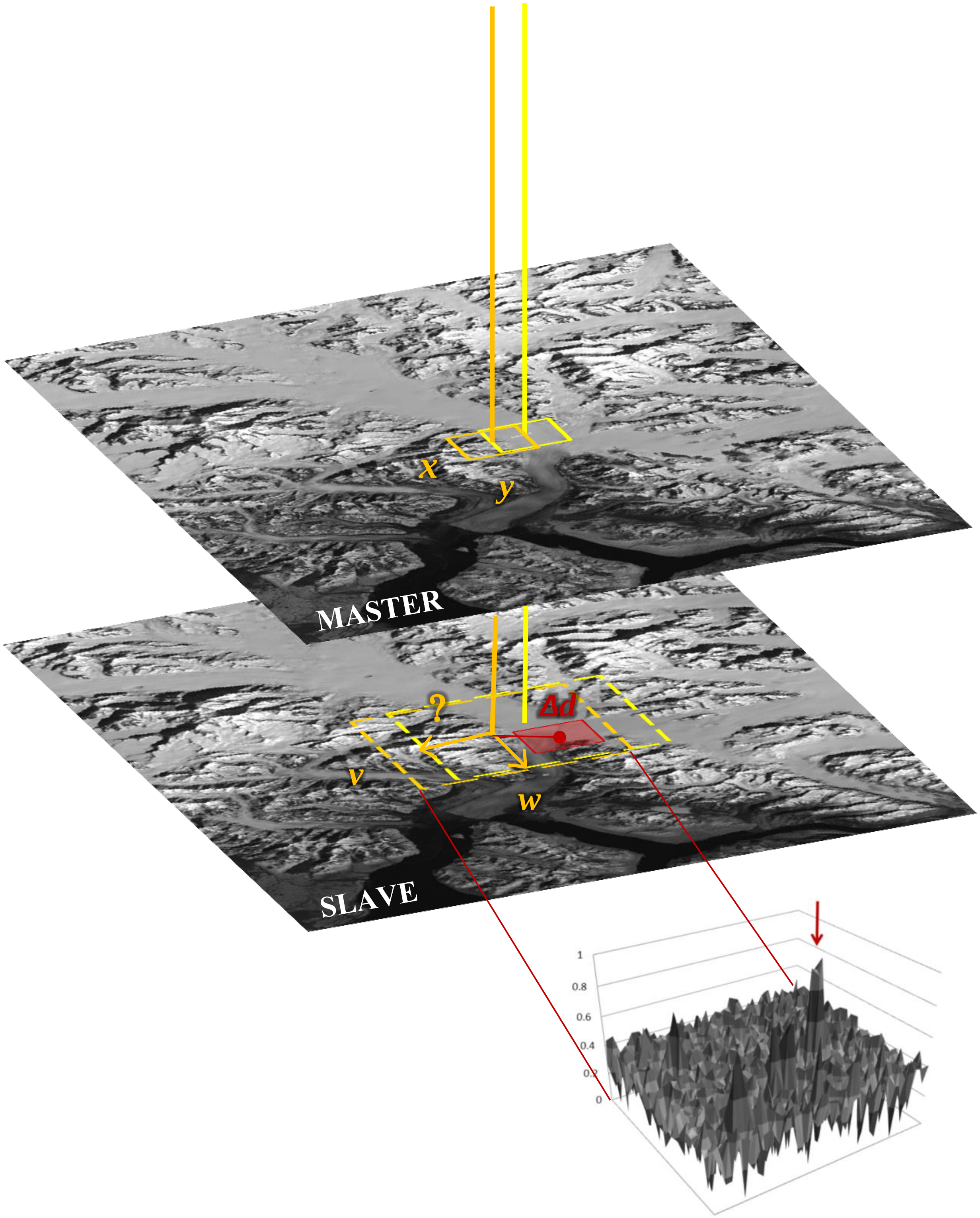

Figure 3.3: Schematic illustrating the concept of spatial cross-correlation, employed by both the speckle tracking and the feature tracking methods. An image chip of size *x* by *y* cells is identified in the master image. In the slave image, a search window of size *v* by *w* pixel shifts is extended outwards from the image chip centre. The displacement (*Δd*) between the initial image chip and the position of its most highly-correlated slave counterpart gives the motion over the image acquisition interval. The process is repeated across the image at a predefined step interval, usually about half the dimension of the image chip.

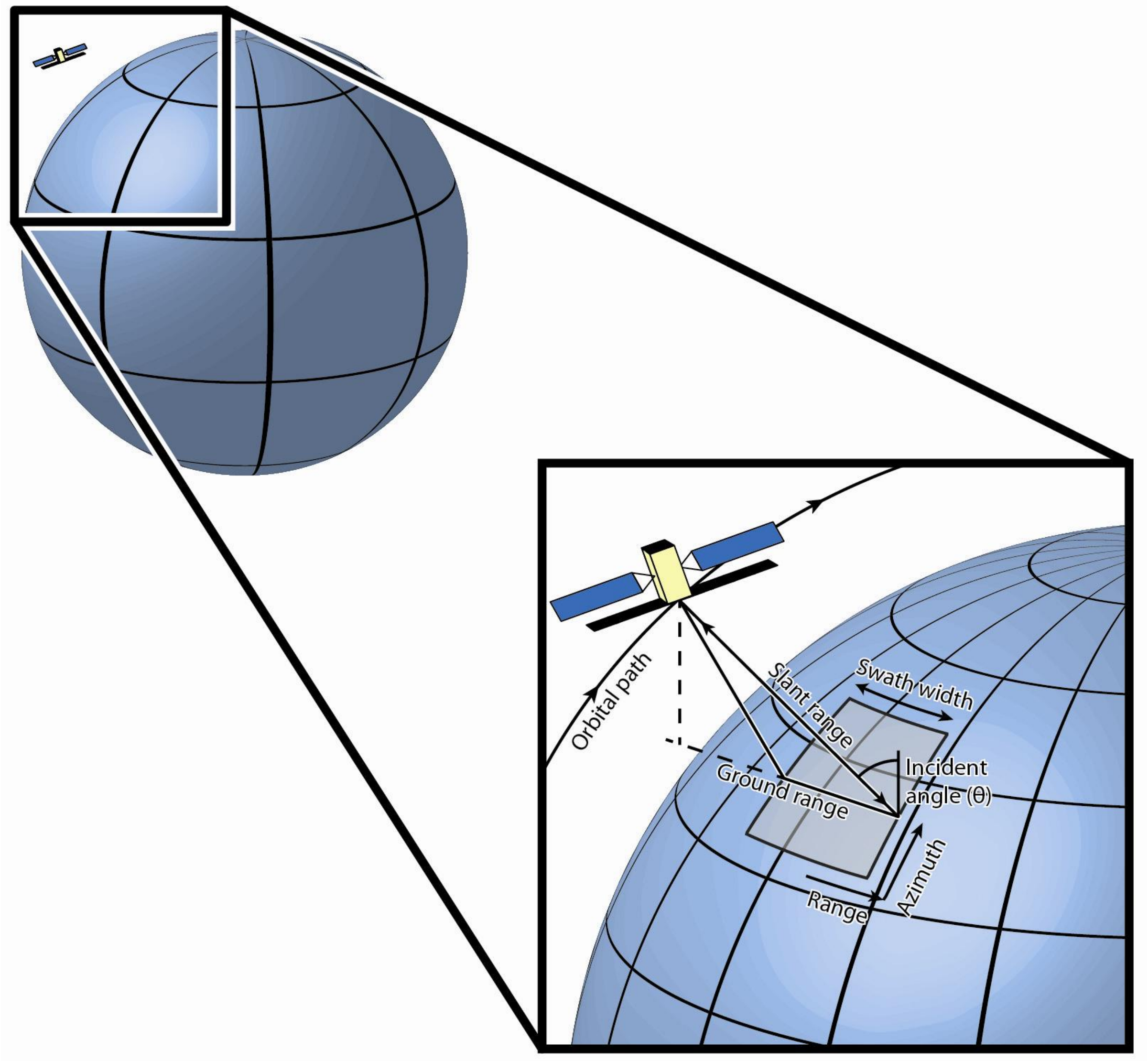

Figure 3.4: Schematic illustrating the viewing geometry of a side-looking radar system.

Location of change (UTM 7N)		**Glacier Basin**		**Area moved (km²)**
Easting (m)	*Northing (m)*	*from*	*to*	
553017.5	6752363.6	Donjek	Logan	4.9
554899.0	6742268.8	Logan	Hubbard	8.9
570452.0	6742600.8	Hubbard	Kaskawulsh	45.5
550451.1	6718565.7	Hubbard	Logan	1.0
617374.8	6705030.8	Kaskawulsh	Dusty	0.2
563870.9	6677742.2	Hubbard (Valerie)	Seward	59.8
559610.4	6674659.1	Hubbard (Valerie)	Turner	3.7
623774.7	6672759.5	Lowell	Hubbard	2.9
623997.9	6664442.4	Fisher	Hubbard	11.4

Table 3.2: Locations of changes to the GLIMS RGI v3.0 ice divides, based on 2011 and 2012 flow patterns.

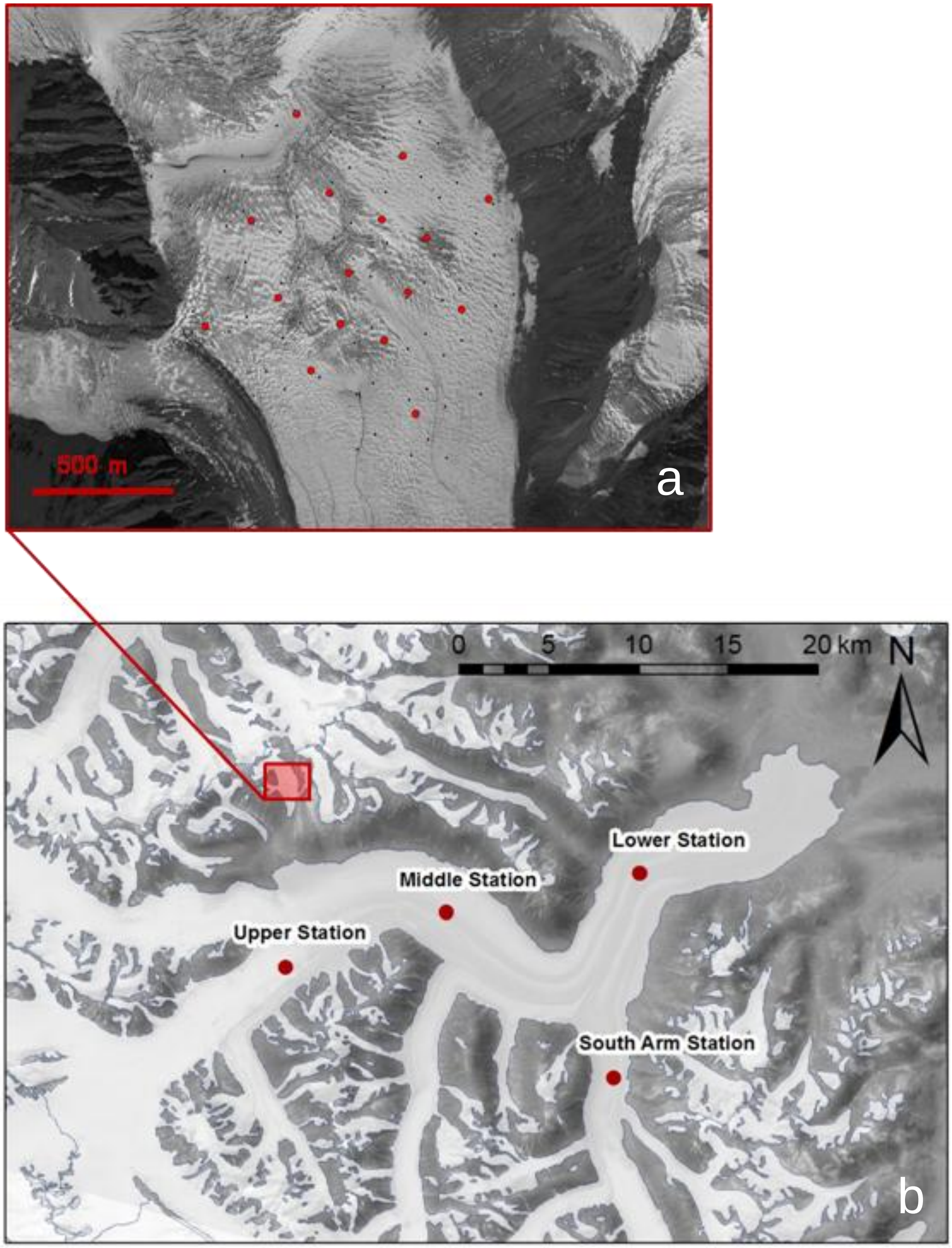

Figure 3.5: Positions of the dGPS receivers with which speckle tracking results are compared. (a): Glacier One stations managed by Dr. Gwenn Flowers (Simon Fraser University). (b) Kaskawulsh Glacier stations managed by Dr. Luke Copland (University

Landsat path/row identifier	**Image date pair**	**Interval (days)**	**Glacier area processed**
p061 r018	09/09/1988 - 09/25/1988	16	Hubbard Gl. terminus Mount Queen Mary tributaries (Hubbard Gl.)
	06/17/1998 - 07/03/1998	16	Hubbard Gl. terminus
	08/22/1987 - 09/09/1988	384	Mount Queen Mary tributaries (Hubbard Gl.), upper Hubbard Gl. Kaskawulsh Gl. Lowell Gl. Fisher Gl.
	06/30/1997 - 06/17/1998	352	Mount Queen Mary tributaries (Hubbard Gl.), upper Hubbard Gl. Kaskawulsh Gl. Lowell Gl.
p062 r018	09/11/1986 - 08/29/1987	352	Seward Gl. Mount Queen Mary tributaries (Hubbard Gl.), upper Hubbard Gl.
	07/07/2000 - 08/11/2001 *	400	Seward Gl. Mount Queen Mary tributaries (Hubbard Gl.), upper Hubbard Gl.
	09/11/1986 - 08/30/1999	4736	Logan Gl.
p062 r017	09/15/1996 - 09/24/1997	375	Donjek Gl.

* Landsat-7 ETM+ band 4 pair. Ground resolution remains 30 m. No suitable Landsat-5 pairs were available for the desired time period.

Table 3.3: Landsat date pairs used in the analysis of past velocities. All pairs are Landsat-5 images, unless otherwise indicated.

Chapter 4: Results

4.1 Error Analysis

4.1.1 Apparent motion over bedrock outcrops and ice divides

An assessment of the accuracy of the Radarsat-2 speckle tracking algorithm can be derived through the extraction of apparent velocities over known zero-displacement locations, namely bedrock outcrops and at ice divides. A summary of the mean apparent displacements at these locations is given in tables 4.1 and 4.2, broken down both by individual image pairs and for the mosaicked regional rasters as a whole. Per image pair, mean apparent velocities over bedrock outcrops range from 5.95 m a^{-1} to 55.70 m a^{-1} in 2011 (fine-beam mode), with an average of 16.58 m a^{-1}. The mean apparent displacement over the mosaicked raster as a whole is 11.58 m a^{-1}. The difference arises because the regional average is skewed to the lower-error northeastern tiles where there is much more exposed bedrock area than in the southwestern tiles that are dominated by snow-covered high mountain plateaus with isolated ridges and nunataks. Apparent motion along ice divides is greater, ranging from 19.01 to 44.82 m a^{-1} with an average of 24.89 m a^{-1}. The image pairs that have the greatest error associated with them are: F6 segment 1, F2 segment 1 and F2F segment 1. For all swaths, the highest errors are associated with the image tiles that are the furthest south, comprising the fast-flowing Pacific-facing glaciers. This gradient is also visible in Figure 4.1.

In 2012, where ultrafine-wide beam mode imagery was employed, the range of mean error per image pair is reduced to between 2.18 and 36.97 m a^{-1}, with an average value of 12.66 m a^{-1}, and a bulk regional error of 4.97 m a^{-1} from the mosaicked raster. Again, the apparent motion over ice divides is greater, ranging from 8.49 to 65.22 m a^{-1}, and averaging 17.98 m a^{-1}. For the regional mosaic, the error over ice divides is 16.94 m a^{-1}. The highest errors are associated with U1W2 segment 4, U2W2 segment 4, U9W2 segment 4 and U24W2 segment 3, corresponding to the Pacific-facing glaciers. Again, Figure 4.2 illustrates the error gradient across the region.

For the Landsat feature tracking analysis, bedrock velocities were extracted from the velocity rasters in the same way as for the speckle tracking analysis. In these cases the bedrock points from which the errors were derived were those immediately surrounding the glacier as each glacier was processed individually. Ice divides were not considered because in most cases, there were no ice divides in the area processed. The mean and maximum errors associated with each of the datasets are presented in Table 4.3, and range from 1.75 m a^{-1} at the Logan Glacier to 104.10 m a^{-1} at the terminus of the Hubbard Glacier. Errors are higher for shorter image acquisition intervals because the error in the displacement measurements, which is relatively consistent for each run of the program, is multiplied to annual velocities. The interval for the Logan Glacier was almost 13 years, so errors are very low. For pairs that were close to annual pairs, the error ranges from 4.93 m a^{-1} (Upper Hubbard Glacier 1987-88) to 20.44 m a^{-1} (Upper Hubbard Glacier, 2000-01) . Most fall between 7 m a^{-1} and 12 m a^{-1}.

The fast-flowing glaciers to the southwest of the study area are always associated with higher errors due to a number of reasons. Firstly, these image pairs are dominated by steep mountain peaks and ridges, meaning that areas of flat stable bedrock required to calibrate shifts during processing were extremely restricted. The lack of effective zero-motion calibration could introduce biases and offsets in the speckle tracking results. Secondly, the extremely fast flow in these areas means that the interpolation of glacier velocities across glacier margins follows a steep gradient, and high velocities ‘leak’ into adjoining bedrock cells. This was partially accounted for by employing a buffer of 100-200 m around the glacier extents, but this buffer was not made large enough to completely remove this effect because it was important to retain as many bedrock points as possible, especially in areas where bedrock outcrops are already limited in extent. Fast-flowing glaciers also require a larger search area to resolve large displacements during the image acquisition interval, which tends to increase the random error because the probability of random mismatches is higher.

There are also typically higher errors associated with steep terrain when it is imaged by a side-looking radar system. This effect was examined by binning all bedrock error points by the local slope (derived from the ASTER GDEMv2 used in the speckle tracking process, resampled to the same 50 m resolution as the velocity rasters). At best this is a rough estimate, because the resolution of the DEM is much poorer than the 3 m (ultrafine wide) or 8 m (fine) resolution of the Radarsat-2 imagery, and so the DEM is much smoother than the local topography seen by the SAR system. Figure 4.3 shows this relation and indicates that errors do increase with slope. However, it should be noted that the steepest bedrock slopes are likely to be found on the nunataks, peaks and ridges of the high-altitude regions, and so higher errors there cannot be directly attributed to the steepness of the terrain, but are likely influenced by the other error sources mentioned above.

Apparent velocity errors along ice divides arise because of inaccuracies in the positioning of ice divides, but also because there are generally higher errors in high altitude accumulation areas compared to low altitude expanses of stable bedrock. This may be due to general loss of coherence from factors such as change in the snowpack properties over the image interval, or due to calibration bias as discussed above. In general, the quality of results was poorer along ice divides, and there were few cases where the detail of the speckle tracking results would be good enough to identify the location of a flow divide within a few kilometres without the aid of topographic information.

For the following figures throughout the remainder of this chapter that show centreline velocities for selected glaciers, the error bars show the mean error of the individual image pair (for the 2011 and 2012 speckle tracking analysis) or of the individual dataset (for the Landsat feature tracking analysis) from which the centreline velocity was extracted. For cases where a centreline crosses an image boundary, there are two error bars shown, located on the profile as close as possible to the beginning of the respective image pair. For the fast-flowing Pacific-facing glaciers, or glaciers at high altitude, the error bars are relatively high due to their derivation from the ice divides. In most cases, however, the error is still relatively small relative to the magnitude of the velocity. For the glaciers flowing towards inland areas the errors are generally lower due to their derivation from large bedrock regions.

4.1.2 Comparison with synchronous dGPS velocities

The motion of in-situ GPS stations is accurate to the order of a few cm a^{-1}, as discussed in Chapter 2. They therefore provide excellent ground validation for the satellite image analysis, and provide the most accurate method for assessing the errors in speckle tracking. In 2011, speckle tracking-derived velocities at the positions of the Kaskawulsh dGPS stations were extracted for the periods Jan. 03-Jan. 27 (all stations), and Feb. 14-Mar. 10 (South Arm and Lower stations). For the interval Jan. 03-Jan. 27, 2011, the highest discrepancy between the two methods was found at the Upper Station. The dGPS measured motion of 136.81 m a^{-1}, and the speckle tracking analysis over the same interval measured a velocity of 131.84 m a^{-1}, an underestimation of 3.63%. At the Middle, South Arm and Lower stations, the speckle tracking results varied from the dGPS displacements by -0.32 m a^{-1} (-0.25%), -4.93 m a^{-1} (-3.44%) and +4.79 m a^{-1} (+4.61%), respectively. The absolute value of the mean error in the velocity magnitude over this time interval was 3.75 m a^{-1}. The mean error of the orientation of the velocity vector for the four sites during this time interval was 3.48°, ranging from 0.22° (Lower) to 8.75° (South Arm). During the interval Feb. 14-Mar. 10, 2011, the error in the magnitude of the velocity between the two methods was slightly greater. At the South Arm, the dGPS measured a velocity of 158.45 m a^{-1} and the speckle tracking results were 4.46% lower, at 151.38 m a^{-1}. At the lower station, the speckle tracking results overestimated velocity by 6.25 m a^{-1}, or 4.61%. The mean error in the velocity magnitude over this time interval was 6.66 m a^{-1}.

In 2012, velocities from the dGPS stations coincident with the Radarsat-2 image acquisition were obtained at the Upper, South Arm and Lower Stations. The Middle station data recording failed from August 2011 to May 2012. The maximum discrepancy was found at the Lower Station during the interval Feb. 21-Mar. 16, 2012, where the speckle tracking results overestimated velocity by 13.47 m a^{-1} (dGPS v = 158.68 m a^{-1}, speckle tracking v = 172.15 m a^{-1}), corresponding to a difference of +8.48%. At the Upper and South Arm stations, the difference in velocity between the two methods ranged from -1.19 m a^{-1} (-0.82%) to -5.46 m a^{-1} (-3.75%). The variation in the difference of the orientations was low, from 1.2° to 3.82°. The mean error in the velocity magnitude for all stations in 2012 was 5.79 m a^{-1}, and the mean error in direction was 2.46°.

These values are comparable to or less than the errors defined by the analysis of the apparent velocity of bedrock outcrops. The mean bedrock error of the Jan. 03-Jan.27, 2011 image pair overlying the four dGPS stations was 5.95 m a^{-1}, compared to the mean error between speckle tracking and dGPS displacements of 3.75 m a^{-1}. The mean bedrock error of the Feb. 14-Mar. 10, 2011 image pair was 10.44 m a^{-1}, compared with 6.66 m a^{-1} from the dGPS comparison. For 2012, the mean bedrock errors of the three image pairs were between 4.62 m a^{-1} and 5.70 m a^{-1}, compared to the range 1.19 m a^{-1} to 13.47 m a^{-1} and mean of 5.79 m a^{-1} obtained from the dGPS comparison. For the Kaskawulsh Glacier and other glaciers like it (landward-draining glaciers with intermediate flow rates), the comparison with the dGPS results suggests that the mean error over bedrock area is a more apt representation of the actual error over glacier ice than the mean error along ice divides. For these glaciers, the error given in the following centreline velocity figures corresponds to the mean apparent motion over bedrock.

At Glacier One, the error of all 2012 speckle tracking points was less than 15 m a^{-1}. For those points that were located close to the middle of the glacier (less than 30 m from the nearest GPS tower), the error is less than ~ 8 m a^{-1}. In the area of the dGPS units, the glacier velocity is between 20 m a^{-1} and 40 m a^{-1}, so the measured error corresponds to up to 40% of the flow rate of this glacier. Unsurprisingly, the error is slightly higher for this smaller, slower glacier, although the absolute value of the error is comparable to the error derived from the apparent motion over bedrock areas.

Overall, there is high confidence that speckle tracking and feature tracking provide a reliable and effective method to determine glacier velocities at the regional scale and at the scale of individual glaciers.

4.2 *Regional Flow Patterns*

The regional mosaicked velocity maps derived for 2011 and 2012 are shown in Figures 4.5 and 4.6, respectively. Of 23 945 km^2 of total area processed in 2011, 21 556.8 km^2 (90.0%) was retained after filtering. Of this, 14 208.1 km^2 of ice area was processed, and 11 048 km^2 (77.8%) ice area was retained after filtering. The largest areas of data loss (from coherence loss between the two acquisition dates) were in the upper accumulation areas of the Seward Glacier, the Donjek Glacier and the Kaskawulsh-Hubbard Divide. Significant area was lost in the Upper Seward Glacier near the divide with Bering Glacier and along the trunk of the Hubbard Glacier. It was also not possible to constrain the magnitude of flow through the fastest-flowing portion of the Hubbard throat.

In 2012, a total of 32 310 km^2 of ground area was processed. Speckle tracking was successful for 94.1% of this area; leading to velocity coverage over 15 102.9 km^2 of ice area or 87.8 % of the total 17 198. 3 km^2 of ice area processed. The area of coherence loss was much less in 2012 compared to 2011, although some of the same areas still proved problematic, such as the Upper Seward Glacier close to the divide with Bering Glacier, parts of the trunk of the Hubbard Glacier and relatively small parts of various other accumulation basins (including the Lowell, Kaskawulsh, Donjek, Turner Glacier basins). Some of these areas of data loss occurred where there were significant anomalies in the DEM.

Flow patterns conform to the known glacier drainage patterns, respecting catchment areas and ice divides, and showing patterns of branching tributary flow, both following visible topography and in the drainage of broad accumulation basins. The best example of this is in the broad accumulation area of the Upper Seward Glacier. Generally, higher velocities were found in the upper reaches of tributary glaciers, either as a result of steeper slopes near the headwalls, or the quiescent buildup of mass in surge-type glaciers, as will be discussed in more detail in the coming chapters. The velocities of the main glacier trunks tend to increase with distance down glacier to a mid-point before decreasing to the terminus in the case of land-terminating glaciers, or continuing to increase to a tidewater terminus. The main patterns are modified along the glacier length by variations in flow that are attributable in some cases to geometry. For example, there are localized high velocities at the icefall between the Upper Lowell/Dusty Glacier and the Lowell Glacier ablation zone. Elsewhere (as at the Kaskawulsh North Arm, Donjek Glacier trunk, and some tributaries of the upper Hubbard Glacier, for example), there are localized areas of high velocity at glacier bends or narrow points in the valley where thickening of the ice by longitudinal stresses would theoretically occur. These details of the qualitative pattern of flow provide further evidence that the speckle tracking analysis has accurately measured the regional velocity structure.

It has also revealed some surprising aspects of the flow pattern, such as accumulation basins that feed more than one terminus and unusual divagations in the patterns of flow that are not always associated with visible surface features (such as a ridge or nunatak) to explain them. The most significant basin that divides to feed two termini is the Upper Lowell/Dusty Glacier (Figure 4.7). The flux of this glacier divides above a prominent ice fall to feed the Dusty Glacier to the north and the Lowell Glacier to the south. Flow is greater into the Lowell Glacier; however, both glaciers surge, and it is possible that the changing geometry of the two glaciers during the stages of quiescence and activity influences how ice is divided between the two termini. Figure 4.8 shows a detail of the Kaskawulsh and upper East Arm of the Hubbard Glacier. In this area, there are two instances of the partitioning of glacier ice through two flow paths. The first shows ice from an eastern basin crossing an ice divide to feed both the Kaskawulsh and Hubbard Glaciers. Most of the ice is directed to the Hubbard Glacier, although the flow to the Kaskawulsh Glacier is significant. Immediately to the southwest is a smaller example, where ice is diverted around a peak. In the lower right corner, flow of the Hubbard Glacier is diverted around some obstacle that is not visible on the surface, delaying the true confluence between the West and East Arms of the Hubbard Glacier to further downglacier.

The analysis has revealed a strong gradient in the magnitude of flow. The highest velocities were measured on glaciers flowing southward from the major topographic divides formed by the Logan massif, both large glaciers such as the Seward and Hubbard Glaciers, but also glaciers draining a much smaller area such as the Agassiz and the Tyndall Glaciers. This pattern of high velocities is consistent with large-scale patterns of precipitation due to the winter advection of Pacific moisture towards the landmass combined with orographic uplift (e.g. Fleming et al., 2000). Glaciers draining landward display velocities an order of magnitude lower, in the range of 150-400 m a^{-1}.

4.3 Glacier Basin Breakdown

The following sections summarize the velocity results for the major glaciers in the region, broken down by drainage basin (Figure 4.9). The text focuses on the results of the 2011-2012 Radarsat-2 speckle tracking analysis, and also describes past velocities derived from feature tracking of archived Landsat images where applicable. For all figures unless otherwise indicated, the background image is a mosaic of Landsat-7 images from summer 2000 and 2001.The coordinate system is WGS 1984 UTM zone 7N.

4.3.1 Chitina River Drainage

The Chitina River drains westward from the Yukon-Alaska border, eventually flowing into the Gulf of Alaska. There are four main glaciers within the drainage basin, comprising two pairs of linked systems: the Anderson-Chitina and the Walsh-Logan (Figure 4.11). The termini of these glaciers are all extensively debris-covered and the boundaries between stagnant and active ice can be difficult to distinguish. Surges can also override or reactivate stagnant ice near the terminus. Walsh Glacier surged from 1960-61 to 1966 during which active ice flowed ~8 km into stagnant terminal ice (Post, 1966). The Anderson Glacier was observed in surge in 1968, and the Chitina Glacier likely surged concurrently based on observations in 1971 (Field, 1975). There is a region of ice-cored moraine at the juncture of the Anderson-Chitina valley with the Logan valley, which has been downwasting since before 1960 (Field, 1975). The 2011-2012 speckle tracking analysis shows that flow of the Walsh and the Chitina glaciers into their respective confluences is minimal, less than 10 m a^{-1}, with zones of stagnant ice of tens of km above the confluences. The Anderson Glacier is contributing ice to the joined valley while flow > 10 m a^{-1} was measured on the Logan Glacier at a point less than 10 km upstream of the confluence, and velocity was ~300 m a^{-1} at about 15 km above the confluence (Figures 4.5, 4.10).

Anderson Glacier

The 2011 and 2012 centreline velocity profiles of the Anderson Glacier match closely visually (Figure 4.12a), showing good coherence in the peaks at km 12, km 17 and km 25. From km 20 to km 32 there is evidence for 25-50 m a^{-1} higher velocities in 2012 than 2011, which is significant given the measurement error. This increase is not as high as the order of magnitude changes typically observed during surge events in this region (Bevington and Copland, submitted 2013; Post, 1966), although the surge observed in 1968 was of several years duration, and the year-to-year velocity variability during an active surge is not well known. The 2011-2012 velocity change is, however, consistent with measurements of year-to-year quiescent velocity evolution measured at Variegated Glacier (Raymond and Harrison, 1988).

Chitina Glacier

The Chitina Glacier underwent a significant increase in velocity from 2011 to 2012, shown in Figure 4.12b. The 2011 profile shows a velocity spike in the upper glacier between km 6 and km 14. In 2012 this zone of high velocity expanded up- and downglacier to between km 2 and km 20. The velocity increase is limited to the upper glacier, above km 20. Below km 36 the glacier appears to be inactive in both 2011 and 2012.

Logan Glacier

Based on Landsat image matching, there was very little motion of the lower 25 km (km 47 to km 72) of Logan Glacier between 1986 and 1999 (Figure 4.12c). The derivation of velocities over this region was assisted by the presence of several distinctive bends in the moraines of the lower glacier in some or all of a series of Landsat images from 1986, 1987, 1992, 1995 and 1999. Displacement of these features was visible on images separated by about three years or more, and was in no place greater than 50 m a^{-1}. The velocity results of 2011-2012 are much higher, up to almost 400 m a^{-1} at the lower glacier. This, combined with the profile of strongly increasing velocity to the terminus followed by an abrupt deceleration is indicative of unstable flow behaviour. Burgess et al. (2013), with winter measurements from 2007-2009, show a region of active glacier movement comparable in extent to that of this analysis, with peak velocities of ~220-250 m a^{-1}. This suggests that Logan Glacier experiences surges that build over several years. There is a significant increase from 2011 to 2012, from ~290 m a^{-1} to ~380 m a^{-1}, indicating that the surge is still ongoing. There has also been an advance of the active portion of the glacier by ~5 km, as evidenced by the downglacier progression of the velocity peak. This is the first conclusive evidence that the main trunk of Logan Glacier is surge-type.

4.3.2 White River Drainage

The White River captures flow from the Donjek River and then flows northward, ultimately draining into the Beaufort Sea. The main glaciers of this basin are the Klutlan, Steele, Spring, Donjek and Kluane Glaciers, all of which are known to be surge-type (Clarke and Holdsworth, 2002) (Figure 4.15). It also contains the Steele valley, which is home to a high concentration of surge-type glaciers which are unusually well studied for this region (e.g. Stanley, 1969; Collins, 1972; Clarke and Goodman, 1975; Clarke and Collins, 1983; Frappé and Clarke, 2007). The fastest flowing glacier of the White River drainage basin observed in this study is the Donjek Glacier, with a peak velocity approaching 400 m a^{-1} in 2011 and 2012. The Spring and Kluane Glaciers have 2012 peak velocities of 170 m a^{-1} and 218 m a^{-1}, respectively.

The largest glacier in this basin is Klutlan Glacier, which is characterized by a broad debris-covered terminal lobe. It largely falls outside of the study area, although the terminal 24 km, including two surge-type tributaries (Nesham and Mount Wood Glaciers; Driscoll, 1980), were included in the 2012 extent. In 2011 and 2012, Klutlan Glacier does not appear to be surging. Of its tributaries, there was a significant increase in velocity from 2011 to

2012 (>100 m a^{-1}, ~400%) on an upper tributary of Mount Wood Glacier. The neighbouring tributary shows a smaller but still significant decrease in velocity from 2011 to 2012 (Figure 4.13). Neither impacted the main trunk of Mount Wood Glacier within the two years examined.

Steele Valley

The Steele valley, containing the surge-type Steele and Hazard Glaciers, as well as four small surge-type glaciers (Hodgson, Trapridge, Rusty, Backe), also falls within this drainage basin. The four small glaciers all have low 2012 velocities that approach the measurement error. Indeed, it has been suggested that Rusty Glacier is probably unable to recharge its reservoir area after its last surge in ~1971, and that it is unlikely to surge again (Frappé and Clarke, 2007). There is less confidence in the 2011 results, where the coarser resolution of the fine beam imagery fails to constrain the pattern of motion on these small glaciers. For the Hazard Glacier, previous velocity measurements have been made there in both active and quiescent periods of the surge cycle. It experienced surges in ~1920, 1941 (major), sometime in the early 1960s, and another minor surge in 1981 (Clarke and Collins, 1984). In all cases, with the exception of the 1941 surge, velocity increases were limited to the upper portion of the glacier and the tongue remained inactive. Quiescent velocity from 1967-78 was 31 m a^{-1} in the upper glacier (Clarke and Collins, 1984). In 2011 and 2012 velocity in the same area exceeded 100 m a^{-1}. The area of high velocity also increased downglacier from 2011 to 2012, suggesting that Hazard Glacier is currently surging. The upper part of Steele Glacier approximately doubled in velocity (113 m a^{-1} to 221 m a^{-1}) from 2011 to 2012, while the lower glacier remained unaffected, and is flowing at <10 m a^{-1}.

Donjek Glacier

A detail of the velocity results of the Donjek Glacier is given in Figure 4.14. The centreline velocity profile of Donjek Glacier derived from the 2011 and 2012 Radarsat-2 speckle tracking, as well as 1996-97 Landsat feature tracking, is shown in Figure 4.17. The latter produced high quality results for the lowermost ~20 km of the 65 km long glacier. Velocities for the quiescent and active phases of the surge cycle are unknown for this glacier, although the 2011/2012 velocity is almost double that of the velocity measured in 1996-97. Observations by local pilots in summer 2013 (Andy Williams, pers. comm., Aug. 2013) indicate that the terminus of Donjek Glacier started advancing in spring 2013, and that the entire terminus region was much more heavily crevassed in summer 2013 than in preceding years. This suggests that the 2011/2012 results capture part of a new surge. Below km 53 there is a significant velocity increase from 2011 to 2012, which coincides with an abrupt velocity increase in the 1996-97 profile, and corresponds to the last bend in the glacier before the terminus. A tributary enters from the south at km 43, which shows a marked decrease in velocity from a peak of 390 m a^{-1} in 2011 to 93 m a^{-1} in 2012 at the same location (Figure 4.16a, b). The 2011 velocity of this tributary is much higher than for any other glacier of its size in the region, and it was oversteepened and freshly crevassed during overflights by Luke Copland in summer 2011. It is therefore possible that this 2011 tributary surge may be responsible for the observed Donjek terminus velocity increase between 2011 and 2012.

Spring Glacier

Spring Glacier has also been identified as a surge-type glacier from surface features such as looped moraines, although there are no measurements of its quiescent or active surge velocities. The centreline velocity profiles of 2011 and 2012 are shown in Figure 4.17. There is a marked increase in the velocity of the middle part of the glacier, before an abrupt decrease in velocity that corresponds to a sharp bend in the valley at km 17. Velocity downglacier of this point decreases gradually to values that are not appreciably different between 2011 and 2012. Spring Glacier may be commencing a surge in 2012, although it is also possible that the sharp bend in the glacier promotes the development of a reservoir area, and that the buildup of ice mass and velocity upglacier of the sharp bend in its valley is part of its quiescent evolution.

Kluane Glacier

Based on the presence of looped surface moraines, Kluane Glacier is believed to be surge-type (together with most of its tributaries), although none have previously been observed in the active phase of a surge (Clarke et al., 1986). The glacier shows no significant velocity change from 2011 to 2012, save in the upper reaches of some tributaries where there is evidence of small localized increases in velocity. These are generally consistent with quiescent phase velocity evolution.

4.3.3 Slims River Drainage

The Slims River drains the northern part of the Kaskawulsh Glacier terminus before flowing into Kluane Lake, while the Kaskawulsh River drains the southern part of the glacier terminus before eventually joining the Alsek River. The relative discharge through these rivers has varied over time, depending on water and sediment fluxes from the glacier as well as its terminus position (Fahnestock, 1969). The Kaskawulsh is a non-surge-type glacier that is fed by four large tributaries: the North Arm, Central Arm, Staircase Glacier and the South Arm. The fastest flow is measured on the North Arm, above the confluence with the Central Arm and near the long-term equilibrium line, peaking at 466 m a^{-1} in 2012. Along the trunk, the greatest velocities tend to occur at bends in the glacier. Both Staircase Glacier and the South Arm slow before joining the main Kaskawulsh flow. The glacier was the subject of a number of glaciological studies during the IRRP in the 1960s, and is significant for any assessment of long-term velocity evolution in the St. Elias Mountains because of its relatively stable flow. This study has derived velocities for the Kaskawulsh Glacier from Radarsat-2 speckle tracking (2012 and 2011) and from Landsat feature tracking (Aug. 22, 1987 - Sept. 9, 1988 and June 30, 1997 - June 17, 1998), and compares these with stake measurements made during the IRRP studies of the 1960s (Clarke, 1969: Kaskawulsh-Hubbard Divide; Anderton, 1970: North Arm-Central Arm confluence).

Feature tracking in 1987-88 and 1997-98 was only successful in limited areas, so a centreline profile could not be reliably produced. Instead, cross profiles were positioned at points along the glacier length where there was the highest confidence in the results of both date periods; i.e. where data points were continuous across the glacier surface after filtering, so that interpolation was minimal. This resulted in cross profiles at the mouth of the North (Figure 4.18, A-A'; 1987-88, 2011, 2012) and Central Arms (B-B'; 1987-88, 1997-98, 2011, 2012), where the ice from the accumulation basin begins to be constrained by the valley walls. A third profile was positioned downglacier of the South Arm confluence (C-C'; 1997-98, 2011, 2012) and a fourth profile just before the terminus (D-D'; 1987-88, 1997-98, 2011, 2012).

The North Arm (A-A') profile shows excellent agreement between the three date periods, with no significant differences. Peak velocity varies between 210 and 215 m a^{-1}. The South Arm profile (B-B') shows some small variability between the different measurement periods on the southern margin (towards B') for the years 1987-88, 1997-98, and 2012 while the northern margin shows no change. The profile for the year 2011 shows much higher velocities near the endpoints of the profile compared to the other years, and appears to show a widening of the area of active ice flowing out of the accumulation basin, although it is not accompanied by an increase in the peak velocity, which remains in the region of 107-139 m a^{-1}. At the third profile (C-C'), there is an increase in velocity from 2011 to 2012 that is significant given the measurement error, but is only ~20 % of the 2011 velocity, far less than the variability observed at other glaciers in the study area. The 1997-98 profile is similar to the 2011 profile. The anomalously low values at 3000 m from the northern margin coincide with a gap in the data points, and are probably not significant.

Of the four Kaskawulsh profiles, the terminus profile D-D' shows the greatest variability between measurement periods. Change from 2011 to 2012 is largely insignificant (peak velocity 80-90 m a^{-1}), but both 2011-2012 profiles are considerably less than the 1987-88 profile (peak velocity 181 m a^{-1}). The 1997-98 profile does not conform to a pattern of decreasing velocity with time, as its values are significantly lower than the velocities measured in 2011 and 2012. There is a possibility that the lower values measured are reflective of seasonal variation; this will be examined in the next chapter.

Comparisons with 1960s ground-based velocity measurements

During the IRRP a profile was run across the Kaskawulsh-Hubbard Glacier Divide, at which radio-echo thickness soundings and velocity measurements were made (Clarke, 1969). The velocities were determined between the summers of 1962 and 1963, to give annual measurements (Figure 4.19b). On the Kaskawulsh side of the Divide, velocities show little change over the 50-year period. On the Hubbard side, 2011 and 2012 velocities are significantly lower than in the 1960s. In 2012, there is a reduction of 50%, while in 2011 the trend is comparable, although errors are larger.

Also as part of the IRRP, stake velocity measurements were obtained at the confluence of the North and Central Arms of the Kaskawulsh Glacier (Anderton, 1970). These stakes were arranged in three lines roughly 1 km apart, transverse to glacier flow, above the confluence (E-E'), at the confluence (F-F') and below the confluence (G-G') as shown in Figure 4.20a. Displacements were measured during the 1964 and 1965 field seasons, yielding annual velocities. 2011 and 2012 velocities were extracted at 50 m intervals along profiles constructed connecting these stakes. The results are plotted in Figure 4.20b. At all three profiles, there is a significant decrease in velocity from 1964-65 to the present. The North Arm decreases in velocity by up to 187 m a^{-1}, or ~50% (profile F-F'), while the velocity reduction of the Central Arm is less at 94 m a^{-1}, or 38% (profile F-F'). As a result, the velocity difference between the North and Central Arms is less in 2011/2012 than it was in 1964-65. The motion was also generally higher in 2012 than 2011 in all three profiles, although the difference was much less in comparison to the 1960s. The magnitude and significance of long-term vs. seasonal velocity changes along these profiles will be discussed more thoroughly in the next chapter.

4.3.4 Alsek River Drainage

There are four large valley glaciers in the study area which belong to the Alsek watershed: moving southwards, the Dusty and Lowell Glaciers, the Fisher Glacier, and the Tweedsmuir Glacier. The smaller Felsite and Disappointment Glaciers lie to the north of the Dusty Glacier. All of these are surge-type, although not much is known about the periodicity, duration or velocities of surges of the Dusty and Fisher Glaciers. The last known surge of the former was in 1966, and the Fisher Glacier last surged in ~1970 (Clarke and Holdsworth, 2002). The Disappointment and Felsite Glaciers have never been described in their active phase, although they contain extensive looped surface moraines indicative of past surge activity.

Tweedsmuir Glacier

The Tweedsmuir Glacier has been observed through several surges, and velocities have previously been measured through manual feature tracking (Holdsworth et al., 2002). It is currently in quiescence following a surge that terminated in 2009, and has a peak 2012 velocity of only 39 m a^{-1} (low for a glacier of this size), Along its longitudinal axis the velocity increases gradually to a point near the middle of its length and then decreases gradually, producing a very symmetrical longitudinal profile. However, the upper reaches of several tributaries are flowing unusually rapidly for their size. The velocity structure of this glacier and its tributaries is very similar in winter 2012 to that measured by Burgess et al. (2013) in winter 2010.

Lowell Glacier

Two centrelines were constructed on the Lowell Glacier; the first (Lowell) runs from the head of the accumulation area shared with Dusty Glacier to the terminus, and the second (South Lowell) runs from the head of the southern accumulation basin to the confluence with the northern arm (at about km 48 of the Lowell centreline), as shown in Figure 4.21. Velocities extracted along these centrelines are shown in Figure 4.22a and b. The velocity spike in the Lowell centreline at km 42 corresponds to a steep icefall which divides the Dusty and Lowell valleys. The Lowell Glacier surged between July 2009 and June 2010 (Bevington and Copland, submitted 2013), so velocities measured in winter 2011 and 2012 represent the evolution of the glacier during its return to quiescence. In surge, the Lowell Glacier advances past a nunatak near its terminus. Since the end of the surge, the terminus position seems to have stabilized at the nunatak.

From 2011 to 2012 there is an appreciable decrease in velocity of the northern arm above the ice fall, the southern arm above the confluence, and the ablation area of the glacier below the icefall and confluence. The velocity decrease of the northern arm was relatively small (-~75 m a^{-1}) compared to the southern arm (-~200 m a^{-1}) and nearer to the terminus (-~100 m a^{-1}). In comparison with 1987-88 velocities measured from feature tracking, which showed near stagnation over the lowest ~25 km of the glacier during a quiescent stage of the surge cycle, the glacier is expected to further decelerate This is consistent with results of Bevington and Copland (submitted 2013) who measured a progressive decrease in the forward displacement of the position of the calving front over the quiescent period.

4.3.5 Disenchantment Bay Drainage

Drainage of glaciers into Disenchantment Bay reflects by far the largest ice fluxes in the study region. The Hubbard Glacier alone is ~123 km long, with an area of 3321 km^2, flowing from the highest peaks in the region to a tidewater terminus in the mouth of Disenchantment Bay. The largest of its named tributaries is the Valerie Glacier, entering from the west near the terminus. About 20% of the length of the calving face of the Hubbard is composed of ice from the Valerie. The Valerie Glacier is known to surge, and its velocity variability during quiescence appears to be high, although measurements are lacking (Ritchie, 2008). The dynamics of the terminus of Hubbard Glacier have received significant attention over the past 40 years (Brown et al., 1982; Krimmel and Sikonia, 1986; Mayo, 1989; Trabant et al., 1991; Krimmel and Trabant, 1992; Trabant et al., 2003; Motyka and Truffer, 2007), although the velocity of the upper glacier and its variations has been little studied. This study has derived velocities along the glacier length in 2011 and 2012 from speckle tracking, terminus velocities from September 1988 and June-July 1998 from feature tracking, and velocities in the upper glacier from feature tracking in 1986-87, 1987-88, 1997-98 and 2000-01. The 2012 speckle tracking results indicate previously undescribed surge activity in a tributary branch of the upper Hubbard Glacier flanking Mount Queen Mary.

There are two other tidewater glaciers within the study area that drain into Disenchantment Bay to the west of Hubbard Glacier: the Turner and Haenke Glaciers (Figure 4.23). Neither of these has been as extensively studied as the Hubbard Glacier, and both are much smaller, although their histories from 1890 to 1970 have been in some measure reconstructed from sporadic photographic records (summarized in Field, 1975). The Haenke Glacier appears to be a surge-type glacier that advances to tidewater and then thins and stagnates with some retreat; calving appears to account for much less of the ablation than for other tidewater glaciers. The 2012 Radarsat-2 amplitude images show that the glacier extends into the bay, but its terminal lobe is overridden by that of the adjacent Turner Glacier. The 2012 velocity results indicate that the glacier is currently quiescent, with most of its terminus appearing to be in state of stagnation.

In 2012, the terminus of Turner Glacier extends well out into Disenchantment Bay with an obviously active calving face. Velocities are highest in the upper glacier, peaking at ~1339 m a^{-1}, before decreasing at the mid glacier to values of ~64 m a^{-1}. Velocities then increase slightly to the terminus, also consistent with an active calving face. Turner Glacier advanced from 1899 to 1958 when an earthquake may have led to the destabilization of the deltaic sediments underlying the terminus, resulting in a 700 m recession. The glacier recovered, advancing slightly by 1965 before undergoing another recession in 1968. Its current extended position has been stable since at least 1987.

Upper Hubbard Glacier

The only record of surge activity in the upper Hubbard Glacier is found in Clarke and Holdsworth (2002) who note that a surge was observed in 1981 "in one of the glaciers on the side of Mount Queen Mary", and that this surge was strong enough to move into the main trunk of the Hubbard Glacier. Glaciers flowing from the slopes of Mount Queen Mary all feed the Hubbard Glacier so there is some ambiguity as to which tributary system is referred to, especially since this study has provided evidence for surge activity in two of these systems (Figure 4.24a). The three tributaries of the western branch were observed to be concurrently surging in 2009. Flights over the area in April and June 2009 indicated new extensive crevassing on all three tributaries, with crevasses extending into the upper Hubbard Glacier (Figure 4.24b). The speckle tracking analysis revealed a significant slowdown of these glaciers, from an average of 256 m a^{-1} and maximum of 330 m a^{-1}, to 2012 velocities of ~100 m a^{-1} in 2012 (Figure 4.25c and d).

At the southern tributary branch, the 2012 speckle tracking analysis identified anomalously high velocities in the upper reaches of one tributary. As a result, there was interest in deriving past velocities in this area from feature tracking. Five Landsat image pairs were processed, and those that provided high quality results are shown in Figure 4.25. The constituent tributaries of the branch are drawn in the first image, and the numbering is as referred to in the text. Feature tracking confirmed that this tributary branch is indeed surge-type. The three image pairs from 1986-88 capture the evolution of a surge that activated the entire tributary branch. Motion from 1986-87 is relatively small (maximum speed is 84 m a^{-1} on the main branch upglacier of the confluence with the Hubbard East Arm), although greater than the inactivity measured over most of the area in 2012. There are higher velocities (~ 153 m a^{-1}) building in 'tributary 2' in the upper reaches of the branch. The next year (1987-88) shows an increase in velocity of the main trunk of the tributary to 265 m a^{-1}, or 215%, and a downglacier propagation of the location of peak velocity. The velocity increase is greater at 'tributary 2', where it peaks at 398 m a^{-1}. 'Tributary 5' entering from the west is still flowing slowly. The next image pair (September 1988) captures motion over the 16 days immediately following the previous pair. Velocities are very high, from 100-1000 times those measured in 1986, and all tributaries are active, including 'tributary 5' that experienced very little flow in the year previous.

The 1997-98 image pair did not produce good coverage over the area, although visual inspection of the images shows little change in the position of surface features. It can thus be concluded that this branch of the Hubbard Glacier was quiescent in 1997-98. The next image pair for which there are high quality results is the annual pair 2000-01. The state of the glacier at this time is similar to that of 1986-87, with intermediate velocities on the main branch of the tributary, peak velocities in the upper reaches and significant inputs from the southernmost ‘tributary 4’. By winter 2012, the majority of the branch is inactive, although the upper pair of tributaries (1 and 2) both show increased activity in their upper reaches. Whereas the 1987-88 surge seems to have been initiated at ‘tributary 2’, the March 2012 pair shows extremely high velocities (~600 m a^{-1}) of ‘tributary 1’. There is a very abrupt transition from fast-flowing to slow-flowing ice. If this system surged in 1987, possibly 2001 or 2002, and now in 2012 or 2013, then the periodicity of the reactivation of this system is in the range of 10-15 years.

Hubbard Glacier trunk

Centreline velocity profiles were plotted down the main trunk of the Hubbard Glacier from the west arm to the terminus, and down the Hubbard East Arm to its confluence with the main West Arm of the glacier (figure 4.23). The main centreline (West Arm-terminus) is split over two plots (Figure 4.26a and Figure 4.27a) because of the large range of velocities along the centreline. The first covers the main trunk of the glacier from km 0 to km 95, while the second runs from km 95 to the terminus, capturing the highest velocities towards the terminus. Because of the overlap of the Landsat images p061r018 and p062r018, there is quite frequent coverage of the upper Hubbard Glacier. The velocity of the main trunk follows a generally increasing pattern (Figure 4.26a) from a minimum of ~35 m a^{-1} in the upper reaches to ~800 m a^{-1} at the mouth of the Hubbard Throat. Superimposed on this are velocity peaks at km 2.5, km 20, km 30 and km 65 that seem to be related to tributary confluences and narrow points in the valley.

There is good agreement (within 50-70 m a^{-1}) between the velocities derived from feature tracking in 1987-88 and 2000-01, and from speckle tracking in 2012. There seems to be far less interannual variability relative to the magnitude of flow than was observed at various surge-type glaciers elsewhere in this study. An exception to this good agreement is the 1997-98 centreline velocity which, although following the same pattern of increase and decrease, is significantly lower (up to 100 m a^{-1}) than the velocity of the other years, as was also noted at the terminus of the Kaskawulsh Glacier. Variability in the 2011 profile is high as the speckle tracking results were very patchy along the central glacier, and interpolation artifacts are present. The errors in that date pair are consequently higher, as shown by the error bars.

The East Arm joins the main West Arm at ~km 76 of the ‘Hubbard’ profile. It is characterized by two velocity peaks before decreasing in velocity to the juncture with the main Hubbard Glacier (Figure 4.26b). Velocity peaks at 585 m a^{-1} at km 26 before decreasing to between 200-250 m a^{-1} just north of the confluence. As before, velocities in 1986-87, 1987-88, 2000-01 and 2012 agree closely with each other, within 50 m a^{-1}. The 1997-98 velocities are significantly lower. The 2011 velocity profile is intermediate, significantly lower than 2012, especially in the upper reaches of the glacier and at the locations of peak velocity, but generally higher than the 1997-98 velocities. Velocities downglacier of the point where the Queen Mary tributaries join the flow of the East Arm at km 34 are not significantly different between the surging years 1986-88 and non-surging years 2011 and 2012, which suggests that surge velocities do not propagate into the main glacier.

Most of the Hubbard Glacier passes through a narrow valley before flowing into the wider terminal area. Centreline velocities through this valley to the terminus are shown in Figure 4.27a. There is a rapid increase in velocity just downglacier of the confluence with the main trunk and the southeast tributaries at the mouth of the narrow valley. In ~4 km, the velocity increases by >1500 m a^{-1} (from ~750 m a^{-1} to 2487 m a^{-1}). For the next 8 km, velocity is relatively steady at ~2500 m a^{-1} before increasing to ~4000 m a^{-1} or higher at the bottom of the valley. As the glacier area widens into the terminus, velocity decreases substantially to ~2000 m a^{-1}. The Valerie Glacier enters from the West at about this point, and form here, the glacier accelerates to the terminus. Near the ice face, velocity is ~3300 m a^{-1}.

The velocity of the Hubbard terminus was derived from speckle tracking in winter 2011 (upper Hubbard throat only) and 2012, and from feature tracking of September 1988 and June 1998 Landsat imagery. Variability between the profiles is greatest at km 102 (500 m a^{-1} between 2012 and 1998), km 111 (400 m a^{-1} between 2012 and 1998) and km 116.5-119 (600 m a^{-1} between 2012 and 1998). Over the length of the profile, there is no consistent pattern of change through time although there is an apparent increase in velocity at km 115-120 from 1998 to 2012.

In the summer of 1978, Krimmel and Sikonia established a network of 51 stakes on the terminal ~12 km of the Hubbard Glacier (Figure 4.29a). UTM coordinates and velocities (m d^{-1}) at these stakes are given in Krimmel and Sikonia (1986). Velocities from the 1988, 1998, 2011 and 2012 analyses were extracted at the same locations and plotted against the August 1978 velocities (Figure 4.29c). At low (<1000 m a^{-1}) and high (>3000 m a^{-1}) velocities, there is no significant trend in the change in velocity. However, at intermediate values, generally corresponding to the central area of the terminus, the data of the different years are clustered so as to indicate an increase in velocity over time that is significant given the measurement error. From 1978 to 1988 there was no change; however, from 1988 to 1998, velocities are higher by ~250 m a^{-1}, increasing to ~500 m a^{-1} by winter 2012. In addition, the area of high velocity expands from 1988 to 1998 to 2012 (Figure 4.29b). This result is shown as well in the Hubbard terminus centreline profile (Figure 4.27a.).

Valerie Glacier

Centreline velocities were measured on the Valerie Glacier from 2011 (upper glacier only), 2012 and June 1998, and the results are shown in Figure 4.28b. The glacier velocity increases at a rate of ~20 m a^{-1} km^{-1} until km 11 where it increases rapidly to a peak of 1300-1400 m a^{-1} at km 14.5. The 2011 and 2012 velocities agree closely, with <50 m a^{-1} variation between the two. The June 1998 profile also agrees with the 2011/2012 profiles, except for a portion of the glacier between km 6 and km 10 where velocities are up to 50% (200 m a^{-1}) higher. From km 17 the measured velocities in 2012 and 1998 diverge. 2012 velocities continue to rise, reaching a peak at km 36.5 of 1546 m a^{-1}. In 1998, velocity decreases to a minimum at km 30.5 before increasing towards its juncture with the Hubbard Glacier. The Valerie was observed to surge in 1986 with peak velocities greater than 27 m d^{-1} and seasonal variation in quiescence was estimated at 1000 m a^{-1}, although this was from a very sparse dataset (Mayo, 1989). Given that the winter 2012 velocities are ~600 m a^{-1} faster than the 1998 summer velocities, it is possible the Valerie Glacier is headed into a surge.

It is unclear how the upper 10 km participates in the surges. There is a sharp 90^{o} bend in the glacier at ~ km 16. This may be important in creating a significant impediment to flow, although a second sharp bend at km 20 does not seem to have the same effect. Such an impediment may result in a buildup of mass in the upper glacier, until accumulation is sufficient to initiate the rapid release of the mass imbalance as a surge. Such a scenario would explain higher velocity above km 10 and lower velocity from km 15 onward in 1998, but the limited spatial extent of the velocity difference in the upper glacier leaves this open to doubt. Figure 4.28 gives the detailed 2012 velocity structure of Valerie Glacier and its confluence with the Hubbard terminus. It shows the pattern of flow through the sharp bends of the upper Valerie Glacier and the high 2012 velocities to its confluence with the Hubbard Glacier. At the confluence, Valerie Glacier ice extends past the valley mouth into the flow of the Hubbard Glacier before sharply merging into its southwesterly flow. Mayo (1989) suggests that because of this structure, surges of this glacier may provide enough lateral pressure to contribute to closures of Russell Fjord.

Variegated Glacier

Variegated Glacier has been the subject of detailed velocity (among other) investigations. In particular, Raymond and Harrison (1988) mapped the evolution of the velocity structure of this glacier in relation to its changing geometry during quiescence. Figure 4.30 presents the minimum (1974) and maximum (1981) quiescent winter velocities from Raymond and Harrison (1988) in relation to the 2012 results derived from speckle tracking. The errors in the speckle tracking analysis are regrettably high, a result of the glacier’s location in a zone of otherwise fast-flowing glaciers, near the margin of the images. The comparison illustrates well that the glacier is currently in the early stages of quiescence, and raises the intriguing question of whether the quiescent velocity evolution of a given glacier could be used to estimate its stage in the surge cycle.

4.3.6 Malaspina System and Icy Bay Drainage

The Malaspina Glacier is the largest piedmont glacier in the world. It is trilobate, and the main influx of ice is from the Seward Glacier that feeds the central lobe. The Seward Glacier has a large accumulation basin partitioned into a zone of fast flow from the west to east along the southern margin and slower-flowing tributaries draining the upper basin (as shown in Figure 4.31a). The entirety of this ice flux is funneled through a narrow valley (the Lower Seward Glacier) before flowing unconfined in the Malaspina piedmont. To the east, the piedmont is fed by Marvine Glacier, and to the west by the Agassiz Glacier (Figure 4.32). The Lower Seward, Agassiz and Marvine glaciers all surge (Muskett et al., 2008).

There are two significant tidewater glaciers that are partially contained within the 2012 study area, the Tyndall and Yahtse Glaciers. These drain into Icy Bay just west of the Malaspina Glacier (Figure 4.32). They underwent drastic retreat during the 1940s (Field, 1975). Examining archived Landsat images since 1972, it seems that both the Tyndall and Yahtse glaciers stabilized by 1987, and have since advanced slightly to their current positions. In 2012, the velocity of Yahtse Glacier 5.5 km from its terminus was 1759 m a^{-1}. At a position <1 km from the terminus of Tyndall Glacier, the 2012 velocity was 1250 m a^{-1}.

Seward Glacier

Although the Lower Seward Glacier is known to surge, it is unclear whether the northern part of the upper basin participates in the surges, or if they are largely driven by and confined to the fast-flowing stream along the southern margin of the glacier. Muskett et al. (2008) showed that the 1999-2002 surge of the Lower Glacier was accompanied by accelerated surface lowering in the western part of the upper glacier, indicating that this fast-flowing section did participate in the surge, but their data did not cover the northern part of the basin. A centreline was plotted along one of the more active northern tributaries since it had high-quality coverage over all four measurement periods (1986-87, 2000-01, 2011, 2012) (Figure 4.32).

Velocity results for this tributary show remarkable agreement between the measurement periods (Figure 4.31). The four velocity profiles are within 35 m a^{-1} of each other over much of their length, well within the measurement error. Tributary velocities are highest close to the headwall and then rapidly decrease. There is a peak at km 7, which is just south of the junction of the three small tributaries that feed this branch. Velocities then decrease gradually until the tributary joins with the main flow of the other upper tributaries. The profile of this glacier is characterised by step increases in velocity when the centreline crosses into a zone of faster flow. The first step occurs at ~ km 16 when the tributary joins the upper W-E ice stream, and the second occurs at km 27 when the centreline enters the fast-flowing lower W-E ice stream. There is significant variability between the different measurement periods only once the profile attains this fast-flowing southern flow band, when the difference between 1986-87 velocity and 2012 velocity is 129 m a^{-1}. The 2000-2001 velocity of the tributary and the northern ice stream does not seem to be affected by the surge of the Lower Seward Glacier between 1999 and 2002.

The velocity of the southern ice stream of the Upper Seward Glacier and the Lower Seward Glacier is shown in Figure 4.34a. Feature tracking of the Landsat images used above was unsuccessful over large areas and is not included here. The 2011 record is also patchy, though it generally agrees well with the 2012 profile where good quality results were present. The initial high velocities correspond to a steep tributary. The velocity of the Upper Seward Glacier increases gradually and steadily at a rate of 12 m a^{-1} km^{-1} in the fast-flowing southern ice stream from km 5 to the juncture with the northern W-E ice stream at km 35. With the influx of ice from the northern ice stream, the rate of acceleration with distance increases to 43 m a^{-1} km^{-1} to the mouth of the Lower Seward Glacier at km 48. The Lower Seward Glacier has large variations in velocity over its length. The locations of peak velocity coincide with the narrowest points of the valley, while valley widenings are associated with decreases in velocity. The profile obtained for the Lower Seward Glacier agrees qualitatively with the Lower Seward velocity results obtained by Headley et al. (2012) from speckle tracking of Sept.-Oct. 2000 Radarsat-1 fine-beam images. The magnitude of velocity at the mouth of the Lower Seward is less than that of this analysis by several hundred metres per year, but this could be influenced by the positioning of the centreline, as well as seasonal variability.

Agassiz

There have been no previous measurements of quiescent or surge velocities of the Agassiz Glacier. In this study, velocities were derived over most of the glacier length in 2011 and 2012 from speckle tracking. Feature tracking of the 1986-87 and 2000-01 image pairs yielded extremely patchy results that are not shown here. The results are shown in Figure 4.34b. The background velocity is ~600 m a^{-1}, with a velocity peak at km 10-13 of ~1600 m a^{-1} and another at km 15-21 of ~1200 m a^{-1}. Velocity of the lower glacier in 2011 and 2012 is not appreciably different, although the upper glacier shows indications of an increase in velocity from 2011 to 2012 of 200-300 m a^{-1}.

Good quality results were also achieved in both 2011 and 2012 for two small tributaries of Libbey Glacier (itself a western tributary to the Agassiz Glacier, joining near the junction with the Malaspina). Its position is labeled in Figure 4.32, and 2012 velocity results for the pair are shown in Figure 4.31b. Both show an appreciable increase in velocity between the two years, as well as downglacier enlargement of the zone of fast flow. The easternmost of the pair shows the greater increase, from 238 m a^{-1} in 2011 to 547 m a^{-1} in 2012 in the upper reaches of the glacier. The maximum acceleration occurred in the mid-glacier where there was a nearly twenty-fold increase in velocity from 2011 to 2012 (23 m a^{-1} to 425 m a^{-1}). Velocity of the western glacier increased by a factor of 2-3. These glaciers are heavily moraine-covered, and the lower glacier shows evidence of pulses of movement. They appear to be surging in 2012.

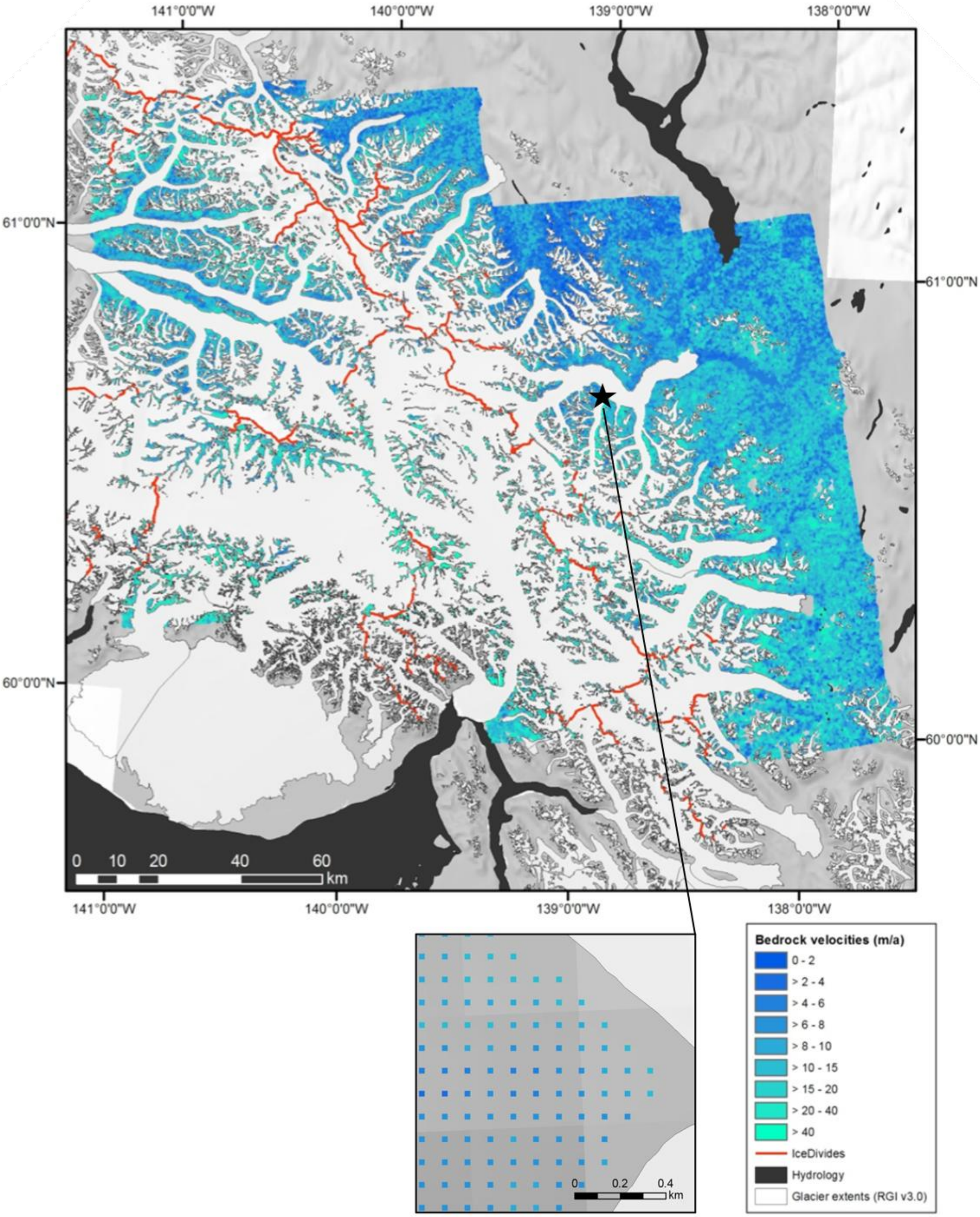

Figure 4.1: Bedrock points more than 200 m from glacier ice, extracted from the 2011 mosaicked velocity raster.

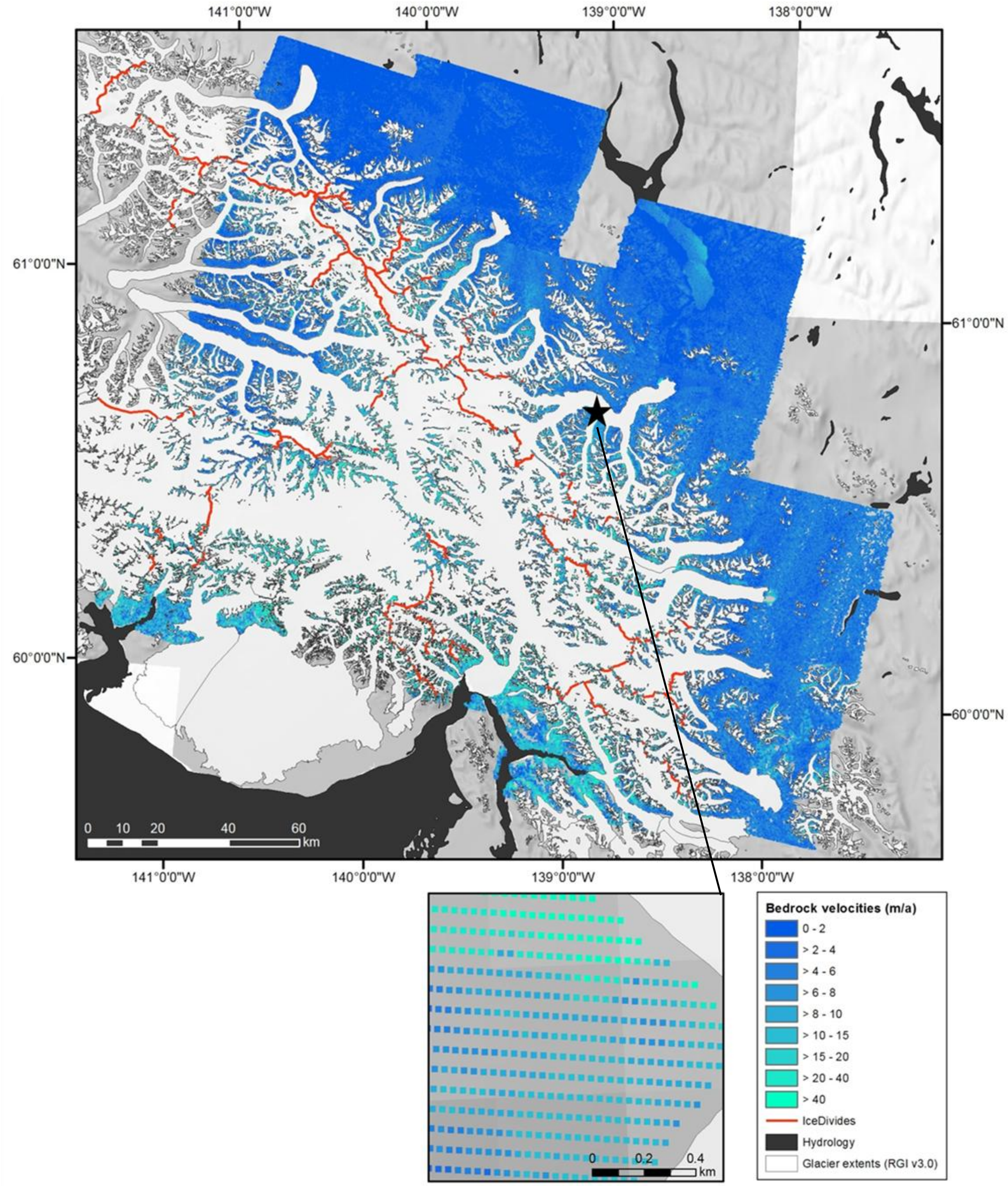

Figure 4.2: Bedrock points more than 100 m from glacier ice, extracted from the 2012 mosaicked velocity raster. This file was used to calculate the mean error of the 2012 mosaic. The bedrock error was also calculated in the same way for each tile individually, the value of which was used in comparing velocity change for individual glaciers. Velocities were also extracted at 10 m increments along the ice divides shown in red.

				Bedrock points					**Ice Divides**				
Year	**Beam code**	**Image Date pair**	**Segment**	**Min (m a^{-1})**	**Max (m a^{-1})**	**Mean (m a^{-1})**	**StanDev**	**Count**	**Min (m a^{-1})**	**Max (m a^{-1})**	**Mean (m a^{-1})**	**StanDev**	**Count**
2011	F6	Jan 03 - Jan 27	1 (composite)	0.60	368.01	17.70	11.68	17570	3.36	164.18	32.41	24.19	8275
			3	0.11	163.74	5.95	3.58	131423	1.37	110.90	19.01	19.75	1634
		Feb 20 - Mar 16	2	0.36	152.58	13.67	8.82	45379	4.23	74.02	22.46	12.02	4350
	F2F	Jan 10 - Feb 03	2	0.86	338.01	12.93	9.75	49028	1.92	71.62	15.27	12.30	4419
			3	0.13	151.80	12.61	7.90	57187	1.97	72.31	20.84	13.05	11481
		Feb 27 - Mar 23	1 (composite)	0.49	1073.50	20.81	23.44	14681	2.05	93.46	19.30	15.56	4566
	F23F	Feb 14 - Mar 10	1	0.13	174.10	13.39	6.85	138954	1.69	62.83	23.07	13.00	2121
			2	0.14	233.38	13.17	6.51	189994	no ice divides				
			3	0.00	77.20	10.44	5.30	230690	no ice divides				
	F2	Jan 17 - Feb 10	1	7.34	385.00	55.70	26.51	5573	5.06	139.25	44.82	16.42	3594
			2	0.19	265.97	12.28	11.55	21743	1.40	120.44	24.61	17.63	5713
			3	0.48	278.33	10.30	7.01	71126	2.56	99.00	28.74	19.16	12490
			Avg			**16.58**	**10.74**				**24.89**	**16.31**	
			2011 mosaic	**0.11**	**1073.50**	**11.58**	**7.86**	**670338**	**1.37**	**164.18**	**27.62**	**19.24**	**39886**

Table 4.1: Apparent velocity over bedrock outcrops and ice divides, derived from the 2011 velocity fields of all fully-processed individual tiles, and of the mosaicked raster. Beam code and segment number are as in figure 2.2 and table 2.1.

				Bedrock points					Ice Divides				
Year	**Beam code**	**Image Date pair**	**Segment**	**Min (m a^{-1})**	**Max (m a^{-1})**	**Mean (m a^{-1})**	**StanDev**	**Count**	**Min (m a^{-1})**	**Max (m a^{-1})**	**Mean (m a^{-1})**	**StanDev**	**Count**
2012	U1W2	Feb 17 - Mar 12	1	0.00	218.59	2.53	2.75	629413	0.64	92.25	12.65	12.29	9456
			2	0.08	228.77	5.09	5.81	258343	0.84	61.49	8.49	6.61	7306
			3	0.23	521.88	8.85	10.28	115558	0.86	76.11	14.05	12.70	4351
			4	0.15	895.05	12.84	15.70	133785	5.48	122.96	28.18	21.32	1423
	U2W2	Feb 24 - Mar 19	1	0.03	112.77	2.18	2.23	996679	1.43	33.95	11.25	7.75	964
			2	0.05	259.03	4.92	8.31	273546	0.08	183.11	11.91	11.22	14457
			3	0.22	387.36	14.39	15.80	71894	0.71	294.35	14.70	24.78	4436
			4 (30 shifts west half)	0.71	965.25	36.97	57.76	11316	3.16	342.88	65.22	76.04	1594
			4 (30 shifts east half)	0.59	590.24	34.85	65.74	21274	no ice divides				
			4 (70 shifts west half)	0.18	653.47	37.73	65.89	18458	no ice divides				
		Mar 19 - Apr 12	1										
			2	0.22	292.38	8.75	6.20	264842	1.54	80.65	11.96	6.87	11332
			3	0.48	609.25	16.92	14.54	73050	1.60	236.37	16.72	21.53	4500
			4 (composite)	0.84	586.05	23.64	19.95	19438	no ice divides				
	U9W2	Feb 21 - Mar 16	1	0.02	68.87	3.09	1.82	1012228	no ice divides				
			2	0.11	144.15	5.70	4.95	498084	2.42	41.26	12.96	7.37	1278
			3	0.14	464.26	12.59	14.47	96709	0.90	167.29	18.21	20.38	8045
			4	0.15	472.31	12.37	12.16	179610	1.85	167.99	23.36	24.03	3188
	U10W2	Feb 28 - Mar 23	2	0.08	138.72	4.56	1.96	850716	2.04	14.60	5.22	2.57	428
			3	0.06	82.07	5.22	3.09	496763	1.38	49.41	13.30	8.70	3064
	U24W2	Feb 18 - Mar 13	1	0.12	143.87	4.70	2.61	377610	0.91	49.23	12.27	9.28	1706
			2	0.08	401.42	7.78	9.23	68207	1.23	93.52	13.99	12.46	5278
			3 (24 shifts)	0.38	514.90	14.29	13.58	75463	4.16	91.12	21.24	14.22	3152
			3 (40 shifts)	0.00	945.22	13.72	18.50	79556	0.47	123.42	20.72	19.31	2952
		Mar 13 - Apr 06	1	0.06	141.27	4.62	2.48	379162	1.40	54.39	12.55	7.22	2072
			2	0.36	316.95	10.75	7.73	73638	2.30	179.35	16.92	17.59	5712
			3 (24 shifts)	0.38	728.20	13.98	116.68	79928	3.55	180.35	23.93	18.64	3577
			3 (50 shifts)	0.00	911.41	14.32	23.17	69138	1.70	101.46	23.64	15.14	2517
			3 (70-90 shifts)	0.14	1058.53	17.06	39.31	24244	no ice divides				
			Avg			**12.66**	**20.10**				**17.98**	**16.44**	
			2012 mosaic	**0.02**	**898.93**	**4.97**	**7.17**	**4371651**	**2.67**	**342.88**	**16.94**	**21.03**	**46436**

Table 4.2: Apparent velocity over bedrock outcrops and ice divides, derived from the 2012 velocity fields of individual tiles, and of the mosaicked raster. Beam code and segment are as in figure 2.2 and table 2.1.

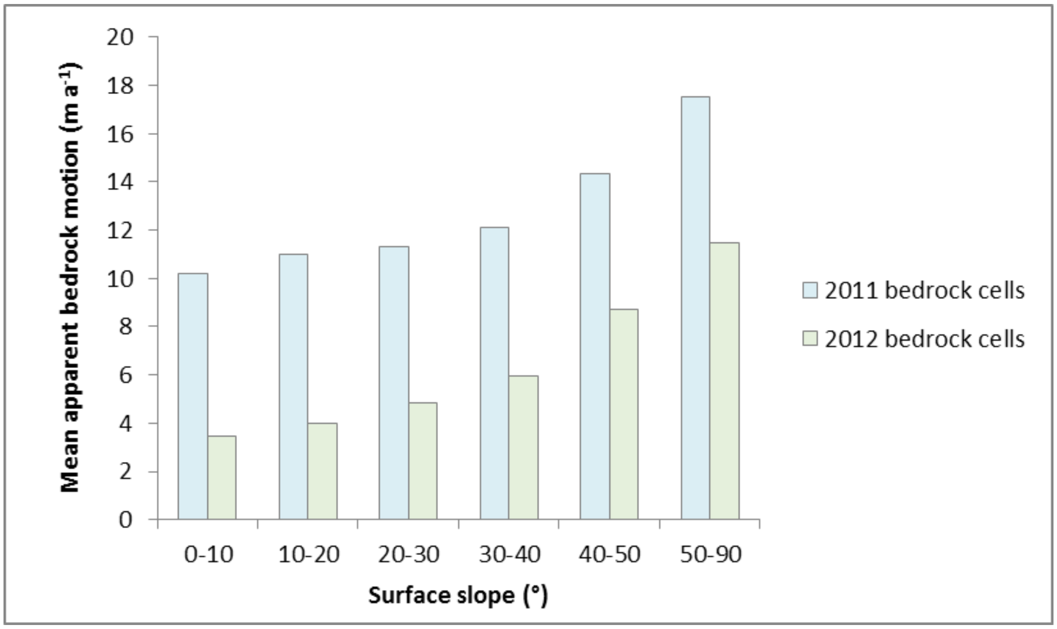

Figure 4.3: Relation of apparent bedrock velocity with slope angle in the 2011 and 2012 regional velocity mosaics.

Landsat path/row identifier	Image date pair	Glacier area processed	Bedrock points		
			Mean (m a^{-1})	Max (m a^{-1})	StanDev
p061 r018	09/09/1988 - 09/25/1988	Hubbard Gl. terminus	58.18	616.89	78.58
		Upper Hubbard Gl.	no bedrock values		
	06/17/1998 - 07/03/1998	Hubbard Gl. terminus	104.10	597.32	90.99
	08/22/1987 - 09/09/1988	Upper Hubbard Gl.	11.02	483.92	47.41
		Kaskawulsh Gl.	10.73	105.70	9.13
		Lowell Gl.	9.60	49.90	6.94
	06/30/1997 - 06/17/1998	Upper Hubbard Gl.	4.96	53.40	4.64
		Kaskawulsh Gl.	4.93	59.97	5.48
p062 r018	09/11/1986 - 08/29/1987	Seward Gl.	12.26	52.38	6.75
		Upper Hubbard Gl.	9.41	44.79	5.48
	07/07/2000 - 08/11/2001	Seward Gl.	9.89	40.19	5.55
		Upper Hubbard Gl.	20.44	57.74	5.58
	09/11/1986 - 08/30/1999	Logan Gl.	1.75	23.62	1.72
p062 r017	09/15/1996 - 09/24/1997	Donjek Gl.	7.63	98.19	8.03

Table 4.3: Apparent velocity over bedrock outcrops, summarized from the filtered velocity fields derived from feature tracking of archived Landsat-5 imagery.

From *Date 1*	**To *Date 2***	**Station**	**GPS Δd (m)**	**GPS v (m a^{-1})**	**ST v (m a^{-1})**	**Absolute difference (m a^{-1})**	**% difference (% of GPS velocity)**	**GPS Δd direction (°)**	**ST Δd direction (°)**	**Absolute difference (°)**
Jan. 03, 2011 03:11:22	Jan. 27, 2011 03:11:22	Upper	9.00	136.81	131.84	-4.97	-3.63	44.90	46.30	1.40
		Middle	8.31	126.44	126.12	-0.32	-0.25	123.28	126.83	3.55
		South Arm	9.42	143.27	138.34	-4.93	-3.44	10.96	2.21	8.75
		Lower	9.83	149.53	154.33	+4.79	+3.20	51.26	51.48	0.22
Feb. 14, 2011 02:46:25	Mar. 10, 2011 02:46:25	South Arm	10.42	158.45	151.38	-7.07	-4.46	10.29	no data	no data
		Lower	8.91	135.56	141.81	+6.25	+4.61	51.49	no data	no data
Feb. 18, 2012 15:25:22	Mar. 13, 2012 15:25:22	Upper	9.56	145.37	139.90	-5.46	-3.75	45.72	49.53	3.82
Mar. 13, 2012 15:25:22	Apr. 06, 2012 15:25:22	Upper	9.46	143.84	142.65	-1.19	-0.82	45.68	48.22	2.54
Feb. 21, 2012 15:37:50	Mar. 16, 2012 15:37:50	South Arm	9.91	150.77	147.71	-3.06	-2.02	9.84	11.04	1.20
		Lower	10.43	158.68	172.15	+13.47	+8.48	55.11	57.41	2.30

Table 4.4: Comparison of speckle tracking results with Kaskawulsh dGPS measurements from the corresponding time interval. Data recording failed at the ‘middle’ dGPS station for winter 2012.

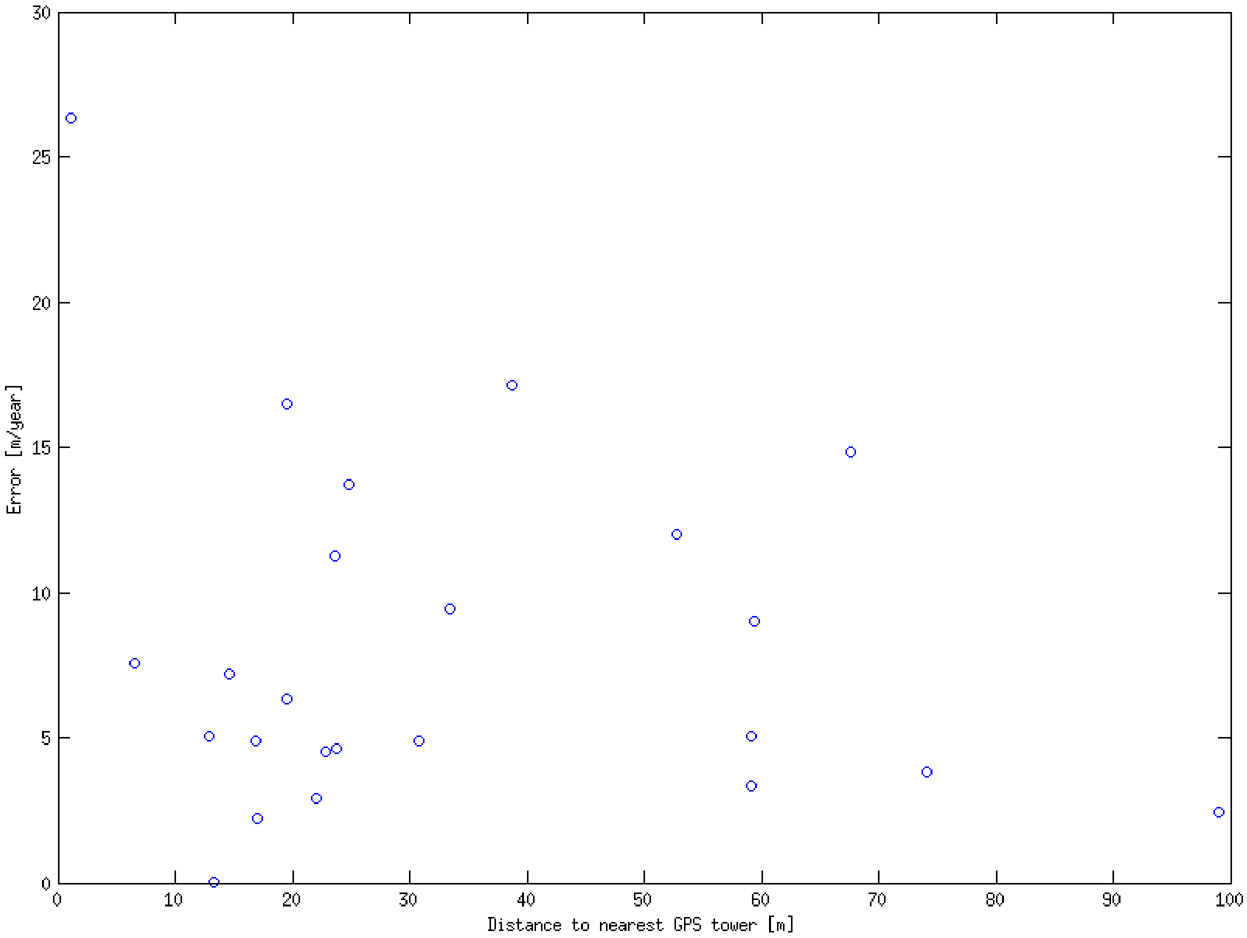

Figure 4.4: Comparison of 2012 speckle tracking velocity field on Glacier One (tributary of the Kaskawulsh Glacier) to the results over the same time interval of the 16 dGPS stations managed by Dr. Gwenn Flowers (Simon Fraser University). GPS velocities were linearly interpolated to the positions of those 2012 speckle tracking point results that were centrally located on the glacier surface, near the dGPS array (24 points). The absolute difference in metres per year is here plotted against the distance to the nearest dGPS measurement, and is less than 15 m a^{-1} for all dGPS stations. The average velocity of this glacier is ~ 25 m a^{-1}. Analysis courtesy of Camilo Rada (University of British Columbia). Figure reproduced with his permission.

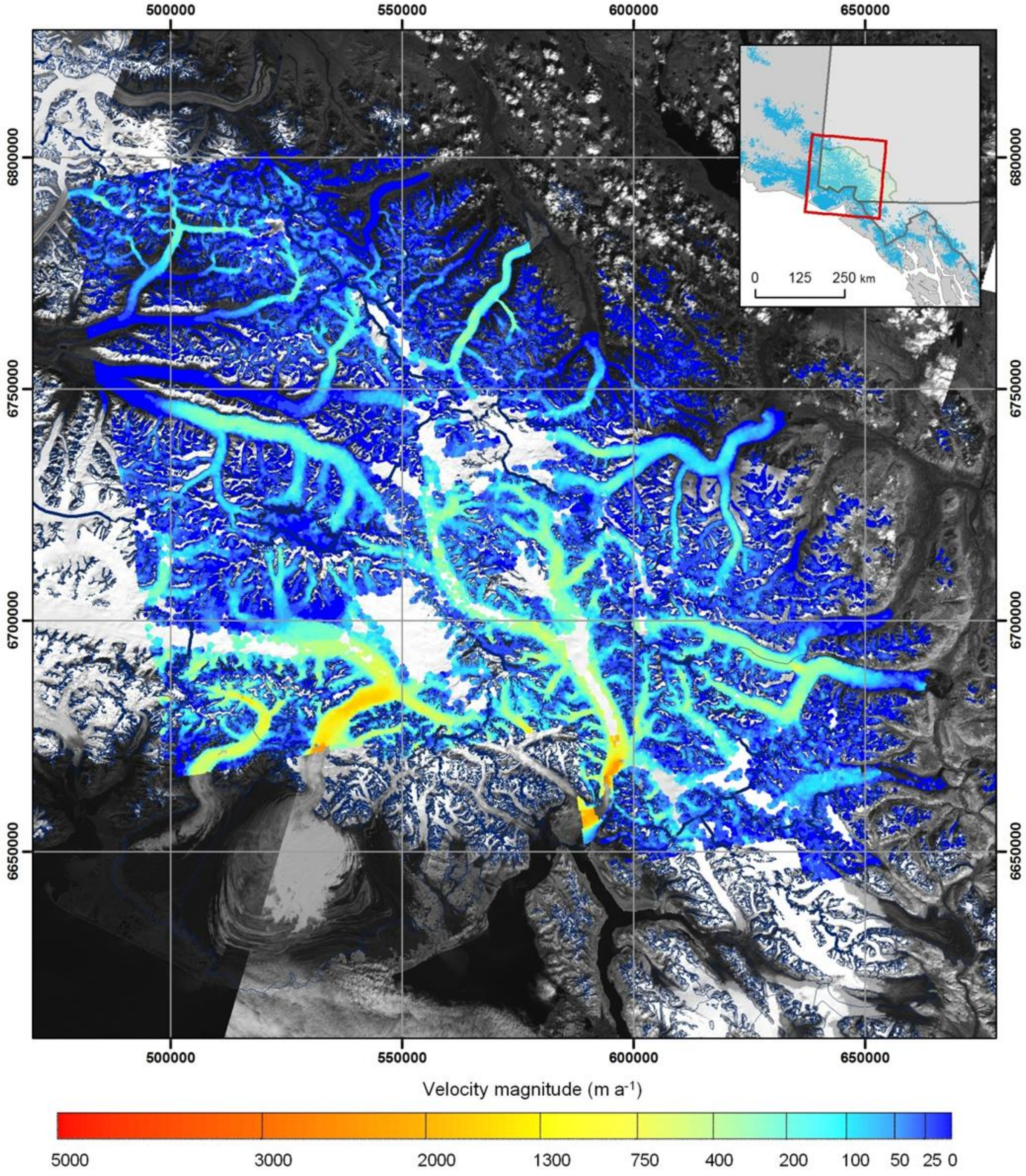

Figure 4.5: 2011 mosaicked velocity map from January-March speckle tracking results, clipped to the RGI v3.0 glacier extents. Tiles have been selected to provide the best quality coverage of the study area. Note that the velocity scale is non-linear. Background image is a mosaic of Landsat-7 images from summer 2000 and 2001. Coordinate system is WGS 1984 UTM zone 7N. Base imagery and coordinate system are consistent across figures unless otherwise indicated.

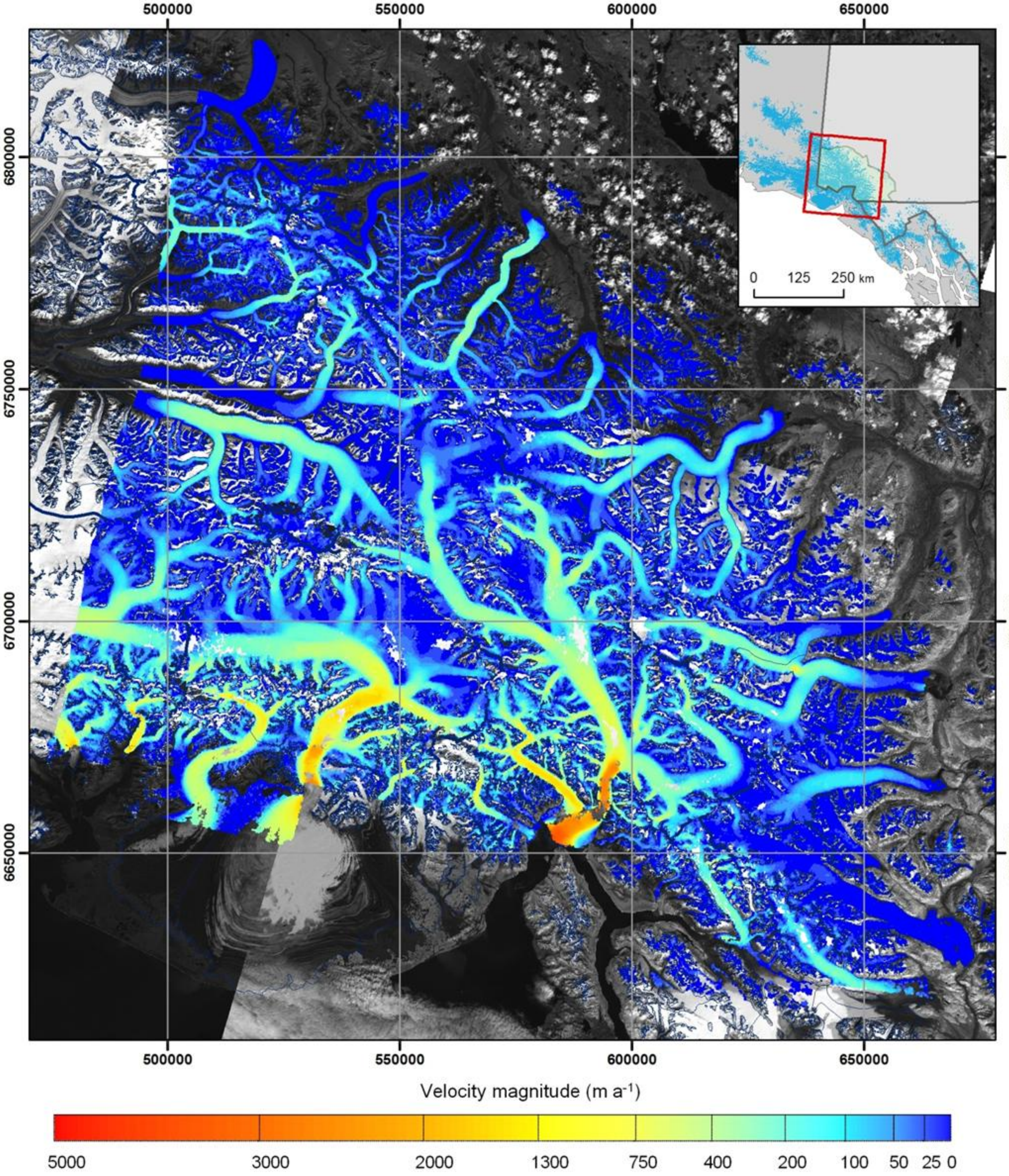

Figure 4.6: 2012 mosaicked velocity map from February-April speckle tracking results, clipped to the RGI v3.0 glacier extents. Tiles have been selected to provide the best quality coverage of the study area. Note that the velocity scale is non-linear.

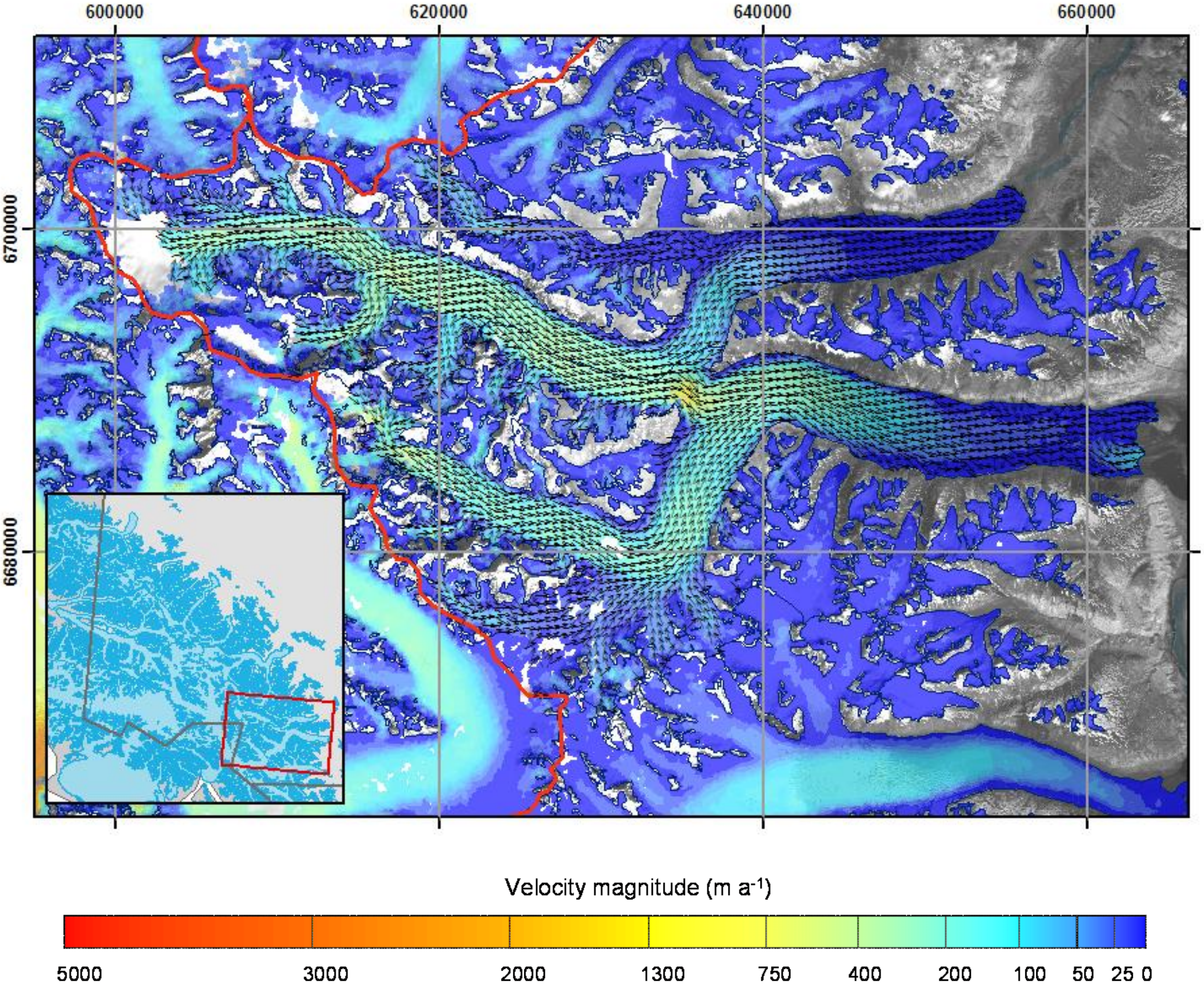

Figure 4.7: Detail of the February-April 2012 velocity of the combined Lowell and Dusty Glacier systems derived from speckle tracking, showing the magnitude of flow coded by colour and direction of flow indicated by the vectors. Ice from the Upper Lowell/Dusty Glacier separates above the icefall to feed the Dusty terminus to the north and the Lowell terminus to the south. Vectors have been downsampled to 500 m for display.

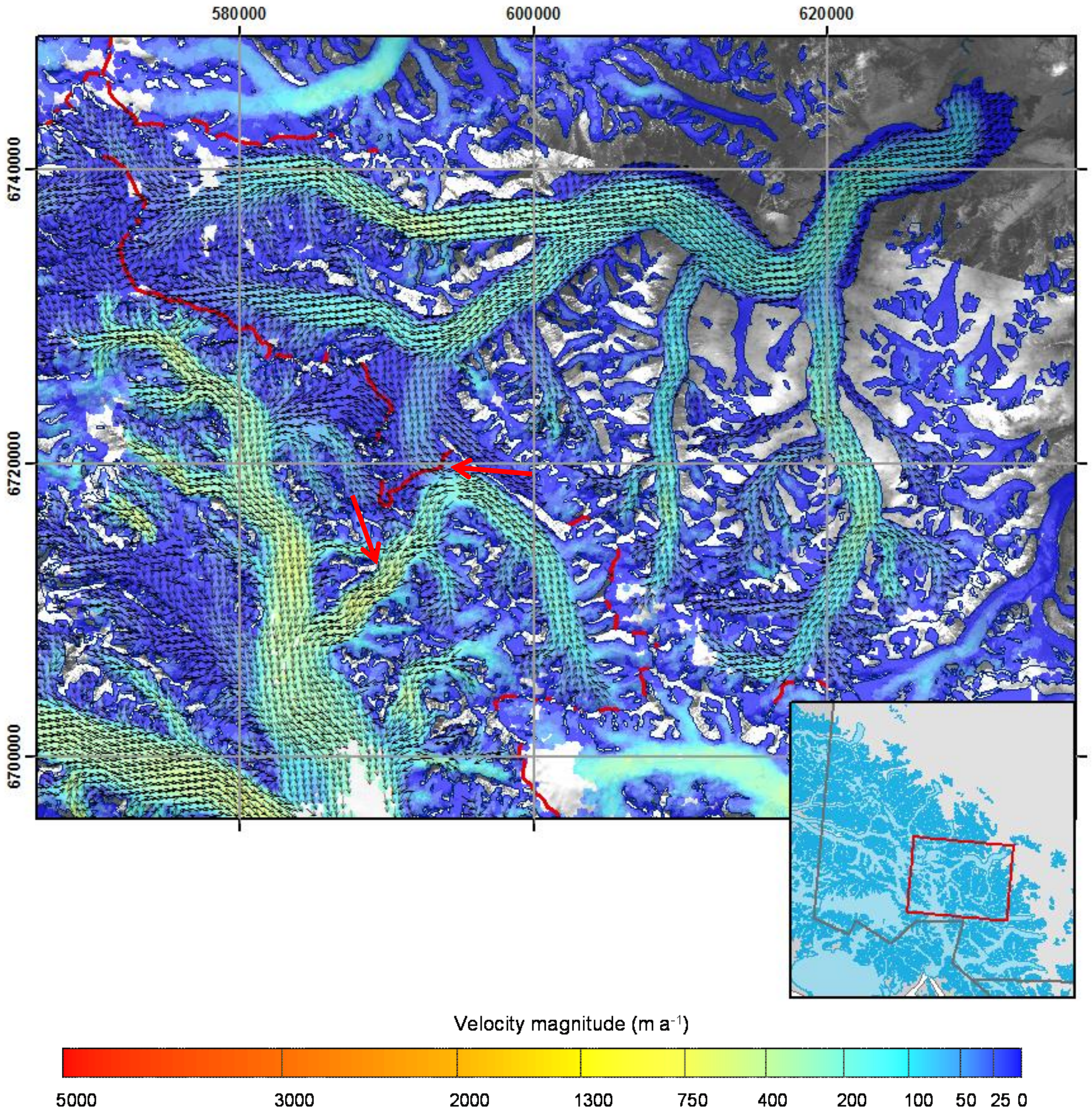

Figure 4.8: Detail of the 2012 velocity of the Kaskawulsh and upper East Arm of the Hubbard Glacier, showing the magnitude of flow coded by colour and direction of flow indicated by the vectors. The large arrows indicate locations where there is ice flow over a basin divide identified in the RGI 3.0 inventory.

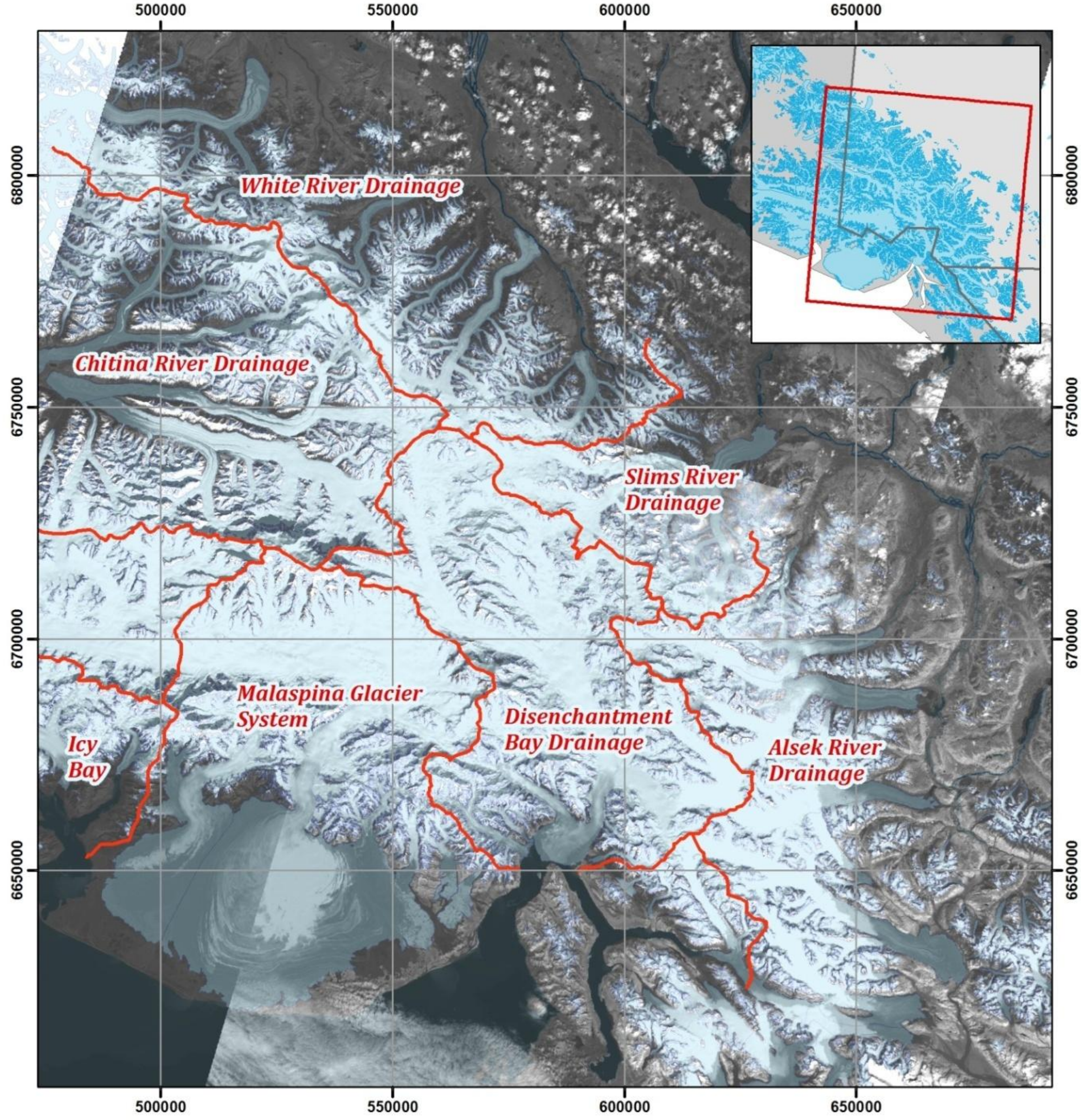

Figure 4.9: Drainage basin divisions as referred to in the coming sections, passing clockwise from the Chitina River Drainage to the Malaspina Glacier System and Icy Bay.

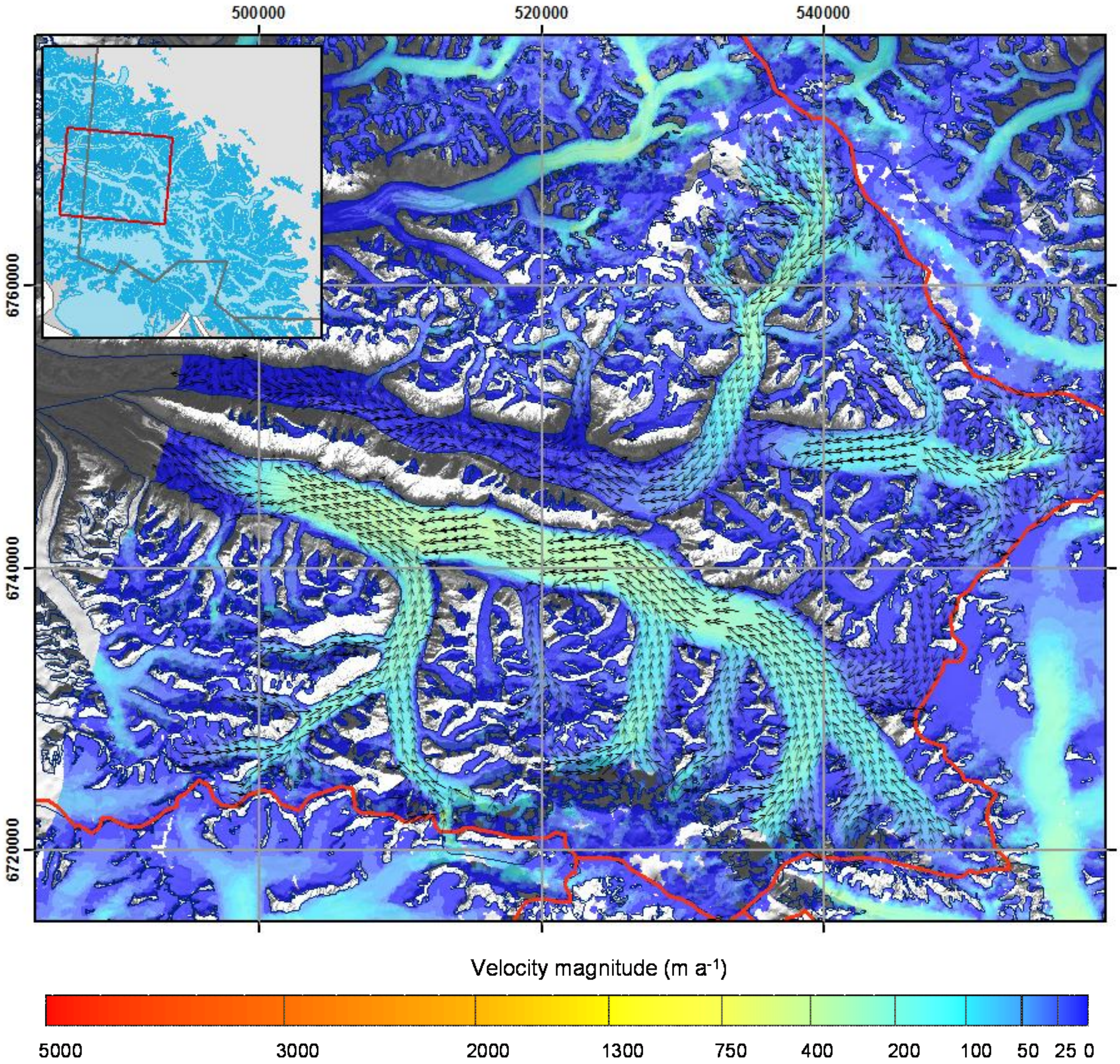

Figure 4.10: Detail of the 2012 Walsh and Logan Glacier flow patterns. As indicated by the loss of coherent flow direction and the low magnitude of flow in its lower reaches, the Walsh Glacier is stagnant along much of its length. The Logan Glacier, on the other hand, is much more active. Vectors have been downsampled to 750 m grid spacing for display.

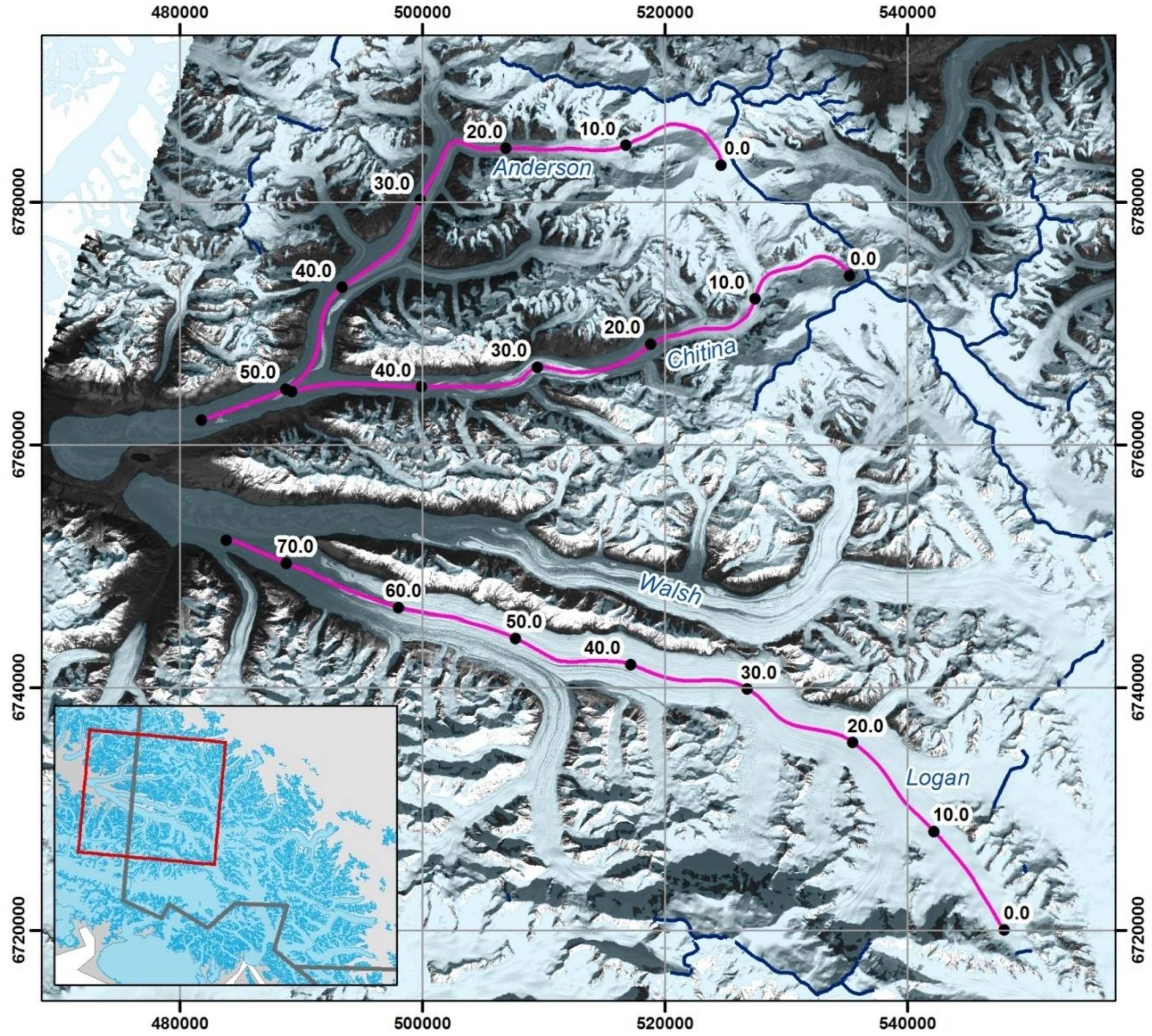

Figure 4.11: Positions of the centrelines along which velocities were extracted to create the longitudinal velocity profiles shown in figure 4.12a, b and c. Kilometre markings are shown along the profile length.

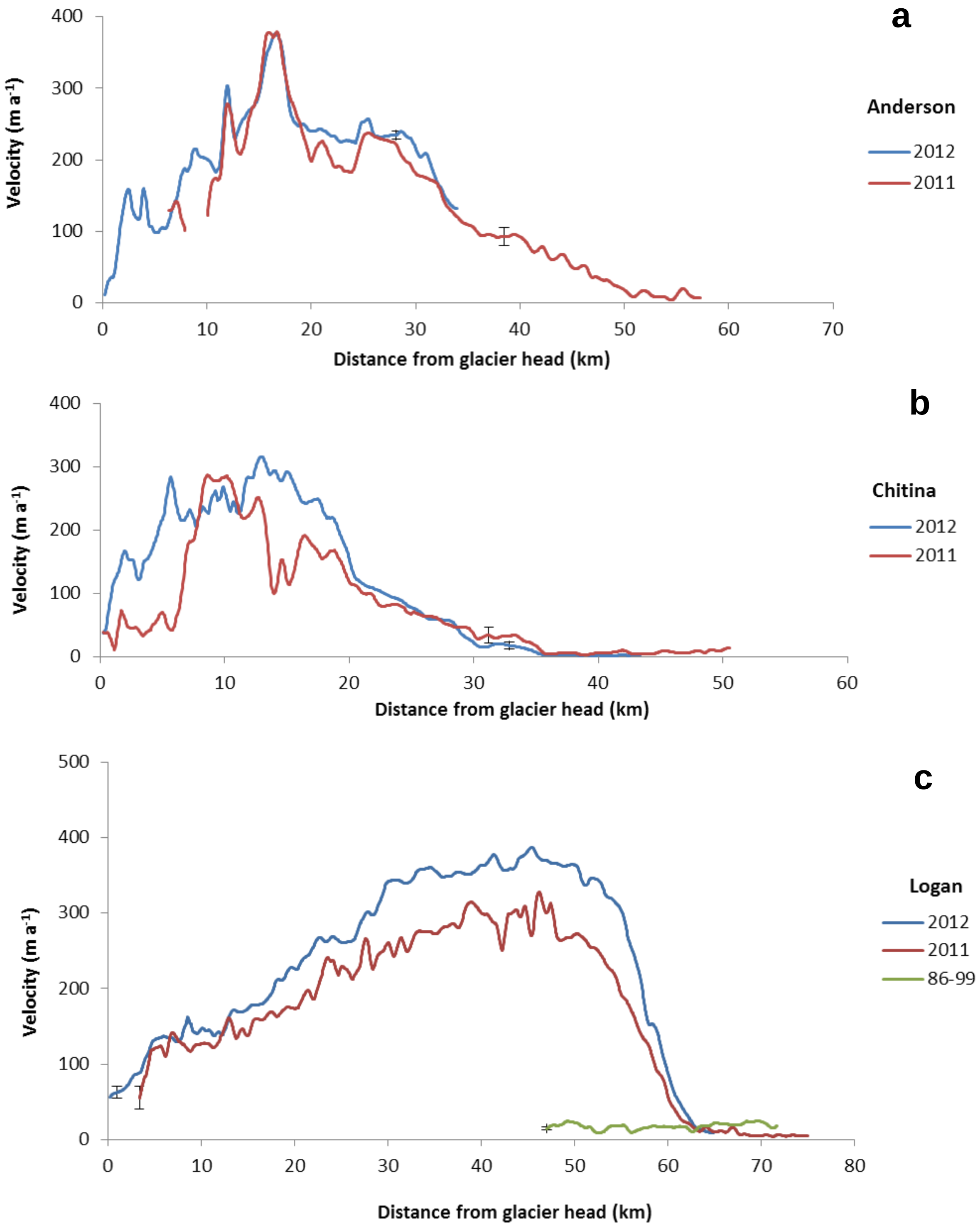

Figure 4.12: Centreline velocity profiles for the (a) Anderson and (b) Chitina Glaciers in the Chitina Glacier system, and for (c) the Logan Glacier. Velocities were extracted from the 2011 and 2012 velocity fields derived from speckle tracking. For the Logan Glacier, velocity was also measured during the interval 1986-1999 using feature tracking of archived Landsat-5 imagery. Velocities were extracted at 50 m increments and averaged over a 500 m moving window. Note that the horizontal and vertical scales vary.

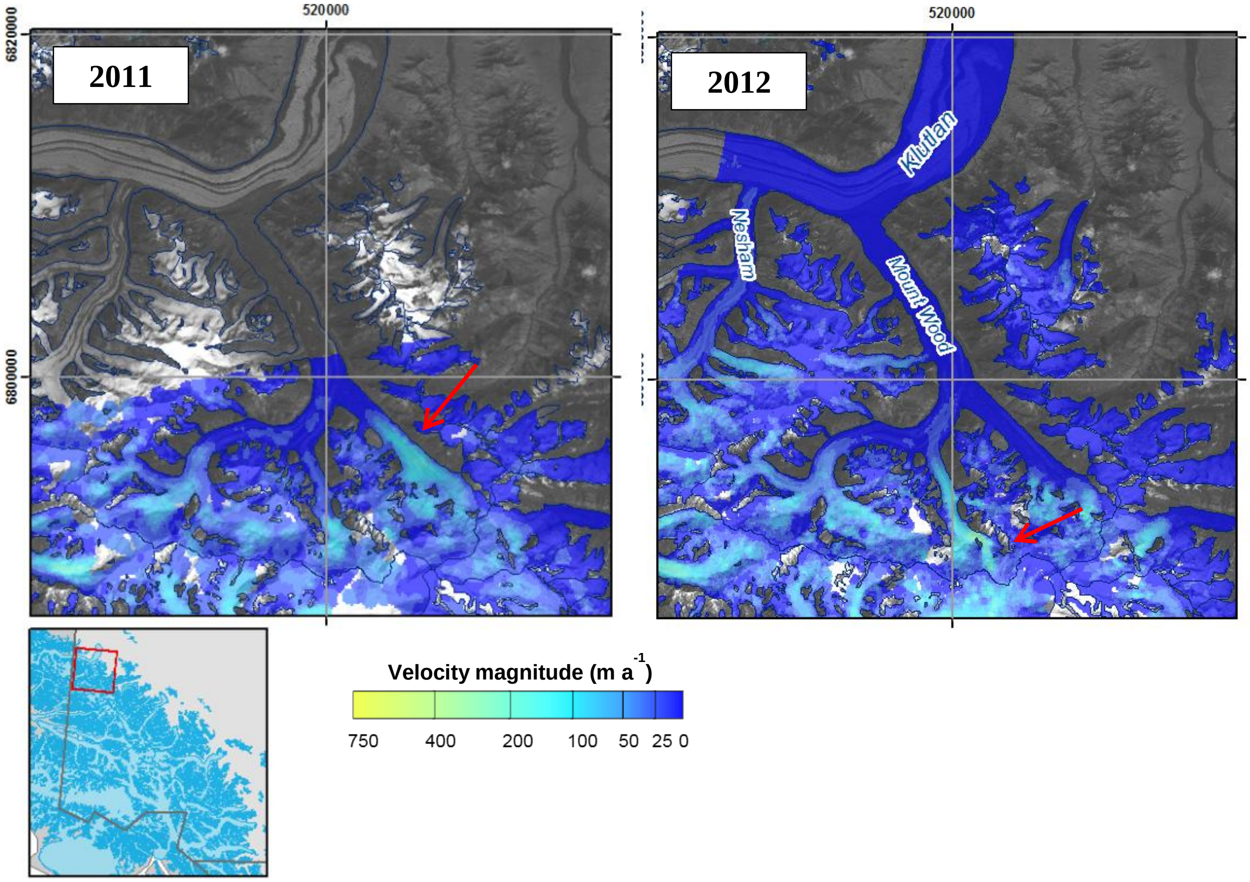

Figure 4.13: Change in velocity between 2011 and 2012 of two tributaries of Mount Wood Glacier. The red arrows indicate the location and timing of surges of these two tributaries.

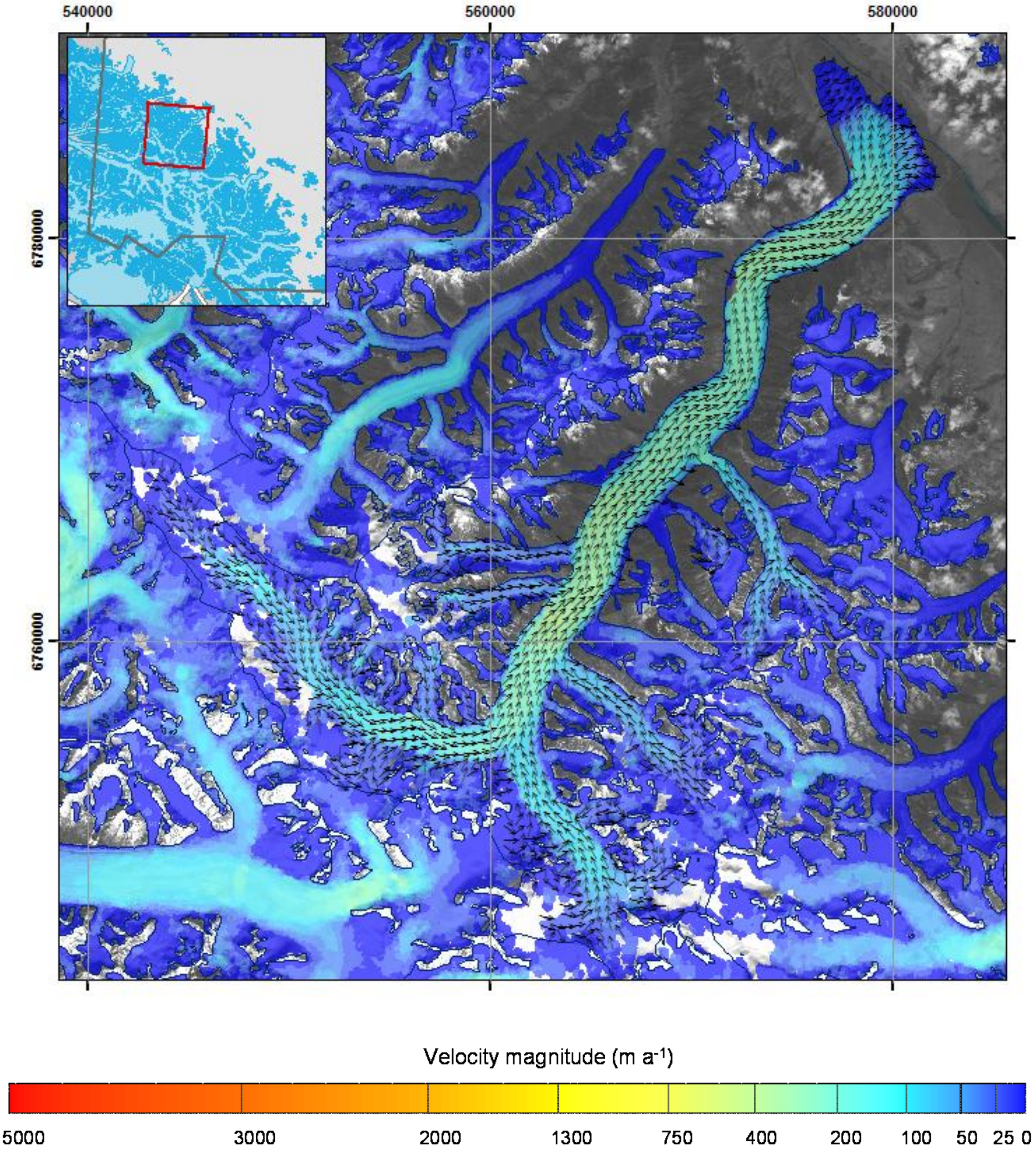

Figure 4.14: Detail of the 2012 Donjek Glacier velocity structure. Vectors have been downsampled to 500 m grid spacing for display.

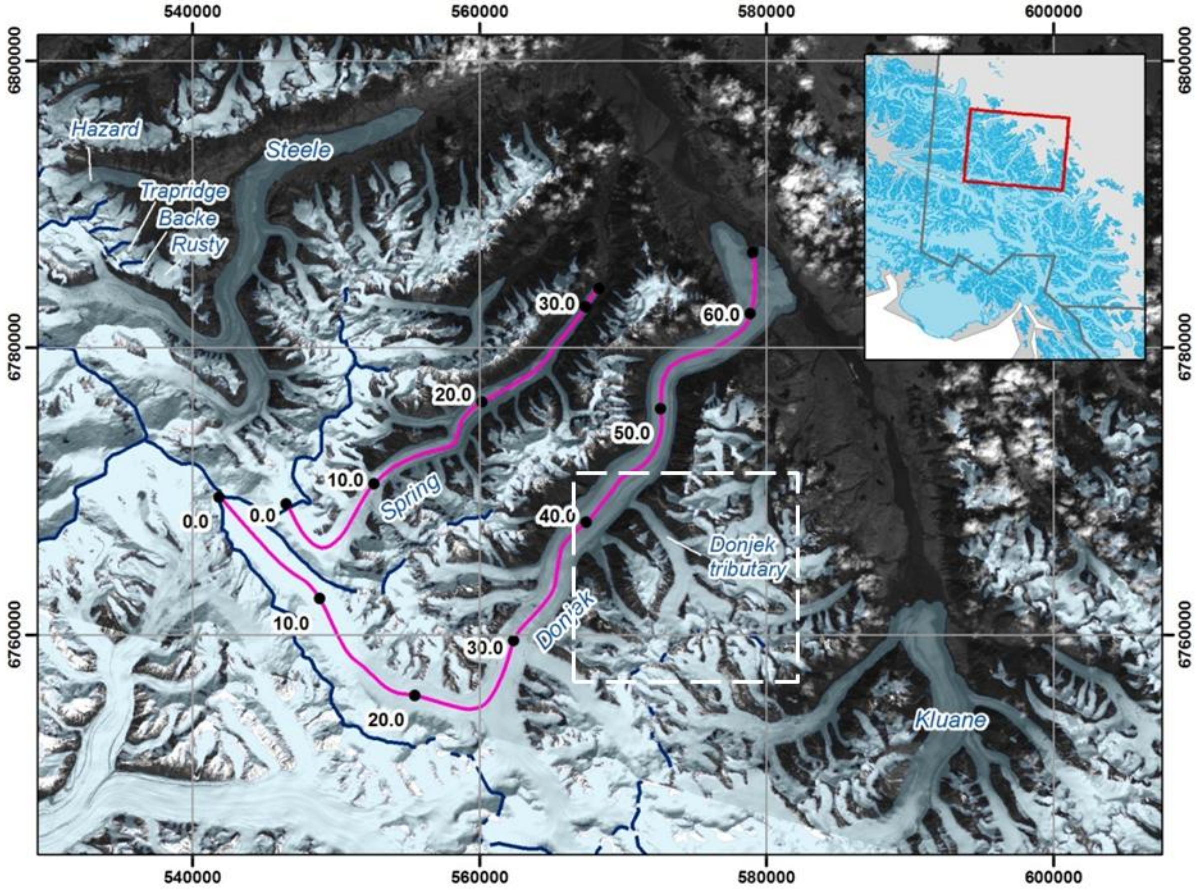

Figure 4.15: Positions of the centrelines along which velocities were extracted to create the longitudinal velocity profiles shown in figure 4.14. Kilometre markings are shown along the profile length. The inset box indicates the location of the detail shown in figure 4.13.

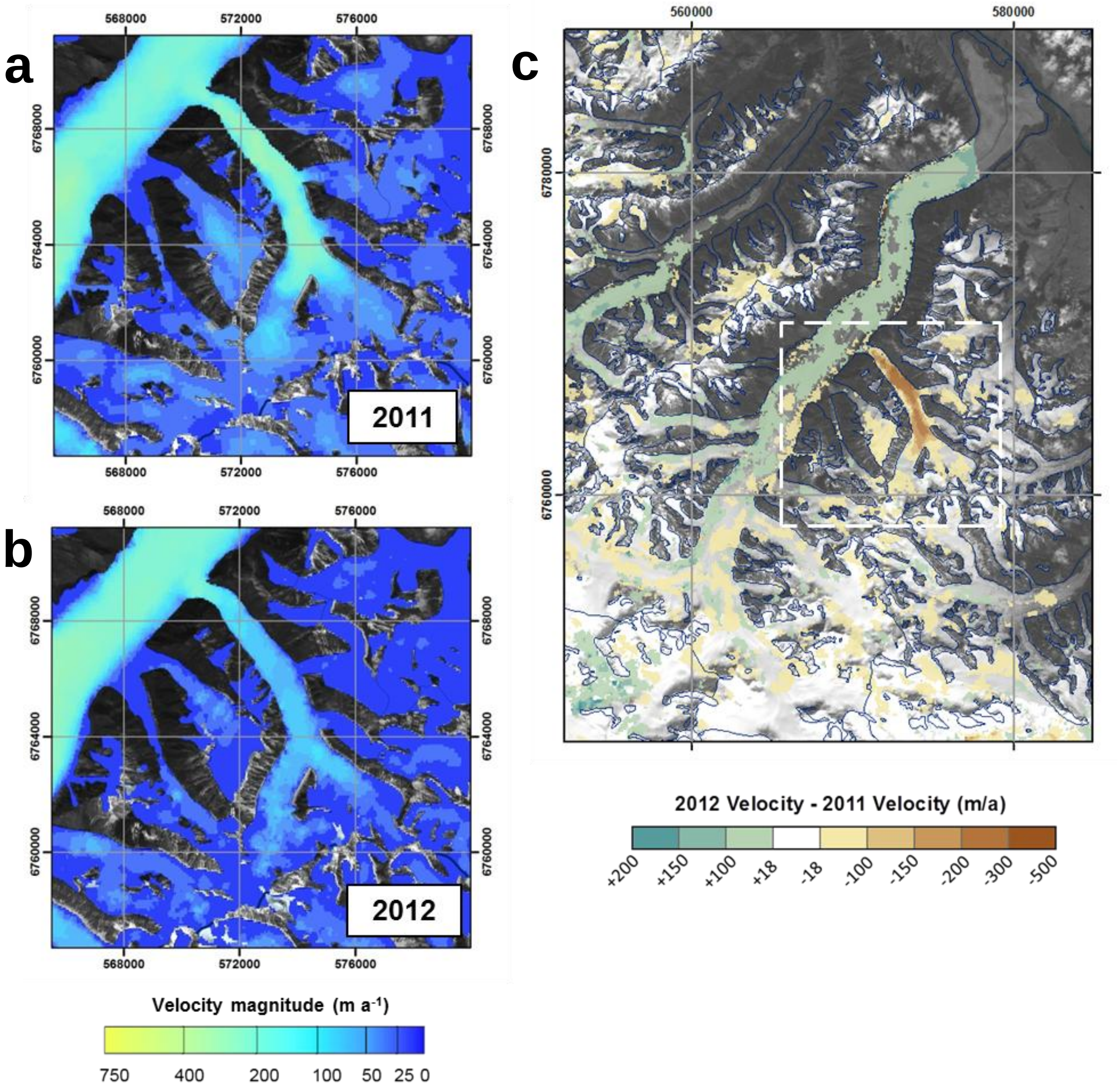

Figure 4.16: (a) and (b) Detail of the southeast tributary of the Donjek Glacier showing the change in velocity from 2011 to 2012. This tributary appears to have been surging in 2011. (c) Magnitude of velocity change from 2011 to 2012 for the Donjek Glacier, including the tributary (inset box) in (a) and (b).

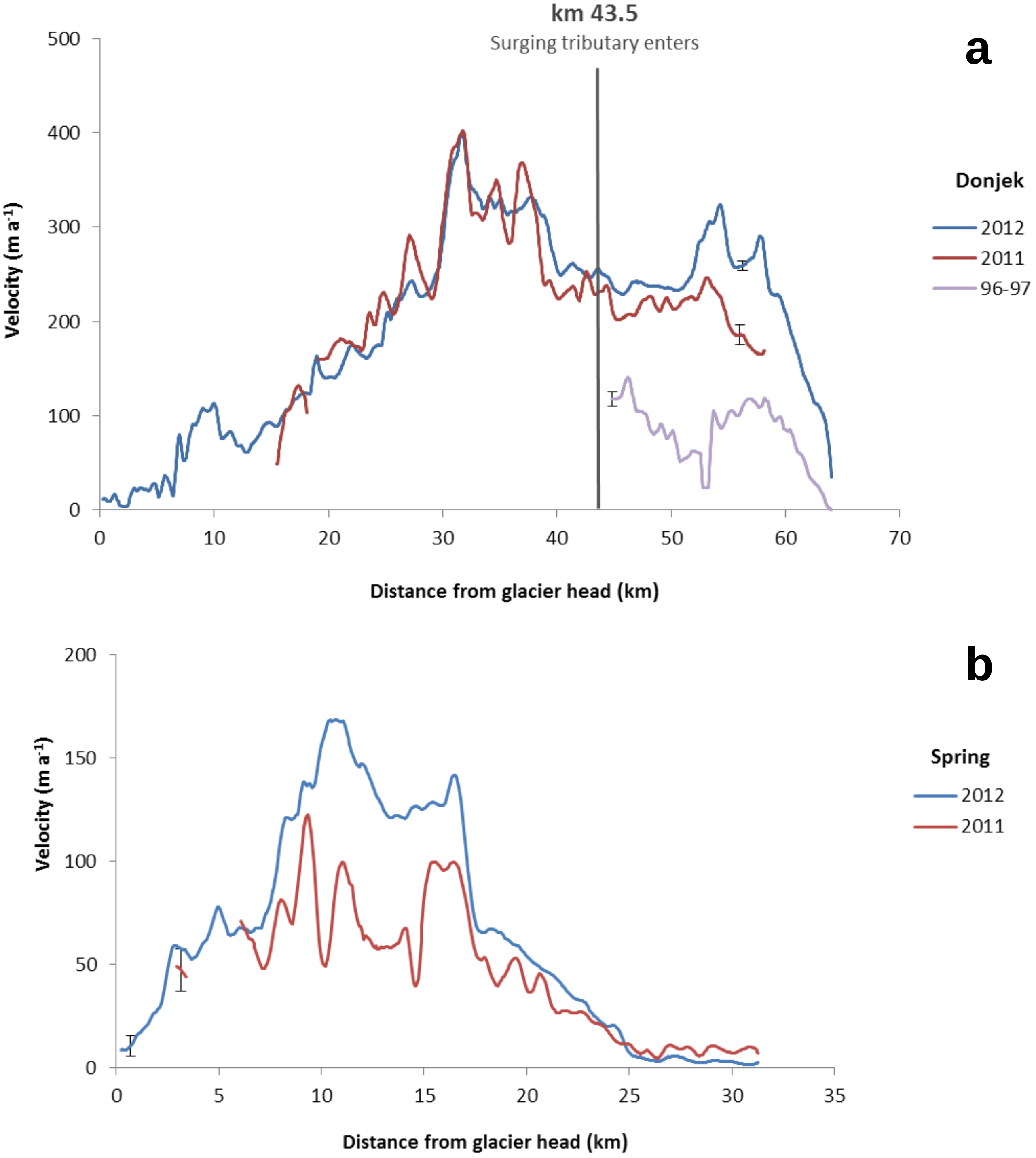

Figure 4.17: Centreline velocity profiles of the Donjek (a) and Spring (b) Glaciers from 2011 and 2012 speckle tracking, and additional 1996-97 feature tracking in the case of Donjek Glacier. Velocities in the lower reaches of Donjek Glacier are significantly higher in the period 2011-2012 compared to the velocities of 1996-97. Ground observations confirm that this glacier was surging during the satellite acquisition period.

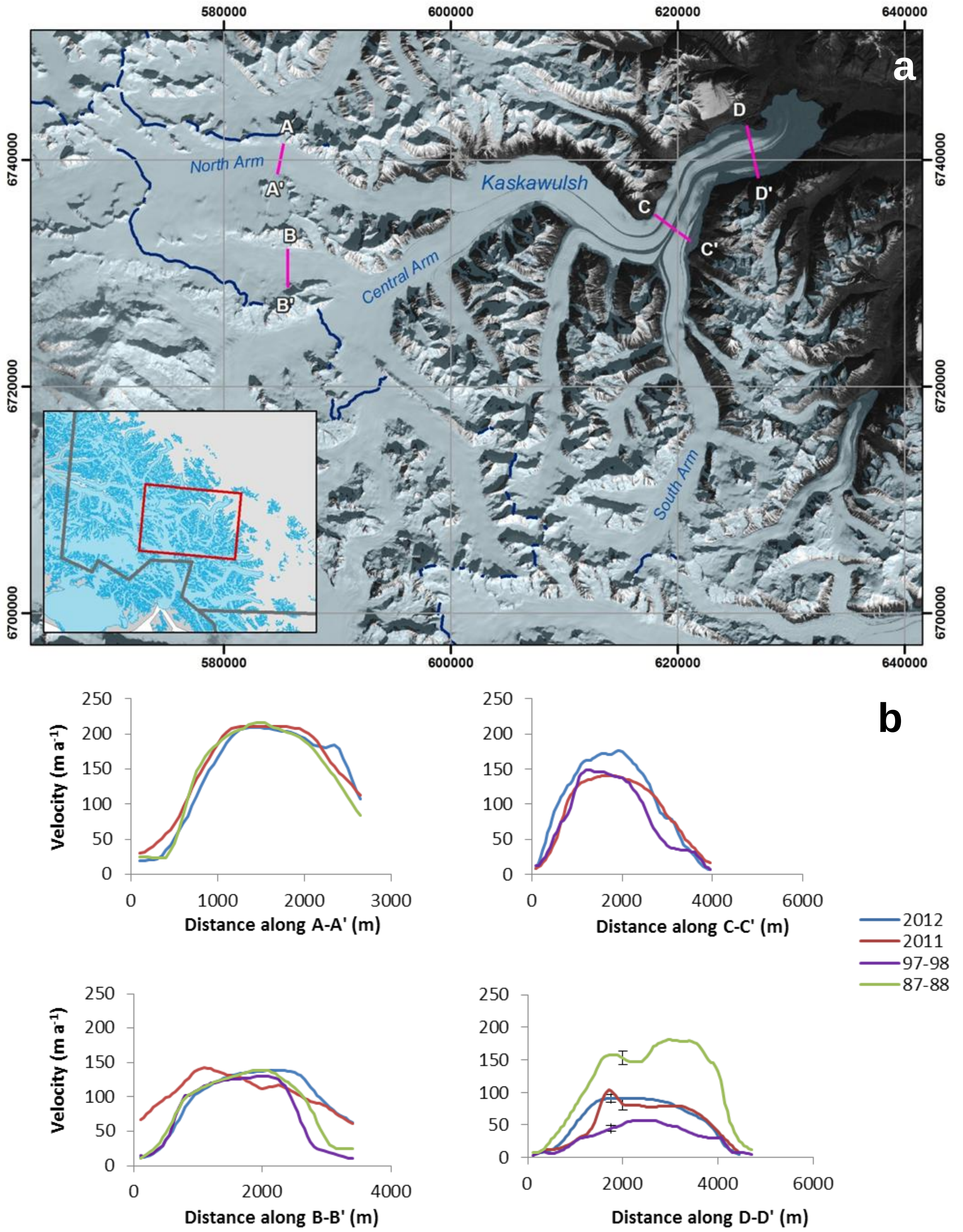

Figure 4.18: (a) Locations of transverse velocity profiles on the Kaskawulsh Glacier, placed where feature tracking was most successful for both Landsat image pairs. Profiles were positioned as much as possible where data points were continuous across the width of the glacier, where filtering and interpolation were minimal. (b) Transverse velocity profiles extracted from the 2011, 2012, 1987-88 and 1997-98 velocity fields at 50 m increments, and averaged over a 250 m moving window.

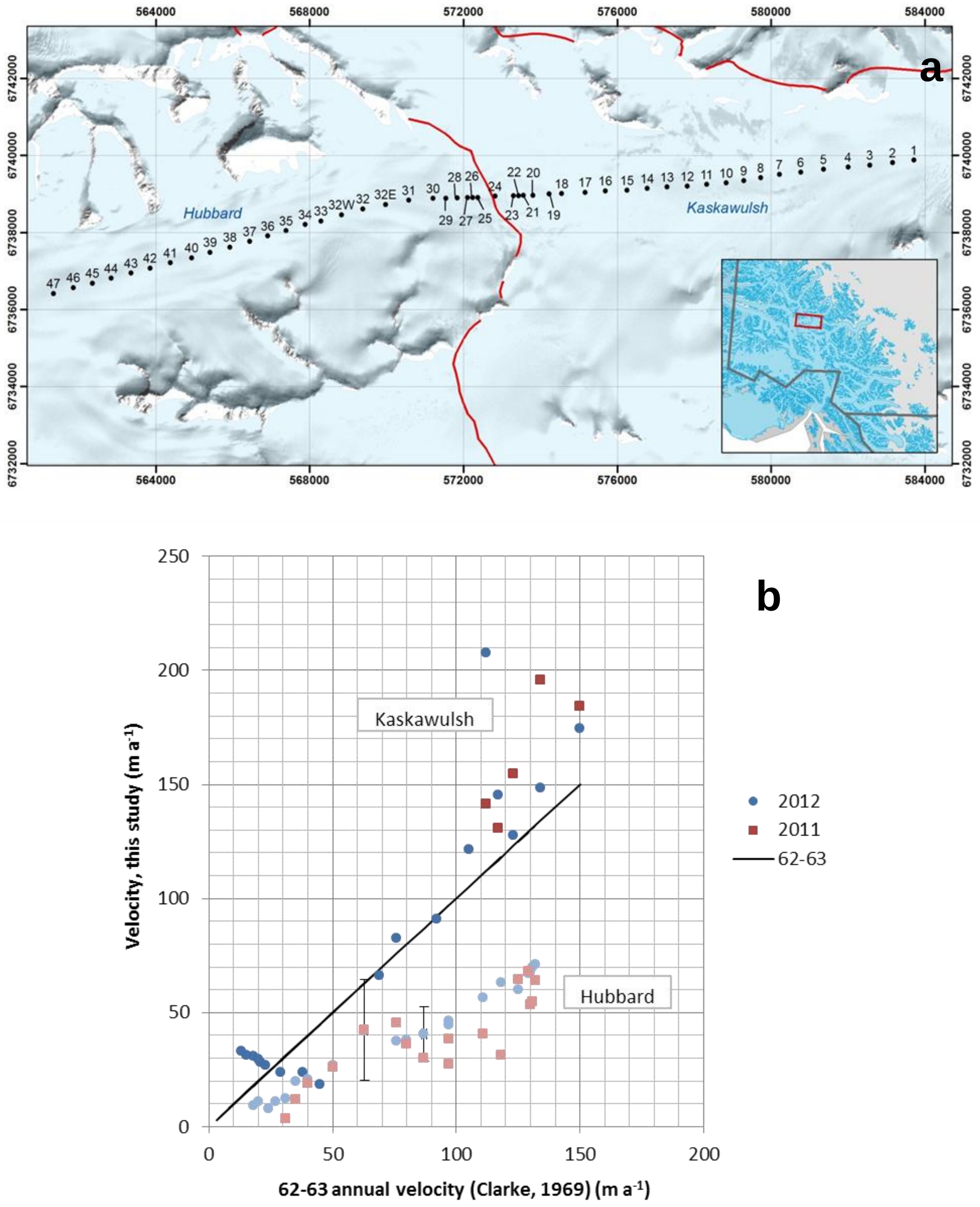

Figure 4.19: (a) Locations of annual velocity stake measurements in Clarke (1969) at which velocities were extracted and plotted in (b). Positions were obtained from georeferencing a scanned image. Positioning error is better than 60 m, or a maximum offset of one pixel in the 2011 and 2012 rasters. (b) 2012 (blue) and 2011 (red) velocities plotted against 1962-63 velocities at the same positions. Points are shaded according to which side of the Divide (located at stake 24) they are on. Darker points are part of the Kaskawulsh Glacier, lighter points part of the Hubbard Glacier.

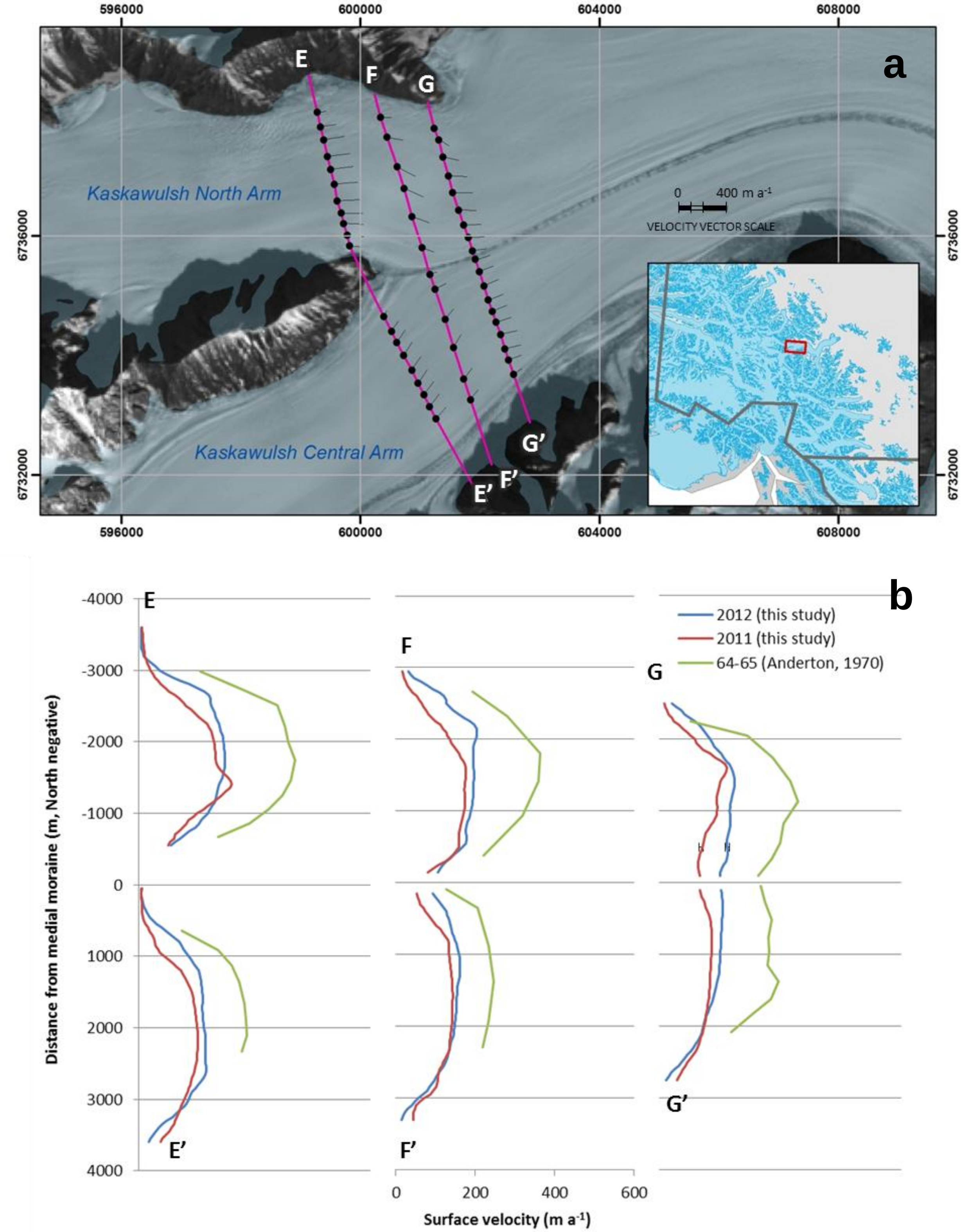

Figure 4.20: (a) Locations of Anderton's (1970) stake array with vectors indicating his 1964-65 annual velocity measurements. (b) Velocity magnitudes along the three lines are plotted by distance. Anderton's 1964-65 point measurements are connected by straight line segments. 2012 and 2011 velocities are extracted at 50 m increments along the profiles drawn in (a), and then plotted as a moving average over a 250 m window. The velocity scale is the same for all three profiles.

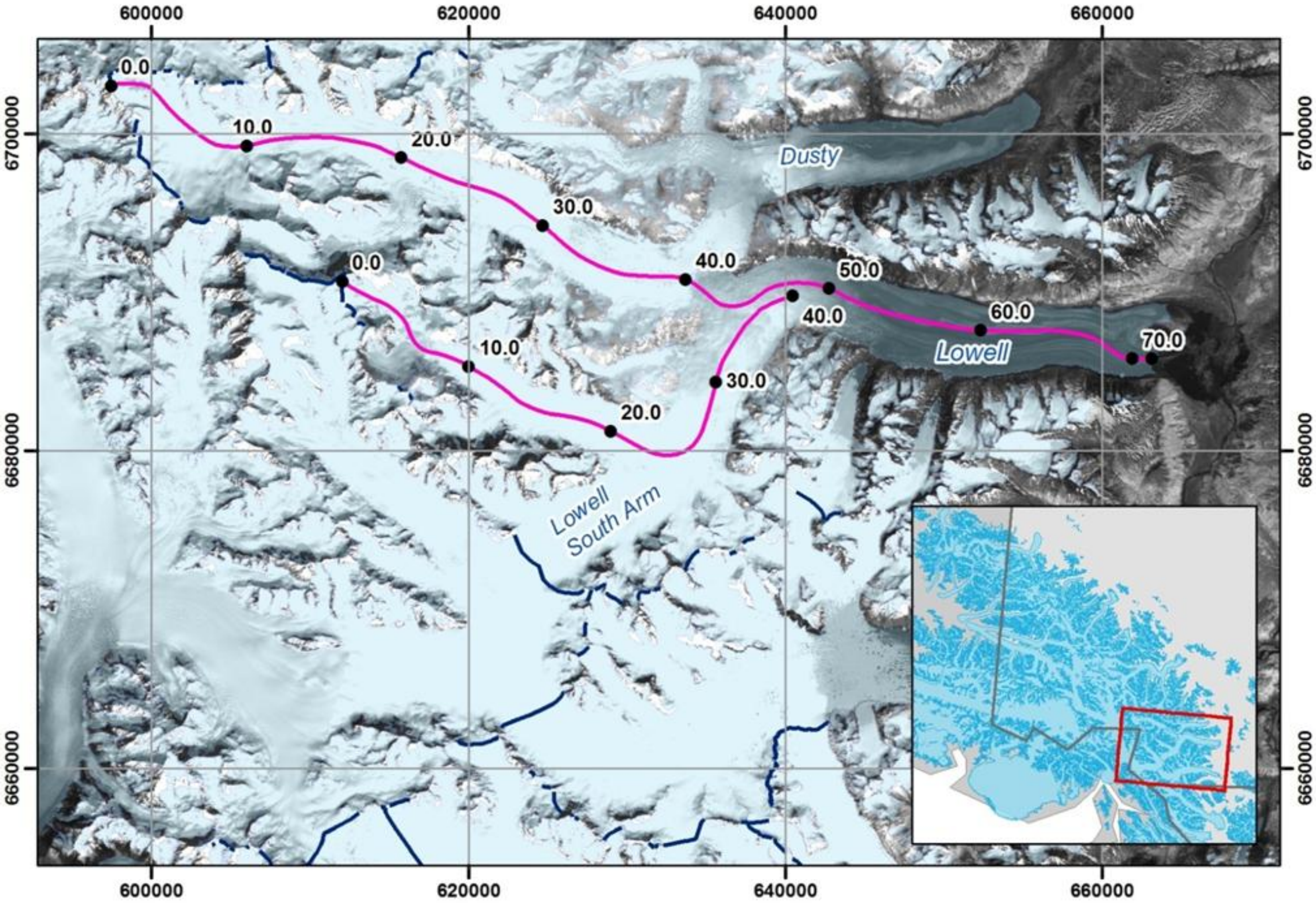

Figure 4.21: Positions of the centrelines along which velocities were extracted to create the longitudinal velocity profiles shown in figure 4.19. Kilometre markings are shown along the profile length. The detailed velocity structure of this area can be found in figure 4.5

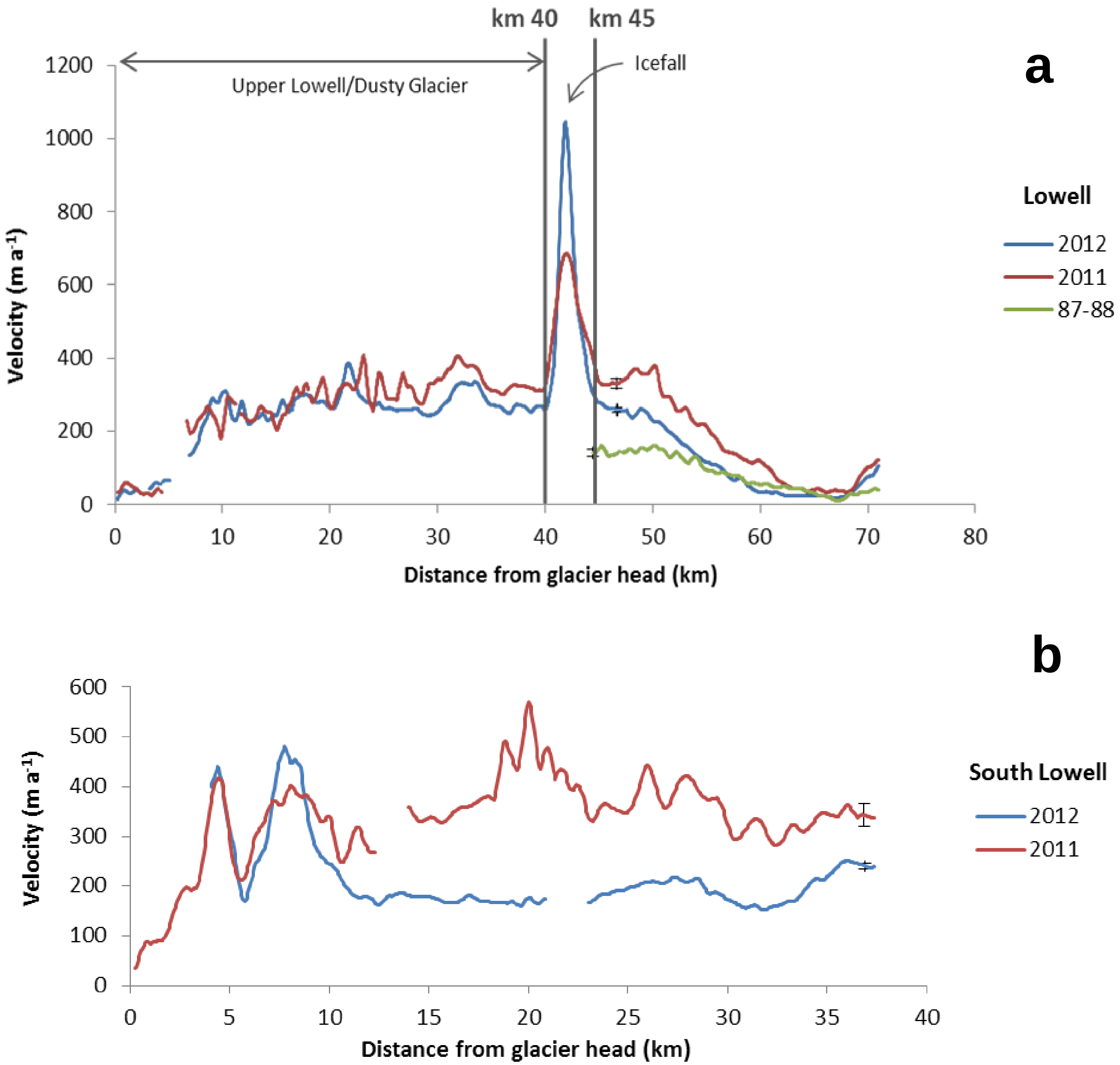

Figure 4.22: Centreline velocity profiles of the Lowell Glacier from 2011 and 2012 speckle tracking, and additional 1987-88 feature tracking of the lower portion of the Lowell Glacier. Profile (a) runs from the Upper Lowell glacier shared with Dusty Glacier through the ice fall to the Lowell terminus. Profile (b) shows the velocities along the southern accumulation area to just east of the confluence with profile (a), as shown in figure 4.18. Velocities were extracted at 50 m increments and plotted as a moving average over a 500 m window. The Lowell Glacier finished surging in 2010. From 2011 to 2012, the glacier is still slowing.

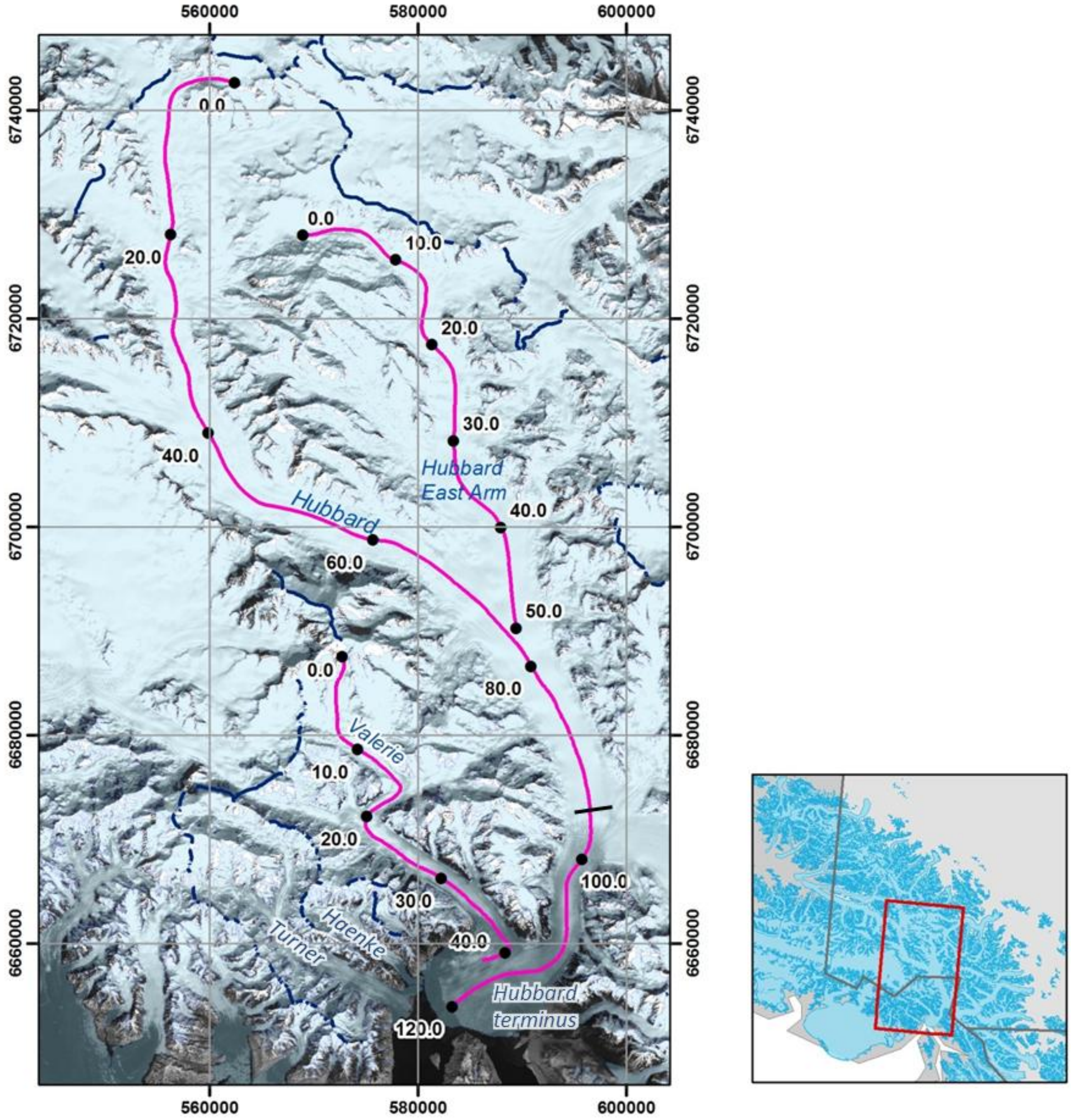

Figure 4.23: Positions of the centrelines along which velocities were extracted to create the longitudinal velocity profiles shown in figure 4.23. Kilometer markings are shown along the profile length.

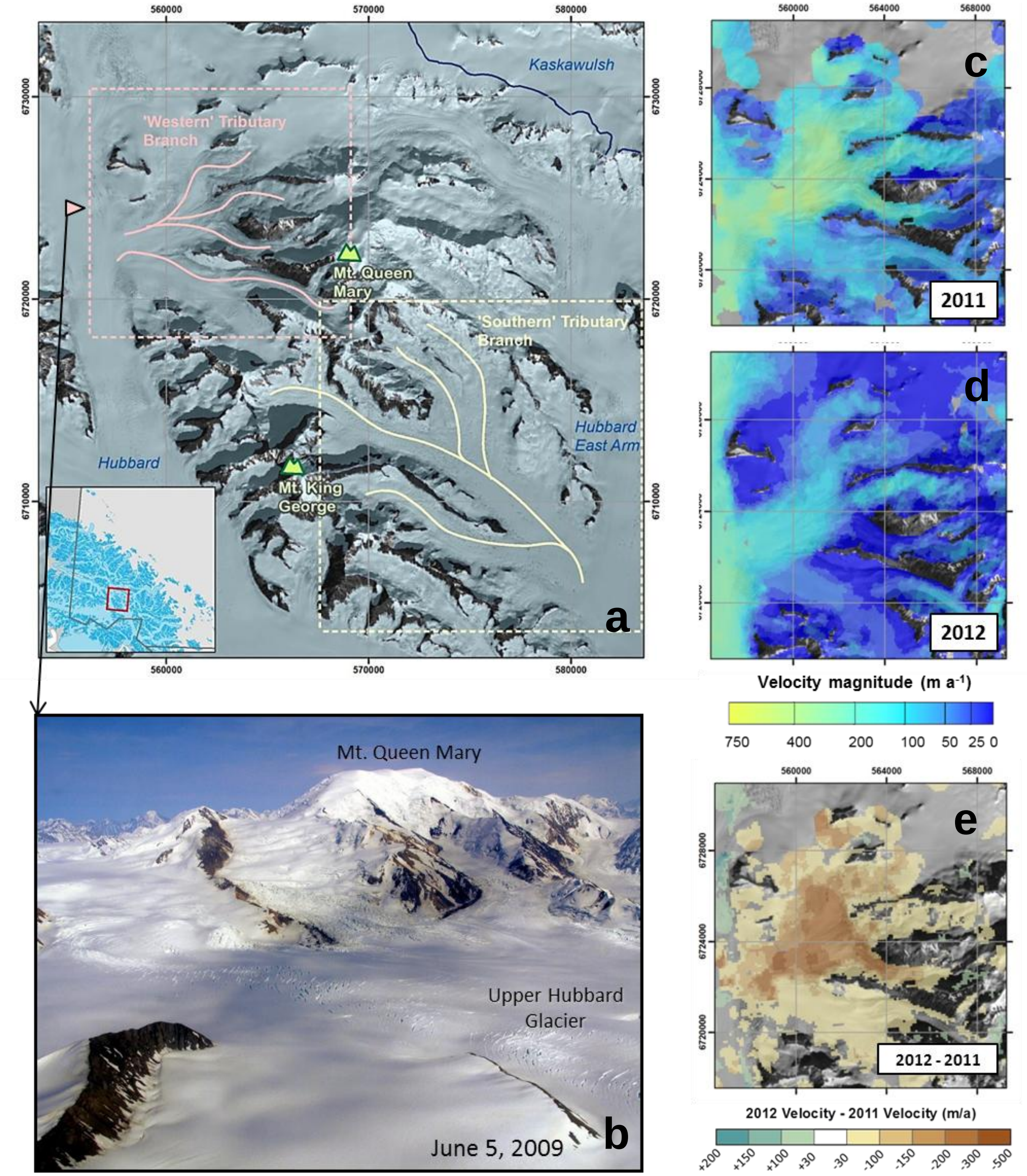

Figure 4.24: (a) Location map showing the position of Mount Queen Mary and the tributary groups flowing from its slopes. The branches labeled are discussed in the text. The western tributary branch is pictured in (b) during a 2009 surge of all three tributaries (photo: Lance Goodwin, Icefield Discovery). The approximate position and look direction of the camera is shown in (a) with a triangle. The 2011 and 2012 velocities of the western tributary branch are shown in (c) and (d), respectively, and the difference between the 2012 and 2011 velocities is shown in (d). A decrease in velocity from 2011 to 2012 is indicated in brown.

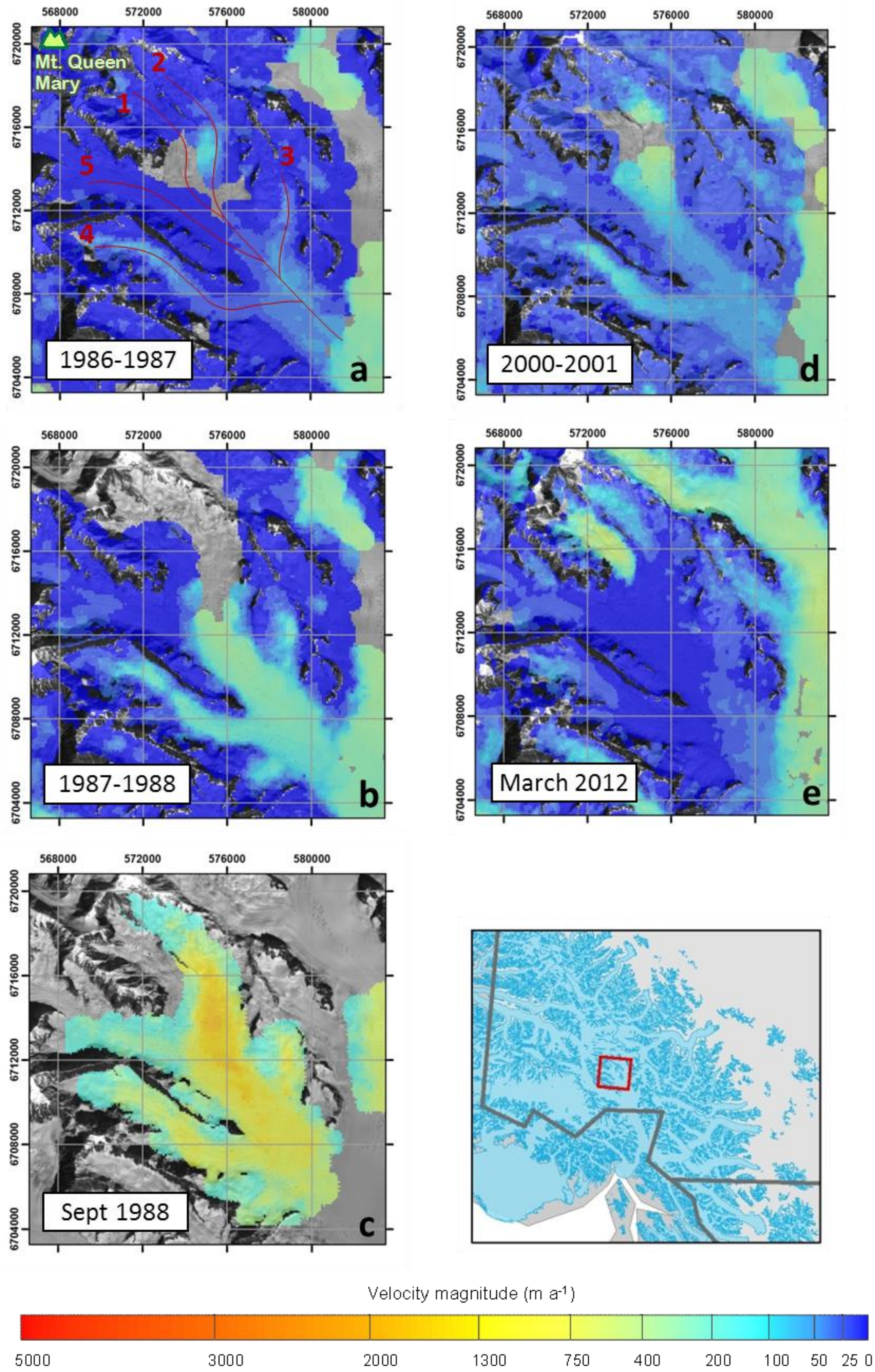

Figure 4.25: Velocity results for the surging ‘Southern’ tributary branch, indicated by the yellow inset box in figure 4.21a, from feature tracking (a: 1986-87, b: 1987-88, c: September 1988, d: 2000-01) and speckle tracking (e: March 2012). Mount Queen Mary is to the top left, and the East Arm of the Hubbard Glacier is on the right in all images. The image sequence captures the progression of a surge from 1986-1988.

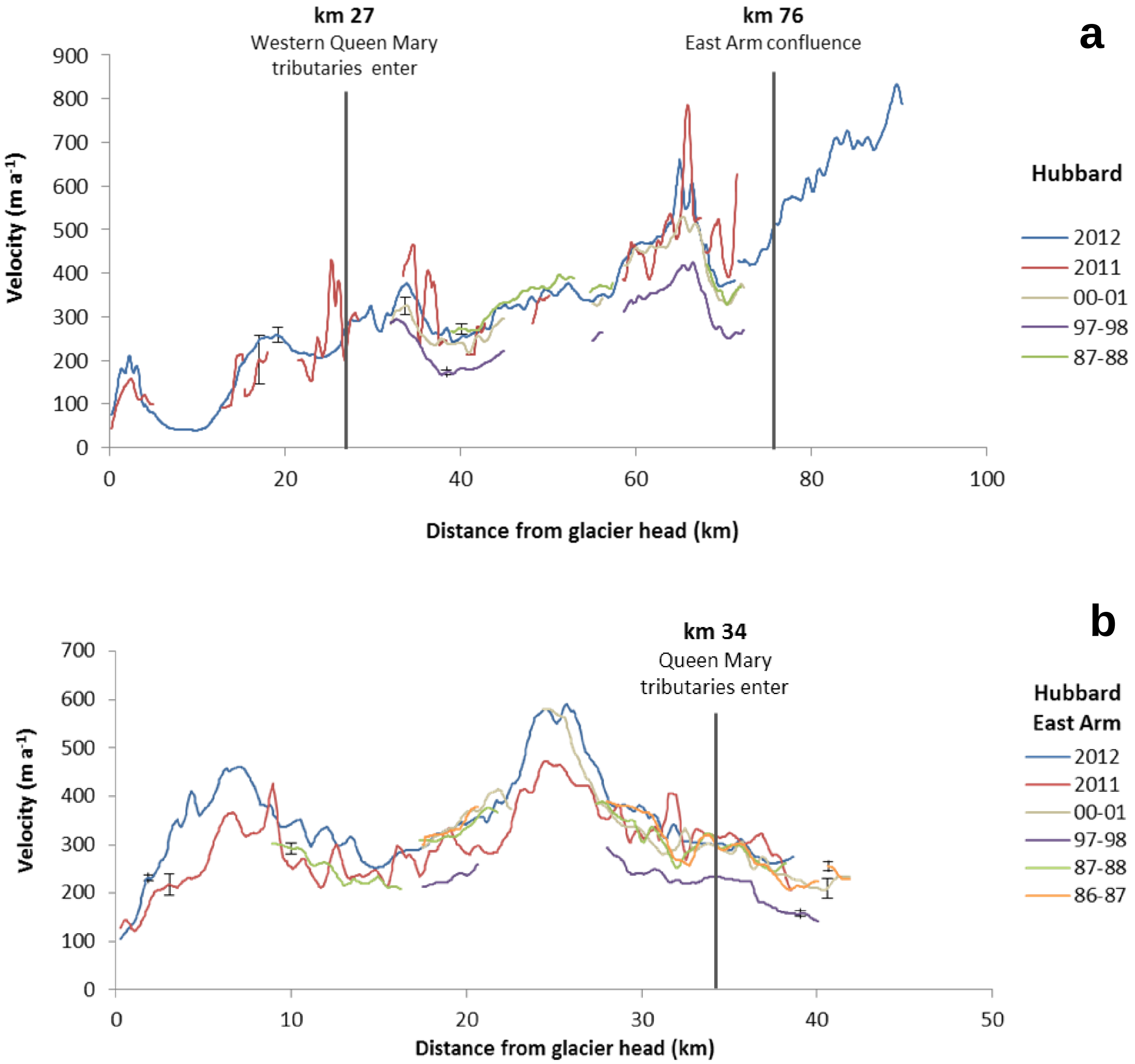

Figure 4.26: Centreline velocity profiles of the Hubbard Glacier (a) from the upper reaches of the West Arm to the mouth of the Hubbard Throat, the narrow valley before the glacier terminus. This profile is continued to the terminus in figure 4.27a. (b) along the East Arm to the confluence with the main West Arm of the glacier. The positions of confluences with the tributary branches described previously are indicated.

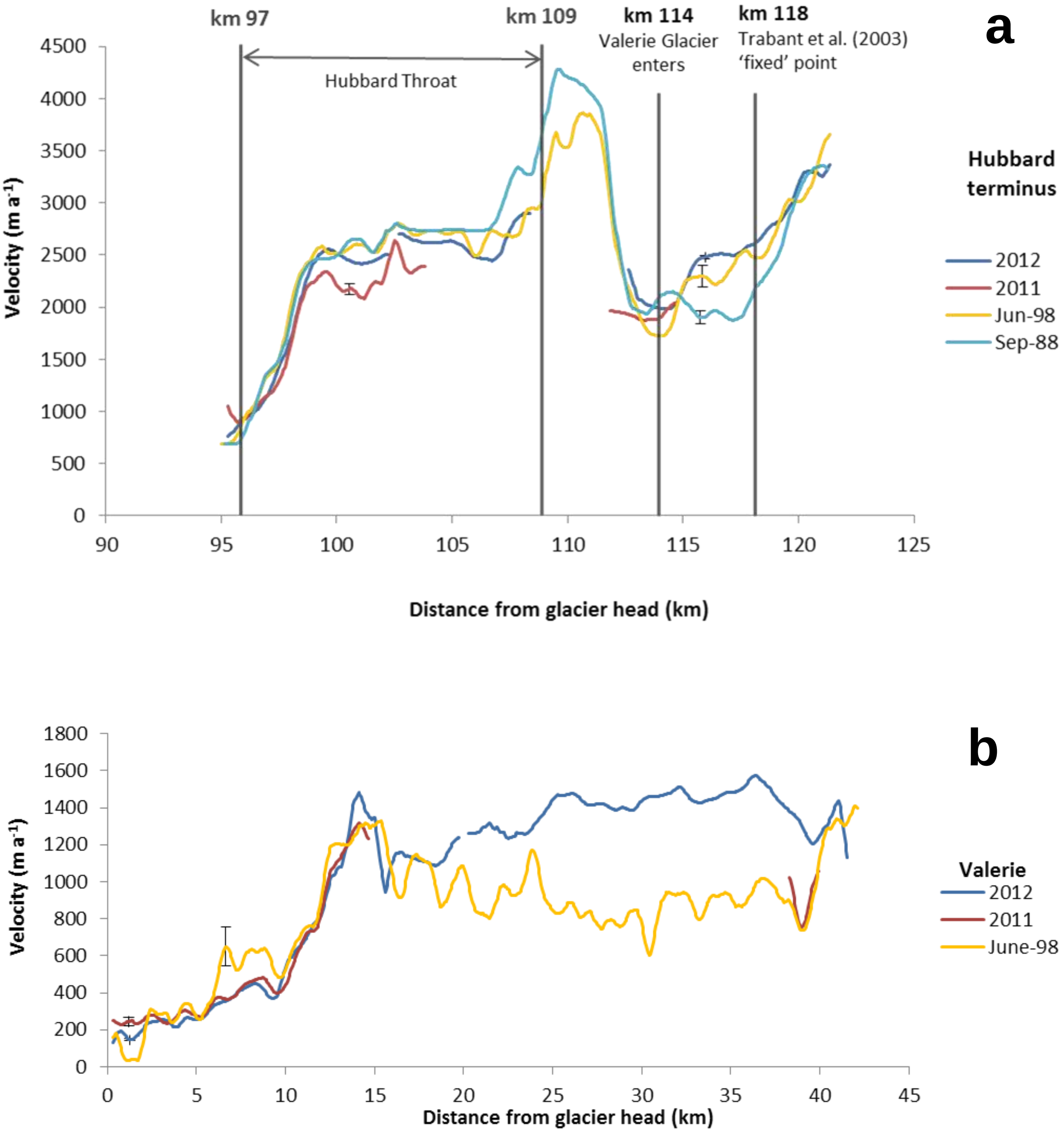

Figure 4.27: (a) Centreline velocity profiles of the Hubbard Glacier from the mouth of the Hubbard Throat to the terminus. This profile is continued from the Hubbard profile in figure 4.26a. (b) Centreline velocity profile of Valerie Glacier.

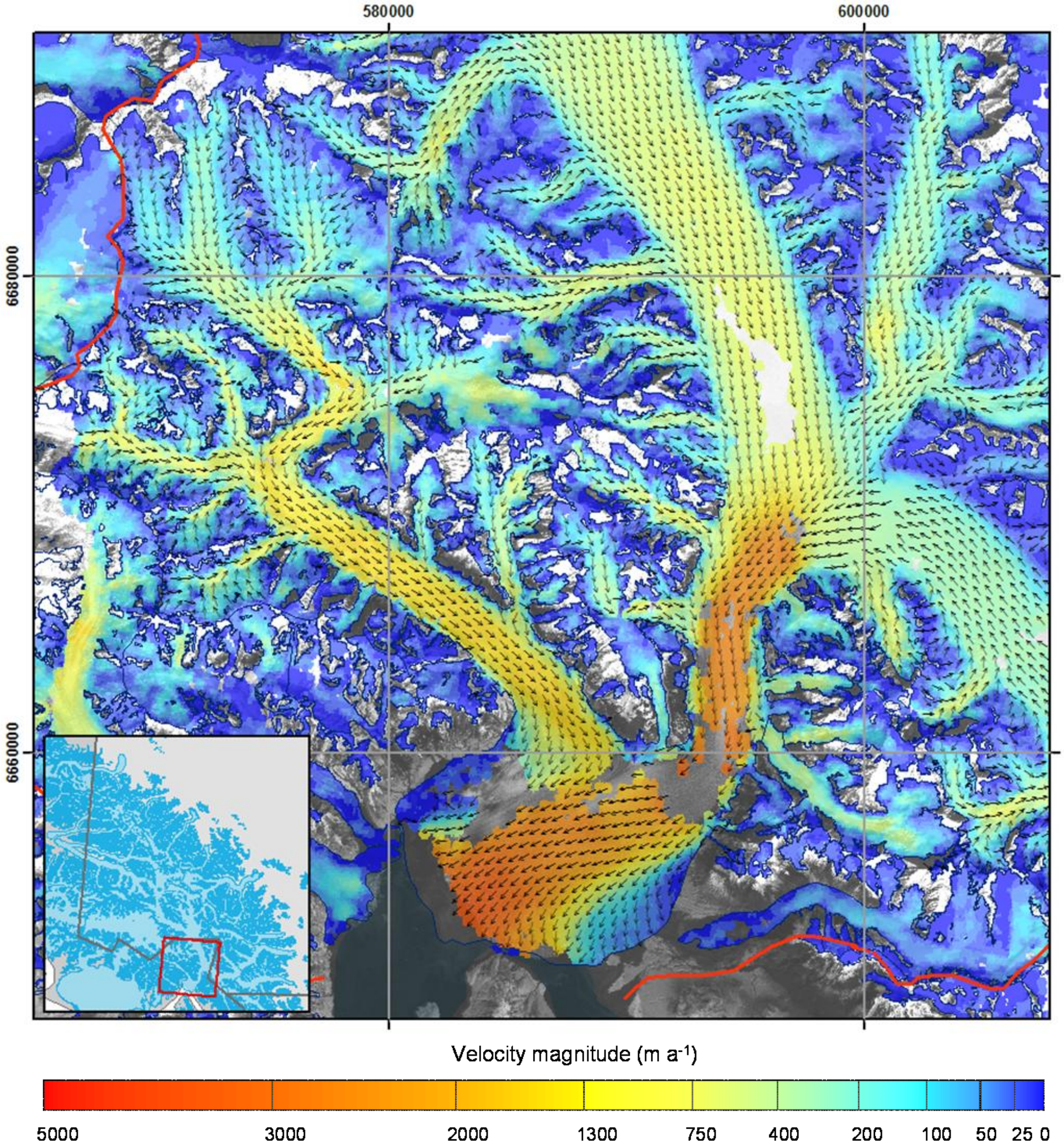

Figure 4.28: Detailed 2012 velocity map of the lower Hubbard Glacier and the Valerie Glacier. The colour scale indicates the magnitude of flow, and vectors show the direction. Vectors have been downsampled to 500 m grid spacing for display.

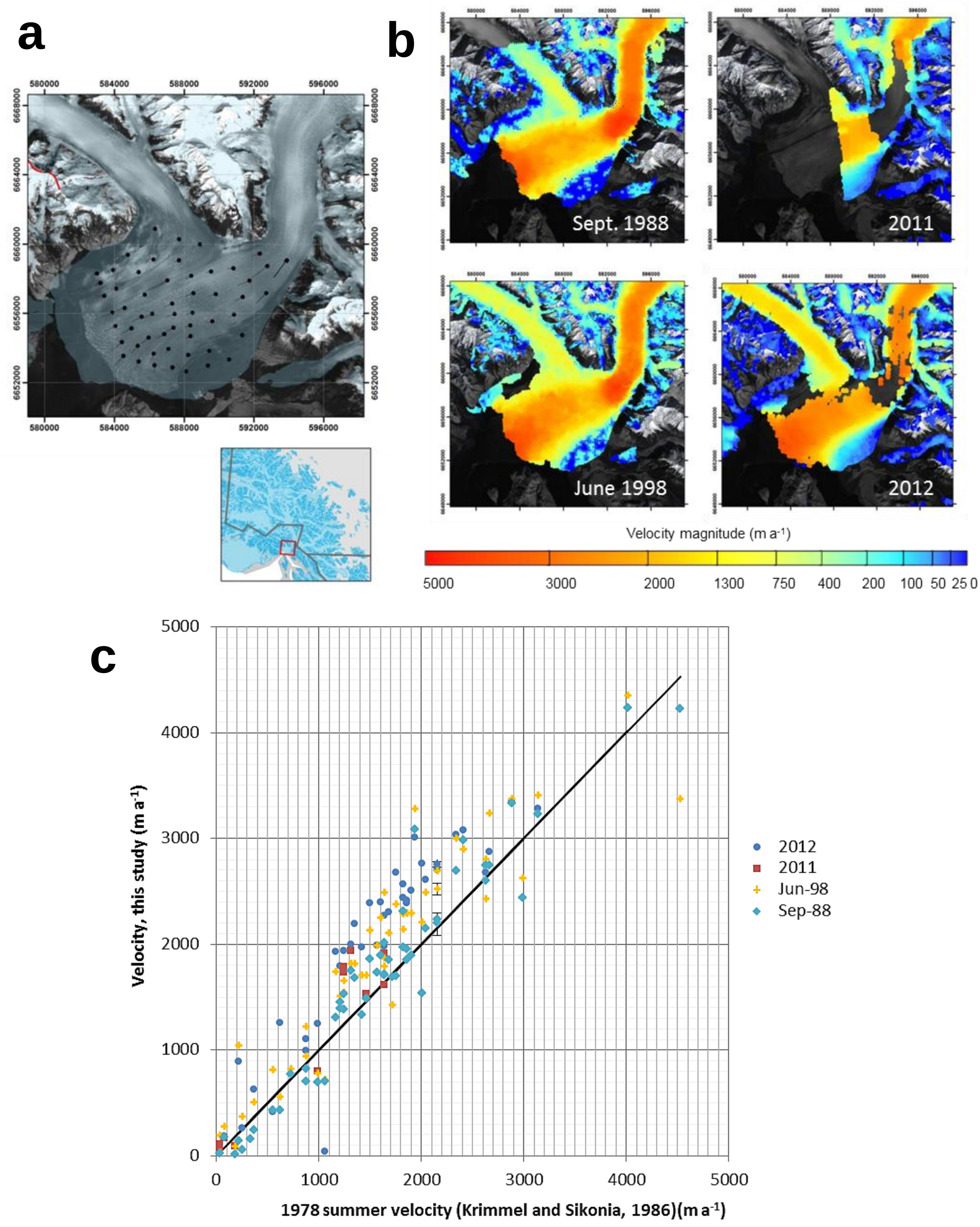

Figure 4.29: Hubbard Glacier terminus activity. Krimmel and Sikonia (1986) installed a stake network over the terminal ~12 km of the Hubbard Glacier, as shown in (a). They measured velocities in August 1978, shown as vectors in (a). (b): Feature tracking (1988, 1998) and speckle tracking (2011, 2012) results over the same area. (c): Velocities were extracted from the rasters in (b) at the stake positions employed by Krimmel and Sikonia (1986) and are plotted against the 1978 velocities.

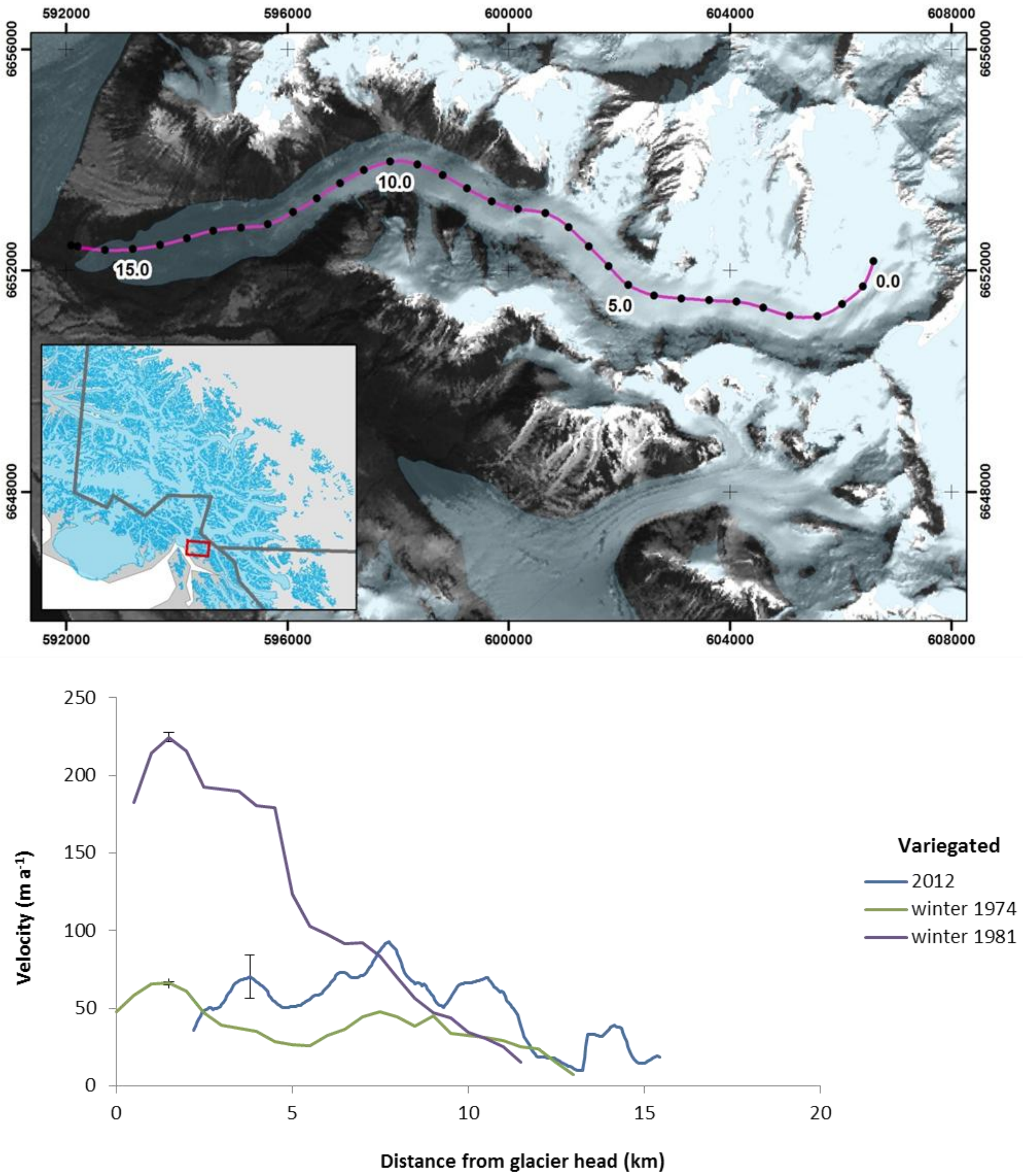

Figure 4.30: (a) Location of the profile used by Raymond and Harrison (1988) to plot the quiescent velocity evolution of Variegated Glacier. (b) Results from Raymond and Harrison (1988) indicating velocity at the beginning of quiescence (1974) and at the end of quiescence (1981). Error bars indicate the measurement error of transcribing velocity values from the published graphs. Velocities were extracted from the 2012 velocity field derived in this study along the same profile, and are plotted against the range of quiescent velocity variability to gauge the surge status of Variegated Glacier in 2012.

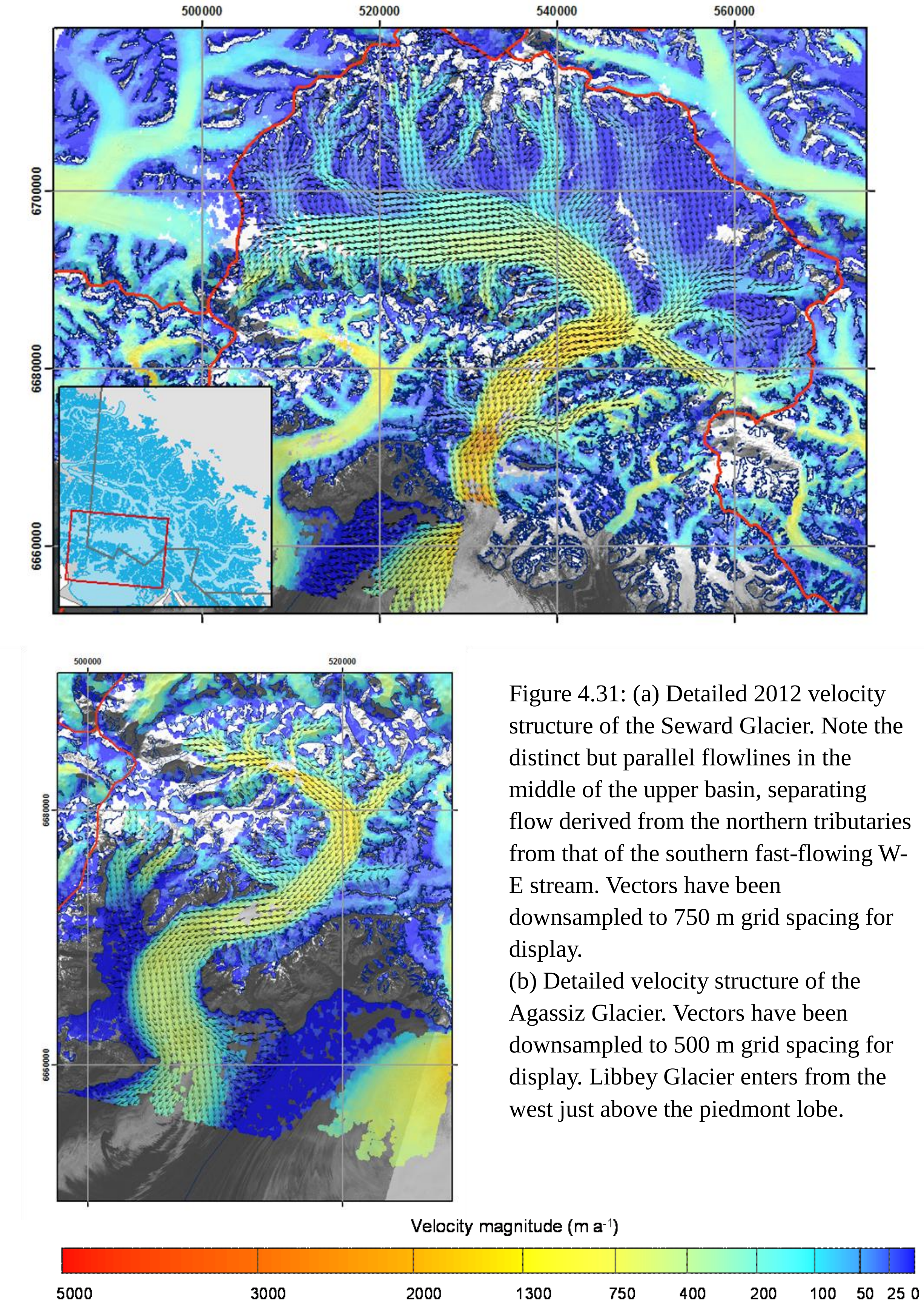

Figure 4.31: (a) Detailed 2012 velocity structure of the Seward Glacier. Note the distinct but parallel flowlines in the middle of the upper basin, separating flow derived from the northern tributaries from that of the southern fast-flowing W-E stream. Vectors have been downsampled to 750 m grid spacing for display.

(b) Detailed velocity structure of the Agassiz Glacier. Vectors have been downsampled to 500 m grid spacing for display. Libbey Glacier enters from the west just above the piedmont lobe.

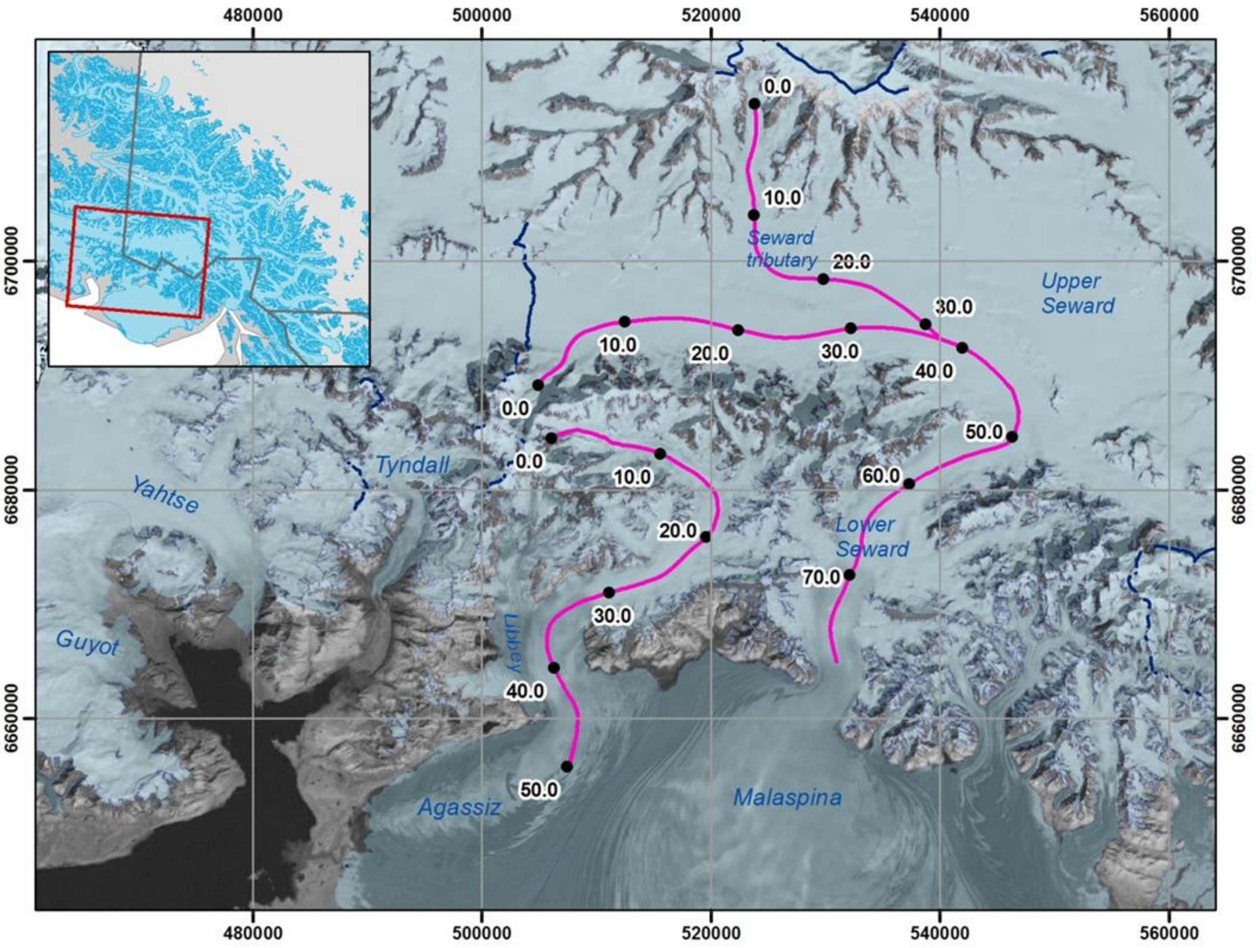

Figure 4.32: Malaspina Glacier system and Icy Bay glaciers showing the positions of centrelines along which velocities were extracted in figures 4.33 and 4.34. Kilometre markings are indicated.

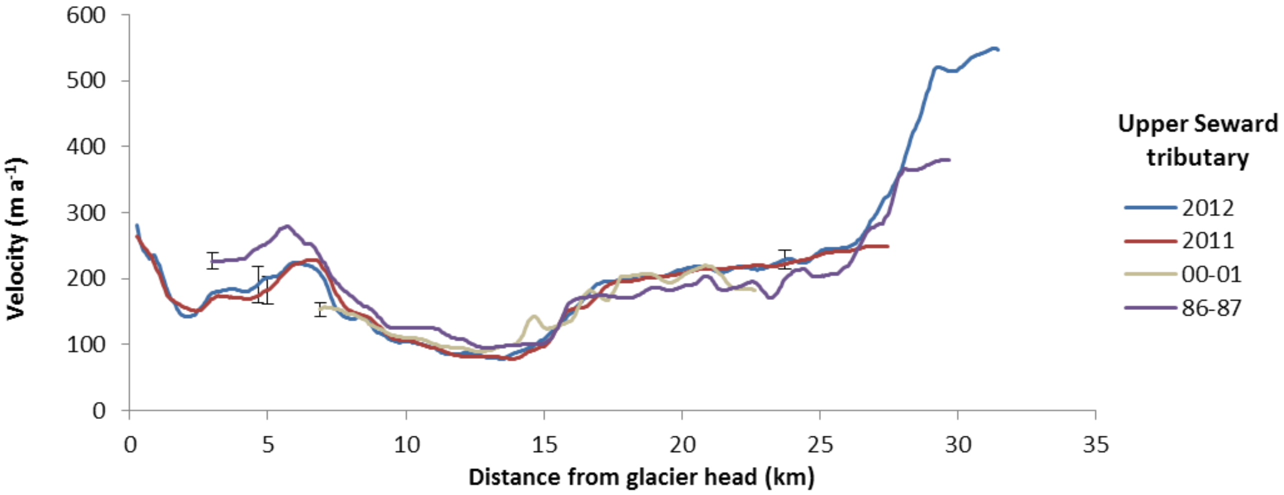

Figure 4.33: Centreline velocity profile of a tributary of the Upper Seward glacier. It was the only location in the Seward basin that had high-quality velocity coverage from both image pairs used in the feature tracking analysis. Velocities are shown from 2011 and 2012 (speckle tracking) and 2000-01 and 1986-87 (feature tracking).

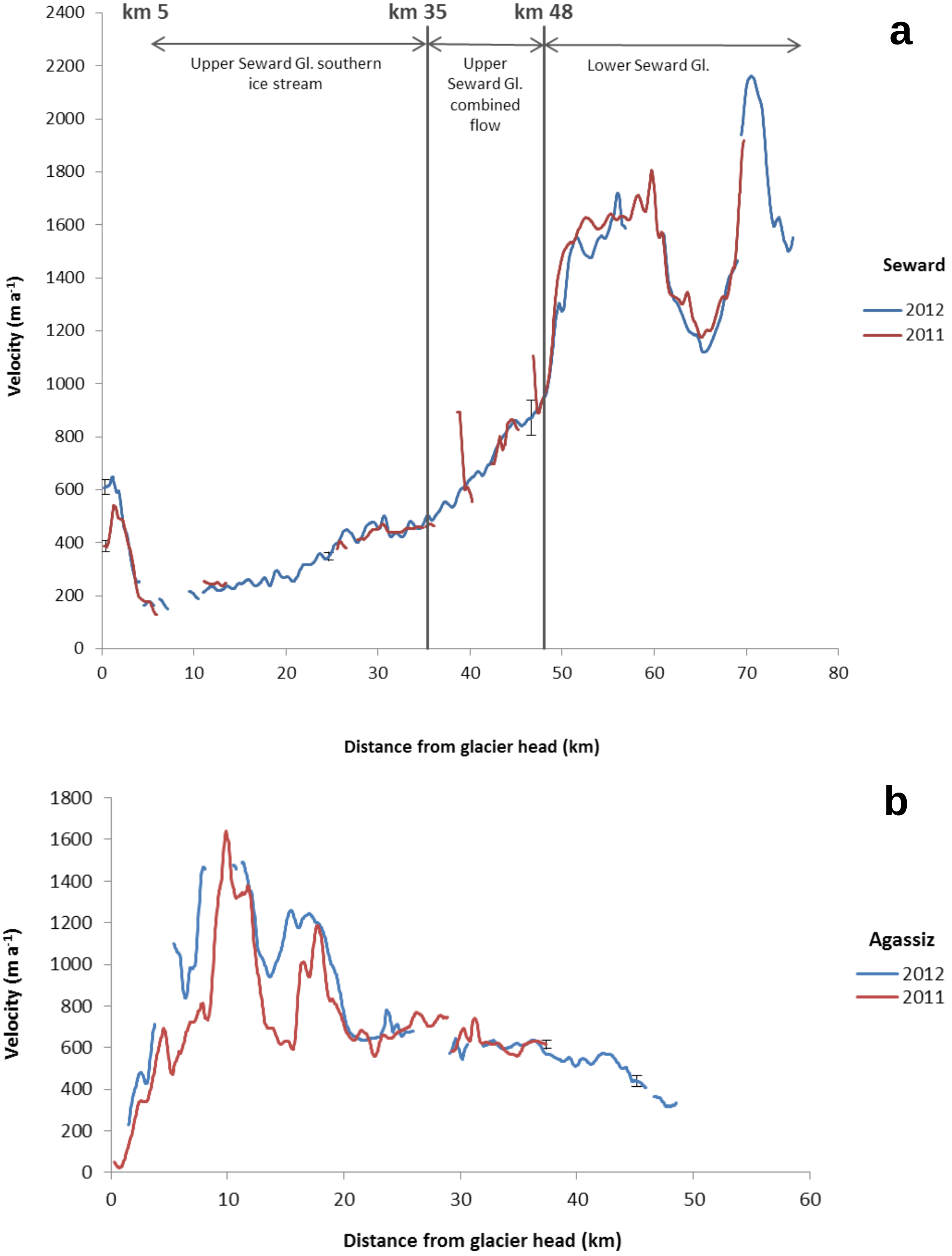

Figure 4.34: (a) Centreline velocity profile of the main Seward Glacier from the Divide with Bering Glacier in the west to the mouth of the Malaspina piedmont lobe as shown in figure 4.29. Velocities were extracted from the 2011 and 2012 velocity fields derived from the speckle tracking analysis. (b) Centreline velocity profile of the Agassiz Glacier, 2011 and 2012.

Chapter 5: Discussion

This study has enabled detailed reconstructions of regional velocities and derivations of past velocities for the St. Elias Icefield. Comparisons between these and previously published literature provides information about annual to decadal variability in glacier motion in the St. Elias Mountains, both in relation to surging and long-term evolution.

5.1 Surge identification and dynamics

Most previous surges in the study region have been identified from morphologic evidence such as rapid terminus advance, observations of increased crevassing, and large displacements of distinctive features between air photos or satellite images (Post, 1966 – Walsh Glacier; Post, 1969 – numerous; Field, 1975 – Anderson, Chitina, Haenke, Disappointment, Felsite Glaciers; Collins, 1972 – Backe Glacier; Driscoll, 1980 – Klutlan Glacier and tributaries; Mayo, 1989 – Valerie Glacier; Clarke and Holdsworth, 2002 – Hodgson, Kluane, Donjek, Dusty Glaciers). This study has enabled an expansion of surge identification from an analysis of complete regional velocity fields (Tables 5.1-5.4). The estimates of surge status given here are based on:

(a) velocity magnitudes and their change from 2011-2012 and over any other period measured. During the surge phase, a minimum tenfold increase in surface velocity is typical. There are also examples in this study where velocities have shown considerable deviation over significant sections of a glacier length between measurement periods. However, without some further evidence such as continuous measurements of the variation between quiescent and active phase velocities, a velocity profile indicative of anomalous fast flow, or coincident ground observations of surge features, there is not enough information to definitively establish the surge status of these glaciers

(b) physical appearance of the glacier surface in the Landsat or Radarsat-2 amplitude images

(c) shape of the longitudinal velocity profile.

(d) velocity of a given glacier in relation to neighbouring glaciers of similar size. It has been noted that surge-type glaciers in their quiescent phase generally flow much more slowly along most of their length than other glaciers of a similar size (e.g., Tweedsmuir Glacier in 2011/2012; Figure 4.5, 4.6).

(e) In terms of the longitudinal profile of surge-type glaciers in quiescence, one tends to see glaciers with extensive areas of inactive ice at the terminus (e.g., profiles of the Walsh (Figure 4.10), Steele (Figure 4.5, 4.6), and Klutlan (Figure 4.13) Glaciers). During the active phase, there is usually some form of reactivation of this ice, in the form of an expansion of the area of fast flow. The profile may evolve from a velocity peak in the upper glacier with a long stagnant tail to the terminus, to a pattern of increasing flow with distance downglacier followed by an abrupt asymmetric decrease (as in the Logan Glacier profile).

In total, 6 tributary surges were observed in 2011 and 2012 (2 Mount Wood tributaries, SE tributary of the Donjek Glacier, Mount Queen Mary western and southern tributary branches, and the Libbey Glacier), with two of these appearing to have terminated by winter 2012 (eastern Mount Wood tributary, western tributary branch of the Mount Queen Mary tributaries). In addition the southern Mount Queen Mary tributary branch was observed to be surging in 1986-88, and possibly 2000-01 as well. Surges were observed at three trunk glaciers: the Hazard, Donjek and Logan Glaciers.

Surge classification of glaciers is further complicated by fact that velocity evolves through quiescence, and that this evolution may represent doubling or trebling of surface velocities over the quiescent period, with a doubling of velocity possible from one year to the next (Raymond and Harrison, 1988). The only measurements of the quiescent phase velocity evolution of a surge-type glacier over an entire quiescent period are from Variegated Glacier (Raymond and Harrison, 1988). While these are of excellent detail, it is unknown if the rate of change of velocity measured at Variegated Glacier is applicable to glaciers of other sizes. In other words, is the manner of the quiescent velocity evolution likely to be highly variable between different glaciers? This question can be partially addressed with the results of the 2011 and 2012 velocity studies. Of twelve glaciers either in the quiescent phase or where the surge status is uncertain, six show significant increases in the peak velocity from 2011 to 2012. The magnitude of the increase ranges from 16 m a^{-1} (13% of 2011 velocity) to 194 m a^{-1} (62% of 2011 velocity). Three glaciers show velocity increases of less than 30 m a^{-1} (less than 15%), and three glaciers show velocity increases of greater than 50 m a^{-1} (greater than 30%). This would imply that the quiescent velocity evolution of different glaciers is highly variable. However, the rate of increase of velocity during quiescence at Variegated Glacier was not consistent over the 9-year period, so without knowing the precise stage in the surge cycle of these glaciers, it is not possible to definitively conclude as such. Further annual velocity measurements would clarify this point.

Repeat velocity surveys would be of great use in constraining details of the velocity evolution of surging glaciers during both quiescent and active phases, and in determining the degree of interannual velocity variability on those glaciers not commonly considered surge-type. Regional flux estimates for Alaska and the Yukon Territory are still associated with large errors, primarily from the lack of ice thickness measurements, but also because there is not enough information to characterize the year-to-year variability in velocity. The Hubbard Glacier (including the tributary Valerie Glacier) carries an estimated 16.6% of the ice flux out of the Gulf of Alaska mountain ranges (Burgess et al., 2013). Within this system, the Valerie Glacier surges, but also appears to experience velocity variability of 600 m a^{-1}.

The results of this study at the Lowell Glacier illustrate how repeat velocity surveys can add to our knowledge of the progression of a surge, including the manner in which different tributaries or parts of the glacier contribute to the surge and how velocities evolve during a surge. These measurements suggest that both the northern and southern arms participate in surges of the Lowell Glacier, but that the southern arm is dominant as it experienced the greatest decrease in motion between 2011 and 2012. The behaviour of the terminal 12 km in 2011 and 2012 is also appreciably different from the 1987-88 quiescent baseline. The quiescent velocities show a steady deceleration towards the terminus, while in 2011 and 2012 the velocities show a much sharper decrease followed by an increase very close to the calving front. This is consistent with the typical velocity pattern of a calving glacier where there is less backstress at the glacier terminus. It is likely that during quiescence, the terminus ice is grounded and thick enough to have a minimal impact on the terminus dynamics. In comparison, terminus advance during surging extends and thins the glacier and increases crevassing, which increases the calving rate and can facilitate acceleration of the lowermost part of the glacier.

At the Logan Glacier, the results of this study combined with the velocity map produced by Burgess et al. (2013) from winter imagery sometime between 2007 and 2010 show a slow buildup of velocity over the main trunk of the glacier with velocities high enough compared with the 1986-99 baseline to indicate surging over at least three years. During that time, the peak velocity has further increased by about 200 m a^{-1} (approximately doubling), and the location of the peak velocity seems to be propagating downglacier. The shape of the profile is remarkably consistent from year to year, and the variability along its length is quite small. The surge followed a period of mass loss in the lower glacier and significant thickening (> 3 m a^{-1}) in the middle glacier, as shown in repeat altimetry measurements in 2003 and 2007 (Arendt et al., 2008). The peak velocity thus far measured is an order of magnitude lower than the displacements of several thousand metres over 2 years measured during the 1960 surge of Walsh Glacier in the neighbouring valley. It seems that surges of the Logan Glacier may be less dramatic than those of the Walsh Glacier. It may explain the relative lack of distorted surface features used elsewhere in this region to identify surge-type glaciers.

5.2 Long-term velocity change

The velocity change measured between 2011 and 2012 and other past periods can represent a combination of a number of signals, namely seasonal variations, variations related to surge dynamics, variations related to other interannual dynamics, and long-term trends in the velocity structure as a result of climate variations. Concerning seasonal variations, the ideal case would be to have image pairs separated by exactly one year so that there are no assumptions made in scaling to annual velocities. In the absence of this, the winter velocities provided by speckle tracking of SAR imagery are advantageous because they are more stable for interannual comparison, as summer velocities are often characterized by large variability over periods of days to weeks due to variable meltwater inputs and changes in subglacial hydrology (Iken et al., 1983; Short and Gray, 2005; Darling, 2012). They represent conservative estimates of annual glacier flow rates, although numerous seasonal velocity studies on temperate glaciers have shown that minimum velocities occur in early fall, when drainage is at its most efficient and meltwater inputs are decreasing (Black Rapids Glacier, Alaska – Rabus and Fatland, 2000; Himalaya – Scherler et al., 2008; Kaskawulsh Glacier – Darling, 2012; Hubbard Glacier – Trabant et al., 2003). This fall minimum may balance to a certain extent the acceleration early in the season. During the winter season, the drainage system reorganizes to a less efficient mode and velocities stabilize at a rate that is generally intermediate, and this, in conjunction with the longer duration of a winter velocity regime, means that annual velocities derived from winter displacements may be relatively close to true annual displacements.

There are few glaciers in this region that permit of examination of long-term velocity evolution given the dataset available, since the interannual surge activity-related signal overwhelms any more subtle decadal-scale change. However, there are two main glaciers in the region whose trunks are not surge-type: the Hubbard and Kaskawulsh Glaciers. Comparing the velocity data over the different measurement periods derived in this study, it becomes clear that the interannual variability of these two glaciers seems to be considerably less relative to their magnitude of flow than that of other, surge-type, glaciers in the region, even those that are probably in quiescence over the measurement period.

Hubbard Glacier

Given the dominance of the Hubbard Glacier in regional ice fluxes, it is useful to assess how the measurements presented in this study can be used to understand its velocity variability. The Hubbard system includes numerous surge-type tributaries, both near the terminus as in the case of 'Seattle' Glacier, and higher in the accumulation zone. As in the case of both branches of Mount Queen Mary tributaries examined in this study, surges of these glaciers may periodically reactivate branches of the Hubbard Glacier, and the effect of such changes on the Hubbard ice flux is uncertain.

This analysis has provided some evidence to suggest that surges of these tributaries do not have a large impact on the Hubbard trunk velocity. In particular, the large decrease in velocity from 2011 to 2012 at the western Mount Queen Mary tributary branch does not extend into the West Arm. However, it should be noted that the 2011 results for much of the length of the Hubbard West Arm are patchy and less reliable than the 2012 results. It is possible that the actual difference was greater than observed. The comparison at the Kaskawulsh-Hubbard Divide between measurements of velocity made in 1964-65 and 2011/2012 shows a decrease by a factor of 2 in the velocity of the upper Hubbard Glacier, at a position about 10 km upstream from the western Mount Queen Mary tributaries. On the Kaskawulsh side of the Divide, velocities were largely unchanged and may even have slightly increased, which is consistent with regional observations of zero mass loss or thickening in the upper accumulation areas of the St. Elias Icefields (Arendt et al., 2008; Foy et al., 2011). The large decrease in velocity on the Hubbard side of the Divide is unexpected, and may be related to surge activity of its upper tributaries. A more detailed picture of the velocity evolution of the upper Hubbard Glacier and its surging tributaries would be required to clarify this point.

The Hubbard Glacier has been advancing over the entire measurement period, and is projected to continue to advance well into the coming future, despite the regional mass loss trend. Its AAR (accumulation area ratio) is 0.95, and the equilibrium line is currently located at a relatively steep part of the glacier. In the case of upward migration of the ELA, the area affected in the near future will be quite small, and it is estimated that the ELA would have to retreat 1000 m upward for the Hubbard Glacier to attain an AAR of 0.7 (when retreat might be expected to begin) (Trabant et al., 2003). It currently has a positive mass balance and shows thickening along most of its length (Arendt et al., 2008).

Results of this study at the terminus of the Hubbard Glacier indicated an increase in velocity in the central portion of the terminus over the period 1978 to 2012. This is in contradiction to the results of Trabant et al. (2003), who found an overall decrease in the velocity of the Hubbard Glacier over the period 1974 to 1997 at a fixed point approximately 3 km from the terminus and a similar decrease at the ice wall over the period 1948 to 2001. Admittedly, their trends were drawn from very sparse datasets. Velocities extracted from the 1988, 1998 and 2012 results of this study at the same fixed point used in Trabant et al. (2003) show no significant change from 1988 to 1998, and an increase of several hundred m a^{-1} from 1998 to 2012 when velocities were ~2650 m a^{-1}, or 7.26 m d^{-1}. Extrapolating the trend of Trabant et al. (2003) to 2012 would give an expected velocity on the order of 5.2 m d^{-1}. The range of their dataset was from 7.7 m d^{-1} to 6.0 m d^{-1}. While both Trabant et al. (2003) and this study compared winter velocities at the km 3 fixed point, there is a small discrepancy that arises because compared with Trabant et al. (2003) (who restricted themselves to winter velocities averaged over at least nine months of displacement), the speckle tracking measurements are much more punctual. It is possible that the higher 2012 velocities could be accounted for by larger inputs from a faster-flowing Valerie Glacier.

The difference between the 1988 and 1998 results may be due to seasonal differences, as Trabant et al. (2003) noted that maximum velocities were generally found in May and June while minimum velocities were measured at the end of fall, generally between September and November. In this case the 1998 (June) measurements would be expected to be significantly higher than the 1988 (September) measurements. It is perhaps worth noting that the difference measured between these two years was far less than the 2 m d^{-1} seasonal variability expected for the terminus of the Hubbard Glacier (Trabant et al., 2003). Both values would be expected to be higher than the winter velocities in the time series of Trabant et al. (2003).

Under an advancing regime, thickening of the terminal area is expected to lead to velocity decreases, as shear stress is reduced. It is similar to the seasonal pattern of variation in velocity noted at other calving glaciers, where, close to the terminus, initial acceleration as a result of the spring breakup of adjacent sea ice thins the glacier tongue leading to further acceleration. Thinning and acceleration continue until melt ceases in winter and the calving front begins to advance. Ice flow in the interior may still be greater, and so the terminus is thickened which reduces the velocity to its seasonal low (Joughin et al., 2008). However, the Hubbard Glacier is projected to experience both increased accumulation and increased ablation as the climate warms (Zhang et al., 2007). This would lead to increased velocities, especially in this region, where high velocities and fluxes seem to reflect naturally high balance velocities due to extremely high snow accumulation, as opposed to dynamic responses to changing climate or calving terminus criteria (Burgess et al., 2013).

Kaskawulsh Glacier

The cumulative signal of change in the pattern and magnitude of flow of the Kaskawulsh Glacier over the past 50 years is complex. In the upper glacier, at the Kaskawulsh-Hubbard Divide and in the accumulation basins of the North and Central arms, there was no change between the 1960s through 1987-88 and 1997-98. In some places it appears that there may be slight increases in velocity. Near the equilibrium line (North Arm-Central Arm confluence), velocity has decreased by 40-50% since 1964-65. At the terminus, there has been a comparable decrease in velocity since 1987-88, although change from 1997-98 to 2011/2012 seems to be small.

The significant decreases in velocity from the 1960s and 1980s to the present of parts of the Kaskawulsh Glacier and the upper Hubbard Glacier can represent a combination of a number of factors operating on varying timescales. Among these is seasonal variations in velocity. At the Kaskawulsh Glacier in 2009-10 and 2010-11, the winter season lasted for 40% of the year and the winter-annual velocity variation in 2009-10 was approximately 33.4 m a^{-1}, slightly less in 2010-11 (Darling, 2012). Given this value, the difference between the 1962-63 annual velocities and the 2011/2012 winter velocities of up to 200 m a^{-1} cannot be explained by seasonal variation.

The decrease in velocity at this point and at the cross profile nearest the terminus can be related to thinning on the lower portion of the Kaskawulsh Glacier from 1977 to 2007 (Foy et al., 2011). It has been noted elsewhere that the response of mountain glaciers to the current mass loss is one of deceleration (Heid and Kääb, 2012). It seems that the thinner ice column has a larger effect on the shear stress than the increased surface slope that arises from thinning at the terminus and slight thickening in the upper reaches.

Velocities derived from the 1997-98 date pair on the upper Hubbard and the Kaskawulsh Glaciers were in all cases lower than velocities derived at the same locations in other years. On the Hubbard Glacier, the 1997-98 mean was less by approximately 100 m a^{-1} (30%). At the terminus of the Kaskawulsh Glacier, it was less by a smaller but still significant margin. The 1997-98 measurement period comprised 352 days from June 30, 1997 to June 17, 1998. Annual dGPS measurements from 2009-2011 on the Kaskawulsh Glacier indicate that velocity peaks in spring (2010 spring velocity peak May 28; 2011 spring velocity peak May 30) with high velocities maintained for several days either side of the peak. If the onset of melt has been becoming earlier, as is a reasonable supposition in a warming climate, then in 1997-98, this velocity peak could fall within the bracket of the unmeasured days June 17-June 30. With this in mind, it was determined that a 200% increase in velocity over the 352-day average would have to be sustained over the 13-day gap period in order for the 1997-98 Kaskawulsh terminus profile (D-D’) to have a magnitude similar to the 2011-2012 profile within the measurement error. This exceeds the magnitude of the spring increases (relative to the mean annual horizontal velocity) measured in 2010 and 2011 by Darling (2012). It seems that the lower 1997-1998 velocity cannot be explained by seasonal variation, although it is still possible that seasonal variability contributes to the lower values. It is possible that the anomalous velocities in 1997-98 could have a climatic control, and it therefore illustrates another source of interannual variability separate from surge dynamics. The magnitude of the difference is large, and provides a lower bracket to the range of variability possible.

Glacier Name	GLIMS glacier system	2011		2012		Previous known surges				Quiescent velocity ($m\ a^{-1}$)	Periodicity (years)	References
		Peak centreline velocity ($m\ a^{-1}$)	*Surge status (Q/A)*	*Peak centreline velocity ($m\ a^{-1}$)*	*Surge status (Q/A)*	*Year (start)*	*Duration (years)*	*Peak velocity*	*Peak displacement*			
Previously-known surge-type glaciers, confident classification												
Walsh	Logan	279	Q	271	Q	~1912-1918	4		11.5 km		~40 years	Post, 1966; 1967 Post, 1966
						1960/61						
Klutlan	Klutlan	n/d	n/d	18	Q	1961			5 km			Driscoll, 1980
Nesham	Klutlan	n/d	n/d	91	Q	1961	2		4 km			Post, 1969; Driscoll, 1980
Mount Wood	Klutlan	83	Q	113	Q							
Steele	Steele	148	Q	211	Q	1940-41	< 1			almost stagnant		Stanley, 1969
						1965	3	24 $m\ d^{-1}$	9.5 km			
"several" Steele tributaries	Steele	10 - 70	Q	10 - 130	Q	1965						Stanley, 1969
Hodgson	Steele	31	Q*	< 8	Q	~1970						Clarke and Holdsworth, 2002
Rusty	Rusty	< 15	Q	< 8	Q					~ 4		Collins, 1972 Frappé and Clarke, 2007
Trapridge	Trapridge	< 15	Q	< 15	Q	1941	> 4			~20 (1969-70) <10 $m\ a^{-1}$ (2002-05)	40-60	Collins, 1972
						~1980	up to 20	42 $m\ a^{-1}$				Frappé and Clarke, 2007
Backe	Backe	41	Q*	< 8	Q	~1963	> 4					Collins, 1972
Kluane	Kluane	212	Q	218	Q							
Disappointment	Disappointment	104	Q	120	Q							Field, 1975
Felsite	Felsite	85	Q	69	Q							Field, 1975
Dusty	Dusty	135	Q	118	Q	1966						Clarke and Holdsworth, 2002
Lowell	Lowell	396	Q	367	Q	1948	2			125		Clarke and Holdsworth, 2002
						1968	2			(mid glacier)		Bevington and Copland, submitted 2013)
						1983	< 1	45 $m\ d^{-1}$		15		
						1997	< 1			(near terminus)		
						2009	< 1				12-20	
Fisher	Fisher	119	Q	135	Q	~1970						Clarke and Holdsworth, 2002
Tweedsmuir	Tweedsmuir	n/d	n/d	39	Q	1973	< 1	> 10 m/d^{-1}				Holdsworth, 1973; Krimmel and Meyer,
						2008					20-30	1975; Clarke and Holdsworth, 2002
Variegated	Variegated	73	Q	92	Q	1905/1906						
						~1921						
						~1931						Raymond and Harrison, 1988
						1946						Kamb et al., 1985
						1982	< 1	50 $m\ d^{-1}$				Eisen et al., 2001
						1995	< 1			winter:		Eisen et al., 2005
						2003	1			70-200	~15	Harrison et al., 2007
Haenke	Haenke	n/d	n/d	< 50	Q	1905						
						~1930				lower glacier		
						~1959				largely stagnant		Field, 1975

* small glacier, less confidence in classification

Table 5.1: 2011 and 2012 velocities and surge status of known surge-type glaciers observed to be in quiescence during the study period. A summary of the known characteristics of each is included.

Glacier Name	**GLIMS glacier system**	**2011**		**2012**		**Previous known surges**				**Quiescent velocity (m a^{-1})**	**Periodicity (years)**	**References**
		Peak centreline velocity (m a^{-1})	***Surge status (Q/A)***	***Peak centreline velocity (m a^{-1})***	***Surge status (Q/A)***	***Year (start)***	***Duration (years)***	***Peak velocity***	***Peak displace-ment***			
Mount Wood tributary	Klutlan	98	Q	321	**A**							Post, 1969; Field, 1975
Mount Wood tributary	Klutlan	129	**A**	26	Q							Post, 1969; Field, 1975
Hazard	Hazard	98	**A**	112	**A**	~1920				~31 (upper glacier 1967-1978)	15-25	Clarke and Collins, 1984
						1941			2.8 km			
						~1960-1967			0.7 km			
						1981						
Donjek	Donjek	401	**A**	397	**A**	3 surges 1930-1970						Johnson, 1972 Clarke and Holdsworth, 2002
						1978 (minor)						
last SE tributary of Donjek	Donjek	390	**A**	139	**A?**	1974	< 1					Clarke and Holdsworth, 2002

Table 5.2: 2011 and 2012 velocities and surge status of known surge-type glaciers showing evidence of an active surge phase during the study period. A summary of the known characteristics of each is included.

Glacier Name	**GLIMS glacier system**	**2011**		**2012**		**Previous known surges**				**Quiescent velocity (m a^{-1})**	**Periodicity (years)**	**References**
		Peak centreline velocity (m a^{-1})	***Surge status (Q/A)***	***Peak centreline velocity (m a^{-1})***	***Surge status (Q/A)***	***Year (start)***	***Duration (years)***	***Peak velocity***	***Peak displace-ment***			
Previously-known surge-type glaciers, not possible to confidently classify												
Anderson	Chitina	378	?	376	?	1966	5					Post, 1967; Field, 1975
Chitina	Chitina	279	?	309	?	~1968	~ 4?					Field, 1975
Spring	Spring	120	?	173	?							
Seattle'	Hubbard	308	?	502	?							Krimmel and Trabant, 1992
Valerie	Hubbard	n/d	n/d	1552	**A?**	1986		< 10 000 m a^{-1}		1000-2000		Mayo, 1988; 1989; Krimmel and Trabant, 1992
Agassiz	Malaspina	1604	?	1518	?	2002	~ 2					Muskett et al., 2008
Marvine	Malaspina	n/d	n/d	1191	?	1987					~ 10 irregular	Muskett et al., 2008
						1999	1?					
Lower Seward	Malaspina	1754	?	1684	?	early 1930s						Muskett et al., 2008
						1954	2					
						1987	1?					
						~2001	~ 2					

Table 5.3: 2011 and 2012 velocities of known surge-type glaciers for which the 2011-2012 status is uncertain. A summary of the known characteristics of each is included.

Glacier Name	**GLIMS glacier system**	**2011**		**2012**		**Previous known surges**				**Quiescent velocity (m a^{-1})**	**Periodicity (years)**
		Peak centreline velocity (m a^{-1})	***Surge status (Q/A)***	***Peak centreline velocity (m a^{-1})***	***Surge status (Q/A)***	***Year (start)***	***Duration (years)***	***Peak velocity***	***Peak displace-ment***		
Previously unknown surge-type glaciers identified by this study						*The following are from this study*					
Logan	Logan	290	**A**	380	**A**	~ 2010	at least 3	380 m a^{-1}		<50 m a^{-1} (lower glacier 1986-1999)	
Mount Queen Mary tributaries western group	Hubbard	430	**A**	98	Q	2009					
Mount Queen Mary tributaries southern group	Hubbard	n/d	n/d	632	**A**	1986	~1-2	1744 m a^{-1}			
						2000?					
						2012					
Libbey	Agassiz	238	**A**	547	**A**	~ 2011		547 m a^{-1}			

Table 5.4: 2011 and 2012 velocities and surge status of previously-unknown surge-type glaciers identified to be surging during the study period. A summary of the known characteristics of each is included.

Chapter 6: Conclusions

This project has produced regional velocity maps for the St. Elias Icefield for the years 2011 and 2012 and velocity maps for other selected glaciers at intervals in the 1980s and 1990s. The highest velocities were measured on the Pacific-facing glaciers where basins receive high rates of accumulation from Pacific air masses. All tidewater glaciers in the study area have stable termini, and so high velocities represent high balance velocities required to balance high accumulation and ablation. Velocities of landward-facing glaciers can be an order of magnitude less, although surge activity means that balance velocities are rarely attained. The results have highlighted the high degree of interannual variability present at these glaciers, especially as regards surge-type glaciers. Surge-type glaciers that were not observed to be in the active phase of the surge cycle in 2011 or 2012 generally showed slight but significant increases in velocity from 2011 to 2012, especially in the upper reaches of their lengths. This pattern is consistent with the established quiescent velocity evolution observed at Variegated Glacier, and it suggests that most surge-type glaciers undergo some kind of evolution in their velocity throughout quiescence. Several surges were observed, including in previously unknown surge-type glaciers, notably the Logan Glacier, but also two tributary branches of the upper Hubbard Glacier.

Over longer timescales, there was evidence for glacier deceleration at the Kaskawulsh Glacier. At the Hubbard Glacier, there was no consistent trend. The Upper Glacier showed high agreement between the velocities of the date periods measured, and at the terminus an observed increase in velocity does not follow the deceleration trend identified previously and may be a result of increased inputs from Valerie Glacier near the terminus and seasonal variability.

6.1 Future research

While it is difficult to determine if observed variations in the velocity of surge-type glaciers represent to any degree long-term flow evolution in response to climatic dynamics, there is still potential to be found in monitoring surge-type glaciers. Studies of glacier systems that have been observed through repeated surges have found that periodicity, duration and maximum terminus displacement can evolve over time (e.g. Bevington and Copland, submitted 2013). In a similar vein, it should be possible to track changes in the dynamics of surge-type glaciers using their quiescent velocity structure, as long as the latter can be mapped with sufficient detail and frequency.

This and other studies have revealed large interannual variations; it seems that most glaciers may experience some form of flow instability. In previous studies of the area there are numerous references to “minor” or “weak” surges, or speed “pulses” in glaciers that are otherwise considered to be non-surge type (e.g. Clarke and Collins, 1983; Ritchie, 2008). The anomalously low 1997-98 velocities suggest that glacier velocity may respond quite rapidly to external forcings. The distinction between ‘normal flow’ and ‘surge-type’ glaciers may be less clearcut than common usage tends to imply. In a region such as the St. Elias Icefield where the majority of glaciers surge, and where ice fluxes are thus extremely variable, it will not be possible to accurately identify long-term glacier evolution in velocity and in ice flux until there is a better understanding of the magnitude of interannual variability, from both surging and other sources of variability.

To this end, the extensive spatial and temporal coverage provided by satellite imagery, in particular SAR platforms, can be of great use. The region has now been almost fully mapped at two intervals, using ALOS L-band data (Burgess et al., 2013) and Radarsat-2 C-band data (this study), showing that quantification of the degree of variability in major glaciers in the region could be feasible. This information will be instrumental in refining ice flux estimates and determining how they change through time.

Chapter 7: References

Alford, D., & Keeler, C. (1970). Stratigraphic studies of the winter snow layer, Mount Logan, Saint Elias Range. In V. C. Bushnell & R. H. Ragle (Eds.), *Icefield Ranges Research Project Scientific Results: Volume 2* (pp. 37-42). Montreal: American Geographical Society.

Alford, D., (1970). Density variations in alpine snow. In V. C. Bushnell & R. H. Ragle (Eds.), *Icefield Ranges Research Project Scientific Results: Volume 2* (pp. 43-50). Montreal: American Geographical Society.

Alley, R. B. (2000). Continuity comes first: recent progress in understanding subglacial deformation. *Geological Society, London, Special Publications*, *176*(1), 171–179. doi:10.1144/GSL.SP.2000.176.01.13

AMAP, 2012. Arctic Climate Issues 2011: Changes in Arctic Snow, Water, Ice and Permafrost. SWIPA 2011 Overview Report. 97 pp.

Amundson, J. M., & Truffer, M. (2010). A unifying framework for iceberg-calving models. *Journal of Glaciology*, *56*(199), 822–830. doi:10.3189/002214310794457173.

Anderson, R. S., Anderson, S. P., MacGregor, K. R., Waddington, E. D., O'Neel, S., Riihimaki, C. A., & Loso, M. G. (2004). Strong feedbacks between hydrology and sliding of a small alpine glacier. *Journal of Geophysical Research*, *109*(F3), 1–17. doi:10.1029/2004JF000120.

Anderton, P. W. (1970). Deformation of Surface Ice at a Glacier Confluence, Kaskawulsh Glacier. In V. C. Bushnell & R. H. Ragle (Eds.), *Icefield Ranges Research Project Scientific Results: Volume 2* (pp. 59–76). Montreal: American Geophysical Union and Arctic Institute of North America.

Arendt, A. A., Echelmeyer, K. A., Harrison, W. D., Lingle, C. S., & Valentine, V. B. (2002). Rapid wastage of Alaska glaciers and their contribution to rising sea level. *Science*, *297*(5580), 382–6.

Arendt, A., Luthcke, S., Larsen, C. F., Abdalati, W., Krabill, W. B., & Beedle, M. J. (2008). Validation of high-resolution GRACE mascon estimates of glacier mass changes in the St Elias Mountains, Alaska, USA, using aircraft laser altimetry. *Journal of Glaciology*, *54*(188), 778–787.

Barrand, N. E., & Sharp, M. J. (2010). Sustained rapid shrinkage of Yukon glaciers since the 1957–1958 International Geophysical Year. *Geophysical Research Letters*, *37*(7), 1–5.

Benn, D. I., & Evans, D. J. (2010). *Glaciers and glaciation*. Hodder Education. London. 802 pp.

Benn, D. I., Hulton, N. R. J., & Mottram, R. H. (2007). “Calving laws”, “sliding laws” and the stability of tidewater glaciers. *Annals of Glaciology*, (46), 123–130.

Berthier, E., Schiefer, E., Clarke, G. K. C., Menounos, B., & Rémy, F. (2010). Contribution of Alaskan glaciers to sea-level rise derived from satellite imagery. *Nature Geoscience*, *3*(2), 92–95.

Berthier, E., Vadon, H., Baratoux, D., Arnaud, Y., Vincent, C., Feigl, K. L., Rémy, F., Legrésy, B. (2005). Surface motion of mountain glaciers derived from satellite optical imagery. *Remote Sensing of Environment*, *95*(1), 14–28.

Bevington, A., & Copland, L. (2013). The 2009-2010 surge of Lowell Glacier, Yukon, and its historical context. Submitted to *Journal of Glaciology*.

Bindschadler, R. (1983). The importance of pressurized subglacial water in separation and sliding at the glacier bed. *Journal of Glaciology*, *29*(101), 3-19.

Blake, E., Clarke, G. K., & Gérin, M. C. (1992). Tools for examining subglacial bed deformation. *Journal of Glaciology*, *38*, 388-396.

Blatter, H., & Hutter, K. (1991). Polythermal conditions in Arctic glaciers.*Journal of Glaciology*, 37(126).261-269.

Boulton, G. S. & Jones, A.S. 1979. Stability of temperate ice sheets resting on beds of deformable sediment. *Journal of Glaciology*, *24*, 29-43.

Boulton, G. S., & Hindmarsh, R. C. A. (1987). Sediment deformation beneath glaciers: Rheology and geological consequences. *Journal of Geophysical Research*, *92*(B9), 9059–9082. doi:10.1029/JB092iB09p09059.

Brecher, H. H. (1969). Surface Velocity Measurements on the Kaskawulsh Glacier. In V. C. Bushnell & R. H. Ragle (Eds.), *Icefield Ranges Research Project Scientific Results: Volume 1* (pp. 127–144). Montreal: American Geophysical Union and Arctic Institute of North America.

Brown, B. C. S., Meier, M. F., & Post, A. (1982). Calving Speed of Alaska Tidewater Glaciers, With Application to Columbia Glacier. *U.S. Geological Survey Professional Paper 1258-C*, 20 pp.

Budd, W. F., Keage, P. L., & Blundy, N. A. (1979). Empirical studies of ice sliding. *J. Glaciol*, *23*(89), 157-170.

Burgess, E. W., Forster, R. R., & Larsen, C. F. (2013). Flow velocities of Alaskan glaciers. *Nature communications*, *4*, 2146. doi:10.1038/ncomms3146.

Clague, J. J., & Rampton, V. N. (1982). Neoglacial Lake Alsek. *Canadian Journal of Earth Sciences*, *19*, 94–117.

Clarke, G. K. C. (1969). Geophysical Measurements on the Kaskawulsh and Hubbard Glaciers. In V. C. Bushnell & R. H. Ragle (Eds.), *Icefield Ranges Research Project Scientific Results: Volume 1* (pp. 89–106). Montreal: American Geographical Society.

Clarke, G. K. C. (1991). Length, width and slope influences on glacier surging. *Journal Of Glaciology*, *37*(126), 236–246.

Clarke, G. K. C., & Collins, S. G. (1984). The 1981-1982 surge of Hazard Glacier, Yukon Territory. *Canadian Journal of Earth Sciences*, *21*, 297–304.

Clarke, G. K. C., Collins, S. G., & Thompson, D. E. (1984). Flow, thermal structure, and subglacial conditions of a surge-type glacier. *Canadian Journal of Earth Sciences*, *21*, 232–240.

Clarke, G. K. C., & Goodman, R. H. (1975). Radio echo soundings and ice-temperature measurements in a surge-type glacier. *Journal of Glaciology*, *14*(70), 71–78.

Clarke, G. K., & Holdsworth, G. (2002). Glaciers of the St. Elias mountains. In R.S. Williams & J.G. Ferrigno (Eds.) *Glaciers of North America: Satellite Image Atlas of the World*. US Geological Survey professional paper, (1386J).

Classen, D. F., & Clarke, G. K. C. (1972). Thermal drilling and deep-ice temperature measurements on the Rusty Glacier. In V. C. Bushnell & R. H. Ragle (Eds.), *Icefield Ranges Research Project Scientific Results: Volume 3* (pp. 103-116). Montreal: American Geophysical Union and Arctic Institute of North America.

Collins, S. G. (1972). Survey of the Rusty Glacier area, Yukon Territory, Canada, 1967-70. *Journal of Glaciology*, *11*(62), 235–253.

Copland, L., Sharp, M. J., & Dowdeswell, J. A. (2003). The distribution and flow characteristics of surge-type glaciers in the Canadian High Arctic. *Annals Of Glaciology*, *36*, 73–81.

Copland, L., Sylvestre, T., Bishop, M. P., Shroder, J. F., Seong, Y. B., Owen, L. A., Bush, A., & Kamp, U. (2011). Expanded and recently increased glacier surging in the Karakoram. *Arctic, Antarctic, and Alpine Research*, *43*(4), 503-516.

Crossley, D. J., & Clarke, G. K. C. (1972). Gravity and shallow-ice temperature measurements on Rusty Glacier. In V. C. Bushnell & R. H. Ragle (Eds.), *Icefield Ranges Research Project Scientific Results: Volume 3* (pp. 93-102). Montreal: American Geophysical Union and Arctic Institute of North America.

Darling, S. (2012). Variations in Velocity of the Kaskawulsh Glacier, Yukon Territory, 2009-2011. Unpublished M.Sc. thesis, University of Ottawa.

Detwyler, T. R., (1974). Snowmelt along the environmental transect at Chitistone Pass, Alaska, during the summers of 1967, 1968, and 1969. In V. C. Bushnell & M. G. Marcus (Eds.), *Icefield Ranges Research Project Scientific Results: Volume 4* (pp. 207-210). Montreal: American Geophysical Union and Arctic Institute of North America.

Dewart, G. (1970). Seismic Investigation of Ice Properties and Bedrock Topography at the Confluence of the North and Central Arms of the Kaskawulsh Glacier. In V. C. Bushnell & R. H. Ragle (Eds.), *Icefield Ranges Research Project Scientific Results: Volume 2* (pp. 77–102). Montreal: American Geophysical Union and Arctic Institute of North America.

Driscoll, F. J. Jr. (1980). Formation of the neoglacial surge moraines of the Klutlan Glacier, Yukon Territory, Canada. *Quaternary Research, 14*, 19–30.

Dozier, J., (1974). Channel adjustments in supraglacial streams. In V. C. Bushnell & M. G. Marcus (Eds.), *Icefield Ranges Research Project Scientific Results: Volume 4* (pp. 189-206). Montreal: American Geophysical Union and Arctic Institute of North America.

Eisen, O., Harrison, W. D., & Raymond, C. F. (2001). The surges of Variegated Glacier, Alaska, U.S.A., and their connection to climate and mass balance. *Journal of Glaciology*, *47*(158), 351–358.

Eisen, O., Harrison, W. D., Raymond, C. F., Echelmeyer, K. A., Bender, G. A., & Gorda, J. L. D. (2005). Variegated Glacier, Alaska, USA: a century of surges. *Journal of Glaciology*, *51*(174), 399–406. doi:10.3189/172756505781829250.

Ewing, K. J. (1972). Supraglacial streams of the Kaskawulsh Glacier. In V. C. Bushnell & R. H. Ragle (Eds.), *Icefield Ranges Research Project Scientific Results: Volume 3* (pp. 93-102). Montreal: American Geophysical Union and Arctic Institute of North America.

Fahnestock, R. K. (1969). The morphology of the Slims River. In V. C. Bushnell & R. H. Ragle (Eds.), *Icefield Ranges Research Project Scientific Results: Volume 1* (pp. 161-172). Montreal: American Geographical Society.

Field, W. O., & Collins, S. G. (1975). Glaciers of the St. Elias Mountains. *Mountain glaciers of the Northern Hemisphere*, *2*, 143-297.

Fischer, U. H., & Clarke, G. K. C. (2001). Review of subglacial hydro-mechanical coupling: Trapridge Glacier, Yukon Territory, Canada. *Quaternary International*, *86*(1), 29–43.

Fisher, D. A., Wake, C., Kreutz, K., Yalcin, K., Steig, E., Mayewski, P., Anderson, L., Zheng, J., Rupper, S., Zfanowicz, C., Demuth, M., Dahl-Jensen, D., Goto-Azuma, K., Bourgeois, J. B., Koerner, R. M., Sekerka, J., Osterberg, E., Abbott, M.B., Finney, B. P.

& Burns, S. J. (2004). Stable isotope records from Mount Logan, Eclipse Ice cores and nearby Jellybean Lake. Water cycle of the North Pacific over 2000 years and over five vertical killometers: Sudden shifts and tropical concepts. *Géographie physique et Quaternaire*, *58*(2-3), 337–352.

Fleming, M., Chapin, F., Cramer, W., Hufford, G. L., & Serreze, M. C. (2000). Geographic patterns and dynamics of Alaskan climate interpolated from a sparse station record. *Global Change Biology*, *6*(Suppl. 1), 49–58.

Fleming, S. W., & Whitfield, P.H. (2010). Spatiotemporal mapping of ENSO and PDO surface meteorological signals in British Columbia, Yukond and Southeast Alaska. *Atmosphere-Ocean*, 48(2), 122-131.

Flowers, G. E., Roux, N., Pimentel, S., & Schoof, C. G. (2011). Present dynamics and future prognosis of a slowly surging glacier. *The Cryosphere*, *5*(1), 299–313. doi:10.5194/tc-5-299-2011

Ford, A. L. J., Forster, R. R., & Bruhn, R. L. (2003). Ice surface velocity patterns on Seward Glacier, Alaska/Yukon, and their implications for regional tectonics in the Saint Elias Mountains. *Annals of Glaciology*, *36*(1), 21–28.

Fountain, A. G., & Walder, J. S. (1998). Water flow through temperate glaciers. *Reviews of Geophysics*, *36*(3), 299–328.

Fowler, A. C. (2010). Weertman, Lliboutry and the development of sliding theory. *Journal of Glaciology*, *56*(200), 965–972. doi:10.3189/002214311796406112.

Fowler, a. C., Murray, T., & Ng, F. S. L. (2001). Thermally controlled glacier surging. *Journal of Glaciology*, *47*(159), 527–538. doi:10.3189/172756501781831792.

Foy, N., Copland, L., Zdanowicz, C., Demuth, M., & Hopkinson, C. (2011). Recent volume and area changes of Kaskawulsh Glacier, Yukon, Canada. *Journal of Glaciology*, *57*(203), 515–525.

Frappé, T.-P., & Clarke, G. K. C. (2007). Slow surge of Trapridge Glacier, Yukon Territory, Canada. *Journal of Geophysical Research*, *112*(F03S32), 1–17. doi:10.1029/2006JF000607, 2007

Glen, J. W. (1958). The flow law of ice: A discussion of the assumptions made in glacier theory, their experimental foundations and consequences. *IASH Publ*, *47*, 171-183.

Gray, A. L., Short, N., Matter, K. E., & Jezek, K.C. (2001). Velocities and flux of the Filchner Ice Shelf and its tributaries determined from speckle tracking interferometry. *Canadian Journal of Remote Sensing*, *27*, 193–206.

Harrison, W. D., & Post, A. S. (2003). How much do we really know about glacier surging? *Annals of Glaciology*, *36*(1), 1–6.

Harrison, W. D., Motyka, R. J., Truffer, M., Eisen, O., Moran, M. T., Raymond, C. F., Fahnestock, M. A., & Nolan, M. (2008). Another surge of Variegated Glacier, Alaska, USA, 2003/04. *Journal of Glaciology, 54 (184) 192-194*.

Harrison, W., Raymond, C., & MacKeith, P. (1986). Short period motion events on Variegated Glacier as observed by automatic photography and seismic methods. *Annals of Glaciology*, *8*, 82–89.

Headley, R., Hallet, B., Roe, G., Waddington, E. D., & Rignot, E. (2012). Spatial distribution of glacial erosion rates in the St. Elias range, Alaska, inferred from a realistic model of glacier dynamics. *Journal of Geophysical Research*, *117*(F3), F03027. doi:10.1029/2011JF002291

Heid T. and Kääb A. (2012a): Evaluation of existing image matching methods for deriving glacier surface displacements globally from optical satellite imagery. *Remote Sensing of Environment*, 118, 339-355.

Heid, T., & Kääb, A. (2012b). Repeat optical satellite images reveal widespread and long term decrease in land-terminating glacier speeds. *The Cryosphere*, *6*(2), 467–478.

Holdsworth, G., Howarth, P. J., and Ommanney, C. S. L. (2002) Quantitative measurements of Tweedsmuir and Lowell Glacier imagery. In R.S. Williams & J.G. Ferrigno (Eds.) *Glaciers of North America: Satellite Image Atlas of the World*. US Geological Survey professional paper, (1386J).

Howat, I. M., Joughin, I., Fahnestock, M., Smith, B. E., & Scambos, T. A. (2008). Synchronous retreat and acceleration of southeast Greenland outlet glaciers 2000 – 06 : ice dynamics and coupling to climate. *Journal of Glaciology, 54*(187), 646–660.

Huang, L. E. I., & Li, Z. (2011). Comparison of SAR and optical data in deriving glacier velocity with feature tracking. *International Journal of Remote Sensing, 32*(10), 2681–2698. doi:10.1080/01431161003720395

Hubbard, B., & Sharp, M. (1989). Basal ice formation and deformation: a review. *Progress in Physical Geography, 13*(4), 529-558.

Iken, A. (1981). The effect of the subglacial water pressure on the sliding velocity of a glacier in an idealized numerical model. *Journal of Glaciology 27*(97), 407-421.

Iken, A., & Truffer, M. (1997). The relationship between subglacial water pressure and velocity of Findelengletscher, Switzerland, during its advance and retreat. *Journal of Glaciology*, *43*(144), 328–338.

Iken, A., Röthlisberger, H., Flotron, A., & Haeberli, W. (1983). The uplift of Unteraargletscher at the beginning of the melt season—A consequence of water storage at the bed. *Journal of Glaciology*, *29*(101), 28-47.

Jacob, T., Wahr, J., Pfeffer, W. T., & Swenson, S. (2012). Recent contributions of glaciers and ice caps to sea level rise. *Nature*, *482*(7386), 514–8.

Jiskoot, H., & Juhlin, D. T. (2009). Surge of a small East Greenland glacier, 2001-2007, suggest Svalbard-type mechanism. *Journal of Glaciology*, *55*(191), 567–571.

Joughin, I., Smith, B. E., Howat, I. M., Floricioiu, D., Alley, R. B., Truffer, M., & Fahnestock, M. (2012). Seasonal to decadal scale variations in the surface velocity of Jakobshavn Isbrae, Greenland: Observation and model-based analysis. *Journal of Geophysical Research*, *117*(F2), F02030. doi:10.1029/2011JF002110.

Joughin, I., Abdalati, W., & Fahnestock, M. (2004). Large fluctuations in speed on Greenland's Jakobshavn Isbrae glacier. *Nature*, *432*(7017), 608-610.

Kääb, A. (2005a). Combination of SRTM3 and repeat ASTER data for deriving alpine glacier flow velocities in the Bhutan Himalaya. *Remote Sensing of Environment*, *94*(4), 463-474.

Kääb, A. (2005b): *Remote sensing of mountain glaciers and permafrost creep*. Schriftenreihe Physische Geographie. 48, 266pp.

Kääb A. and Vollmer M. (2000): Surface geometry, thickness changes and flow fields on creeping mountain permafrost: automatic extraction by digital image analysis. *Permafrost and Periglacial Processes*.11, 315-326

Kamb, B. (1970). Sliding motion of glaciers: theory and observation. *Reviews of Geophysics*, *8*(4), 673-728.

Kamb, B. (1987). Glacier surge mechanism based on linked cavity configuration of the basal water conduit system. *Journal of Geophysical Research*, *92*(B9), 9083–9100.

Kamb, B., & Echelmeyer, K. A. (1986). Stress-gradient coupling in glacier flow: 1. Longitudinal averaging of the influence of ice thickness and surface slope. *Journal of Glaciology*, *32*(111), 267–284.

Kamb, B., & Engelhardt, H. (1987). Waves of accelerated motion in a glacier approaching surge: the mini-surges of Variegated Glacier, Alaska, U.S.A. *Journal of Glaciology*, *33*(113), 27–46.

Kamb, B., Raymond, C. F., Harrison, W. D., Engelhardt, H., Echelmeyer, K. A., Brugman, M. M., & Pfeffer, T. (1985). Glacier surge mechanism: 1982-1983 surge of Variegated Glacier, Alaska. *Science*, *227*(4686), 469–79.

Kavanaugh, J. L., & Clarke, G. K. C. (2006). Discrimination of the flow law for subglacial sediment using in situ measurements and an interpretation model. *Journal of Geophysical Research*, *111*(F1), F01002. doi:10.1029/2005JF000346.

Kirkbride, M. P., & Warren, C. R. (1997). Calving processes at a grounded ice cliff. *Annals of glaciology*, *24*, 116-121.

Kotlyakov, V. M., Osipova, G. B., & Tsvetkov, D. G. (2008). Monitoring surging glaciers of the Pamirs, central Asia, from space. *Annals of Glaciology*, *48*(1), 125-134.

Krimmel, R. M., & Meier, M. F. (1975). Glacier applications of ERTS images. *Journal of Glaciology*, *15*(73), 391–402.

Krimmel, R. M., & Sikonia, W. G. (1986). Velocity and surface altitude of the lower part of Hubbard Glacier, Alaska, August 1986. *U.S.G.S. Open file report 86-549*, *1-13*(August 1978).

Krimmel, R. M., & Trabant, D. C. (1992). The terminus of Hubbard Glacier , Alaska. *Annals of Glaciology*, *16*, 151–157.

Krimmel, R. M., & Vaughn, B. H. (1987). Columbia Glacier, Alaska: Changes in velocity 1977–1986. *Journal of Geophysical Research*, *92*(B9), 8961. doi:10.1029/JB092iB09p08961.

Larsen, C. F., Motyka, R. J., Arendt, A. A., Echelmeyer, K. A., & Geissler, P. E. (2007). Glacier changes in southeast Alaska and northwest British Columbia and contribution to sea level rise. *Journal of Geophysical Research*, *112*(F1), 1–11.

Lemke, P., J. Ren, R.B. Alley, I. Allison, J. Carrasco, G. Flato, Y. Fujii, G. Kaser, P. Mote, R.H. Thomas and T. Zhang, 2007: Observations: Changes in Snow, Ice and Frozen Ground. In: Climate Change 2007: The Physical Science Basis. Contribution of Working Group I to the Fourth Assessment Report of the Intergovernmental Panel on Climate Change [Solomon, S., D. Qin, M. Manning, Z. Chen, M. Marquis, K.B. Averyt, M. Tignor and H.L. Miller (eds.)]. Cambridge University Press, Cambridge, United Kingdom and New York, NY, USA.

Lliboutry, L. (1968). General theory of subglacial cavitation and sliding of temperate glaciers. *Journal of Glaciology*, *7*, 21-58.

Luckman, A., Murray, T., & Strozzi, T. (2002). Surface flow evolution throughout a glacier surge measured by satellite radar interferometry. *Geophysical Research Letters*, *29*(23), 10–1 – 10–4.

Luthcke, S., Arendt, A., Rowlands, D. D., McCarthy, J. J., & Larsen, C. F. (2008). Recent glacier mass changes in the Gulf of Alaska region from GRACE mascon solutions. *Journal of Glaciology*, *54*(188), 767–777.

Macpherson, D. S., & Krouse, H. R. (1967). O18/O16 ratios in snow and ice of the Hubbard and Kaskawulsh glaciers. *Geophysical Monograph Series*, *11*, 180-194.

Marcus, M. G., & Ragle, R. H. (1970). Snow accumulation in the Icefield Ranges, St. Elias Mountains, Yukon. *Arctic, Antarctic, and Alpine Research, 2*(4), 277–292.

Mayo, L. R. (1988). Advance of Hubbard Glacier and closure of Russell Fiord, Alaska: Environmental effects and hazards in the Yakutat area. *USGS Circular*, *1016*, 4-16.

Mayo, L. R. (1989). Advance of Hubbard Glacier and 1986 outburst of Russell Fiord, Alaska, U.S.A. *Annals Of Glaciology*, *13*, 189–194.

Meier, M. F., & Post, A. S. (1969). What are glacier surges? *Canadian Journal of Earth Sciences*, *6*(4), 807–817.

Meier, M. F., & Post, A. (1987). Fast Tidewater Glaciers. *Journal of Geophysical Research*, *92(B9)*, 9051–9058.

Molnia, B. F. (2007). Late nineteenth to early twenty-first century behavior of Alaskan glaciers as indicators of changing regional climate. *Global and Planetary Change*, *56*(1-2), 23–56.

Moon, T., Joughin, I., Smith, B., & Howat, I. (2012). 21st-century evolution of Greenland outlet glacier velocities. *Science*, *336*(6081), 576–578. doi:10.1126/science.1219985

Motyka, R. J., O'Neel, S., Connor, C. L., & Echelmeyer, K. A. (2003). Twentieth century thinning of Mendenhall Glacier, Alaska, and its relationship to climate, lake calving, and glacier run-off. *Global and Planetary Change*, *35*(1), 93-112.

Motyka, R. J., & Truffer, M. (2007). Hubbard Glacier, Alaska: 2002 closure and outburst of Russell Fjord and postflood conditions at Gilbert Point. *Journal of Geophysical Research*, *112*(F2), F02004. doi:10.1029/2006JF000475.

Motyka, R. J., Truffer, M., Fahnestock, M., Mortensen, J., Rysgaard, S., & Howat, I. (2011). Submarine melting of the 1985 Jakobshavn Isbræ floating tongue and the triggering of the current retreat. *Journal of Geophysical Research*, *116*(F1), F01007. doi:10.1029/2009JF001632.

Murray, T. (2003). Is there a single surge mechanism? Contrasts in dynamics between glacier surges in Svalbard and other regions. *Journal of Geophysical Research*, *108*(B5), 2237. doi:10.1029/2002JB001906.

Muskett, R., Lingle, C., Sauber, J., Post, A. S., Tangborn, W. V., & Rabus, B. T. (2008). Surging, accelerating surface lowering and volume reduction of the Malaspina Glacier system, Alaska, USA, and Yukon, Canada, from 1972 to 2006. *Journal of Glaciology*, *54*(188), 788–800.

Nienow, P., Sharp, M., & Willis, I. (1998). Seasonal changes in the morphology of the subglacial drainage system, Haut Glacier d'Arolla, Switzerland. *Earth Surface Processes and Landforms*, *23*, 825–843.

Nye, J. F. (1970). Glacier sliding without cavitation in a linear viscous approximation. *Proceedings of the Royal Society of London. A. Mathematical and Physical Sciences, 315*(1522), 381-403.

Ommanney, C. S. L. (1980). The inventory of Canadian glaciers: procedures, techniques, progress and applications. In *Proceedings of the Riederalp Workshop, September 1978; Actes de l'Atelier de Reideralp, septembre 1978* (pp. 35–44).

Ommanney, C. S. L. (1995). 100 Years of Glacier Observations in Canada (1890-1990). In *100 years of glaciological research in Italy, 19-20 October 1995*. *Geogr. Fis. Dinam. Quat*, *18,* 321–330.

Paterson, W. S. B. (1994). *The physics of glaciers* (3rd ed.). New York, NY: Pergamon. 480 pp.

Pelto, M. S., & Warren, C. R. (1991). Relationship between tidewater glacier calving velocity and water depth at the calving front. *Annals of Glaciology*, *15*, 115–118.

Pfeffer, W. T. (2007). A simple mechanism for irreversible tidewater glacier retreat. *Journal of Geophysical Research*, *112*(F3), F03S25. doi:10.1029/2006JF000590.

Podrasky, D., Truffer, M., Fahnestock, M., Amundson, J. M., Cassotto, R., & Joughin, I. (2012). Outlet glacier response to forcing over hourly to interannual timescales, Jakobshavn Isbræ, Greenland. *Journal of Glaciology*, *58*(212), 1512–1526. doi:10.3189/2012JoG12J065.

Post, A. (1966). The Recent surge of Walsh Glacier, Yukon and Alaska. *Journal of Glaciology*, *6*(45), 375–381.

Post, A. (1969). Distribution of surging glaciers in Western North America. *Journal of Glaciology*, *8*(53), 229–240.

Post, A. (1967). Walsh Glacier surge, 1966 observations. *Journal of Glaciology,* 6(47), 763-765.

Post, A., (1975) Preliminary hydrology and historic terminal changes of Columbia Glacier, Alaska, U.S. Geological Survey Hydrologic Investigations Atlas HA-559.

Post, A., Meier, M. F., & Mayo, L. R. (1976). Measuring the motion of the Lowell and Tweedsmuir surging glaciers of British Columbia, Canada : U. S. Geological Survey Professional Paper 929, p. 180-184.

Post, A., O'Neel, S., Motyka, R. J., & Streveler, G. (2011). A complex relationship between calving glaciers and climate. *Eos, Transactions American Geophysical Union*, *92*(37), 305-306.

Pritchard, H. D., Arthern, R. J., Vaughan, D. G., & Edwards, L. A. (2009). Extensive dynamic thinning on the margins of the Greenland and Antarctic ice sheets. *Nature*, *461*(7266), 971–975.

Quincey, D. J., Copland, L., Mayer, C., Bishop, M., Luckman, A., & Belò, M. (2009). Ice velocity and climate variations for Baltoro Glacier, Pakistan. *Journal Of Glaciology*, *55*(194), 1061–1071. doi:10.3189/002214309790794913.

Rabus, B. T., & Fatland, D. R. (2000). Comparison of SAR-interferometric and surveyed velocities on a mountain glacier: Black Rapids Glacier, Alaska, USA. *Journal of Glaciology*, *46*(152), 119–128.

Raymond, C. F., & Harrison, W. D. (1988). Evolution of Variegated Glacier, Alaska, U.S.A., prior to its surge. *Journal of Glaciology*, *34*(117), 154–169.

Rignot, E., & Kanagaratnam, P. (2006). Changes in the velocity structure of the Greenland Ice Sheet. *Science*, *311*(5763), 986–90.

Rignot, E., Koppes, M., & Velicogna, I. (2010). Rapid submarine melting of the calving faces of West Greenland glaciers. *Nature Geoscience*, *3*(3), 187-191.

Ritchie, J. B., Lingle, C. S., Motyka, R. J., & Truffer, M. (2008). Seasonal fluctuations in the advance of a tidewater glacier and potential causes: Hubbard Glacier, Alaska, USA. *Journal of Glaciology*, *54*(186), 401–411. doi:10.3189/002214308785836977

Röthlisberger, H. (1972). Water pressure in intra- and subglacial channels. *Journal of Glaciology*, 11(62), 177-203.

Rupper, S., Steig, E. J., & Roe, G. (2004). The relationship between snow accumulation at Mt. Logan, Yukon, Canada, and climate variability in the North Pacific. *Journal of Climate*, 17, 4724-4739.

Scherler, D., Leprince, S., & Strecker, M. (2008). Glacier-surface velocities in alpine terrain from optical satellite imagery—Accuracy improvement and quality assessment. *Remote Sensing of Environment*, *112*(10), 3806–3819. doi:10.1016/j.rse.2008.05.018

Schoof, C. (2005). The effect of cavitation on glacier sliding. *Proceedings of the Royal Society A: Mathematical, Physical and Engineering Sciences*, *461*(2055), 609–627. doi:10.1098/rspa.2004.1350.

Schoof, C. (2010). Ice-sheet acceleration driven by melt supply variability. *Nature*, *468*(7325), 803–6. doi:10.1038/nature09618.

Short, N. H., & Gray, A. L. (2004). Potential for RADARSAT-2 interferometry : glacier monitoring using speckle tracking. *Canadian Journal of Remote Sensing*, *30*(3), 504–509.

Short, N. H., & Gray, A. L. (2005). Glacier dynamics in the Canadian High Arctic from RADARSAT-1 speckle tracking. *Canadian Journal of Remote Sensing*, *31*(3), 225–239.

Siegert, M. J. (2008). Numerical modelling of the Antarctic Ice Sheet. In (Eds. Florindo, F. and Siegert, M.J.) *Antarctic Climate Evolution*. Elsevier. 235-256 (2008).

Sikonia, W. G., Finite element glacier dynamics model applied to Columbia Glacier, Alaska, U.S. Geol. Surv. Prof. Pap., 1258-B, 1982.

Stanley, A. D. (1969). Observations of the surge of Steele Glacier, Yukon Territory, Canada. *Canadian Journal of Earth Sciences*, *6*, 819–830.

Storey, J. C., & Choate, M. J. (2004). Landsat-5 bumper-mode geometric correction. *Geoscience and Remote Sensing, IEEE Transactions on*, *42*(12), 2695-2703.

Strozzi, T., Kouraev, A., Wiesmann, A., Wegmüller, U., Sharov, A., & Werner, C. (2008). Estimation of Arctic glacier motion with satellite L-band SAR data. *Remote Sensing of Environment*, *112*(3), 636–645.

Strozzi, T., Luckman, A., Murray, T., Wegmüller, U., & Werner, C. L. (2002). Glacier Motion Estimation Using SAR Offset-Tracking Procedures. *IEEE Transaction Geosciences and Remote Sensing*, *40*(11), 2384–2391.

Sundal, A. V., Shepherd, A., Nienow, P., Hanna, E., Palmer, S., & Huybrechts, P. (2011). Melt-induced speed-up of Greenland ice sheet offset by efficient subglacial drainage. *Nature*, *469*(7331), 521–4. doi:10.1038/nature09740.

Tarr, R. S., & Martin, L. (1914). *Alaskan Glacier Studies of the National Geographic Society in the Yakutat Bay, Prince William Sound and Lower Copper River Regions*. National Geographic Society., Washington, D.C. 498 pp.

Tedesco, M., Willis, I. C., Hoffman, M. J., Banwell, A. F., Alexander, P., & Arnold, N. S. (2013). Ice dynamic response to two modes of surface lake drainage on the Greenland ice sheet. *Environmental Research Letters*, *8*(3), 034007. doi:10.1088/1748-9326/8/3/034007.

Thomson, S. (1972) Movement observations on the terminus area of the Steele Glacier. In V. C. Bushnell & R. H. Ragle (Eds.), *Icefield Ranges Research Project Scientific Results: Volume 3* (pp. 29-38). Montreal: American Geophysical Union and Arctic Institute of North America.

Trabant, D. C., Krimmel, R. M., & Post, A..1991. A preliminary forecast of the advance of Hubbard Glacier and its influence on Russell Fiord, Alaska.*U.S. Geological Survey Water Resources Investigations Report 90-4172.*

Trabant, D., Krimmel, R. M., Echelmeyer, K. A., Zirnheld, S. L., & Elsberg, D. H. (2003). The slow advance of a calving glacier: Hubbard Glacier, Alaska, USA. *Annals of Glaciology*, *36*, 45–50.

Truffer, M., Harrison, W. D., & Echelmeyer, K. A. (2000). Glacier motion dominated by processes deep in underlying till. *Journal of Glaciology*, *46*(153), 213-221.

Van de Wal, R. S. W., Boot, W., van den Broeke, M. R., Smeets, C. J. P. P., Reijmer, C. H., Donker, J. J. A, & Oerlemans, J. (2008). Large and rapid melt-induced velocity changes in the ablation zone of the Greenland Ice Sheet. *Science*, *321*(5885), 111–3.

Van der Veen, C. J. (2002). Calving glaciers. *Progress in Physical Geography*, *26*(1), 96-122.

Van Wychen, Wesley (2010). *Spatial and Temporal Variations in Ice Motion, Belcher Glacier, Devon Island, Nunavut, Canada.* Unpublished M.Sc. thesis. University of Ottawa, 167 pp.

Van Wychen, W., Copland, L., Gray, L., Burgess, D., Danielson, B., & Sharp, M. (2012). Spatial and temporal variation of ice motion and ice flux from Devon Ice Cap, Nunavut, Canada. *Journal of Glaciology*, *58*(210), 657–664. doi:10.3189/2012JoG11J164

Wagner, W. P. (1969) Snow facies and stratigraphy on the Kaskawulsh Glacier. In V. C. Bushnell & R. H. Ragle (Eds.), *Icefield Ranges Research Project Scientific Results: Volume 1* (pp. 89–106). Montreal: American Geographical Society.

Weertman, J. (1957). Steady-State Creep of Crystals. *Journal of Applied Physics*, *28*(10), 1185-1189.

Willis, I. C. (1995). Intra-annual variations in glacier motion: a review. *Progress in Physical Geography*, *19*(1), 61–106. doi:10.1177/030913339501900104

Wood, W. (1948). Project "Snow Cornice": The establishment of the Seward Glacial research station. *Arctic*, *1*(2), 107–112.

Wood, W. A. (1963). The Icefield Ranges Research Project. *The Geographical Review*, *53*(2), 163–184.

Zhang, J., Bhatt, U. S., Tangborn, W. V., & Lingle, C. S. (2007). Response of glaciers in northwestern North America to future climate change: An atmosphere/glacier hierarchical modeling approach. *Annals of Glaciology*,*46*(1), 283-290.

Zwally, H. J., Abdalati, W., Herring, T., Larson, K., Saba, J., & Steffen, K. (2002). Surface melt-induced acceleration of Greenland ice-sheet flow. *Science*, *297*(5579), 218–22.